University of California
Santa Barbara

Driving Fast and Slow: Dynamics of Periodically Modulated Quantum Gases

A dissertation submitted in partial satisfaction
of the requirements for the degree

Doctor of Philosophy
in
Physics

by

Roshan Sajjad

Committee in charge:

Professor David Weld, Chair
Professor Andrew Jayich
Professor Matthew Fisher

March 2024

The Dissertation of Roshan Sajjad is approved.

Professor Andrew Jayich

Professor Matthew Fisher

Professor David Weld, Committee Chair

January 2024

Driving Fast and Slow: Dynamics of Periodically Modulated Quantum Gases

by

Roshan Sajjad

To Nana, Nani, and Dadi

Acknowledgements

First, I must thank my family. To my parents, Ammu and Abbu, thank you for the endless love and encouragement during the entirety of my schooling, and for providing constant inspiration throughout. Not only have you always wanted the best for me, but you have also made me strive to be better, as a professional and also as a human being. To my sister Mehran, thank you for showing me what it means to explore, to be free, and to be passionate. Having you come to Santa Barbara for undergrad was just as much support for me as hopefully I was for you. To Nana, Nani, and Dadi, I wish you were still here to see what I've accomplished. You're still in my memories and prayers each and every day.

To Mina, my other half, I unfortunately don't have enough words to say how grateful I am. Not only were you a constant support during my hardest times, but you've shaped how I live my life on a day-to-day basis. From the "details", in teaching me how to properly code and cook, to the "bigger picture", in terms of how to treat people, stay balanced, and enjoy life. You're the most caring and compassionate person I've ever met, and there's no one else I'd rather watch eat an entire pound of cherries. Thanks for sharing my thoughts with me :)

To Quinn, my lab partner in crime: "Wait Spongebob, we're not cavemen, we have technology!" It's been a crazy ride these last 5+ years, but we've finally done it! From late nights taking heat engine data to watching endless episodes of Spongebob to listening to EDM for hours, our shared experiences will be how I remember much of my time in the lab. I thank you for the endless rides, the hot sauce, and for being a caring friend.

To my previous labmates, Alec and Hector, I'm grateful our friendships continued even after you were gone. Alec, you showed me that anything is possible with the right amount of talent and willpower. Between leading multiple science efforts, exploring the

food of Milwaukee during DAMOP, and teaching me everything there was to learn about noodles, I appreciated every moment of the 3 years I got to spend with you. I'm glad I got to see you grow into the science monster that you are today, and I can't wait to follow your progress throughout your career. Hector, you brought a spark of enthusiasm that was much needed after the initial months of COVID. Your willingness to learn, to try, and to keep trying got us through numerous experiments, while your creativity and fresh ideas kept every lab day intriguing and exciting. Special thanks for teaching me more about football and coffee, and I'll always miss our Saturday morning matches.

To the earlier generation of Cora, Shankari, and Kevin, thank you for being my role models first year. Most of my AMO fundamentals I learned due to your mentorship, and the work you've done since has been inspiring. To Cora I'm especially grateful for instilling within me an urgency and desire to always get work done, which was a constant motivation during my initial years.

To my current lithium labmates Jeremy, Eber, and Xiao, I wish you the absolute best of luck in the future! I know our machine is capable of excellence, especially with the upgrades you've been working hard for. I hope you can wrangle some great experiments out of it and achieve some of our ambitious goals in the coming years.

To the strontium team, keep up the great science! Toshi, you've secretly been a postdoc on lithium for many years now, and I'm indebted to you for your optics knowledge and your ability to throw great birthday parties. Peter, your in-depth understanding of relevant physics and electronics concepts is unrivaled, though what I might appreciate most is your interest in obscure movies. Anna, though you've only been here for the end of my graduate school days, it's been amazing to see you grow into an integral member of the strontium team. I will always want to talk about philosophical science fiction with you, and it's been amazing to find someone else who truly loves Chicago as much as (maybe even more than?) I do. Yifei, you've shown why our group needs a theorist, and

have carved a specialty for yourself that no one in the group currently has. I thank you for the many theoretical insights you've given me on projects that you weren't even a part of. I apologize for repeatedly scaring you.

To the potassium team, Jared, Jeremy, and Madeleine, it's been exciting to watch you build a new machine! I know there have been numerous pitfalls, but you have shown that with resilience, atomic physics can prevail. I wish I was staying long enough to watch you tweeze some BECs, but I'll be sure to follow the machine's progress even after I'm gone.

I also have to thank Xuanwei, Samyuktha, and the rest of the undergraduate students that have participated in our lab efforts. It's been my pleasure to watch you master high power electronics and have friendly chats in the office. Your track records speak for themselves and I have no doubt that you'll go on to do great things in the future.

To Kimberlee Keithley, Victor Galitski, Tommaso Macri, Patrizia Vignolo, Flavio Noronha, Thomas Busch, and Subhadeep Gupta, I am grateful for all of the knowledge and expertise you shared during our collaborations. You were pivotal in turning ideas into successful experiments and publications, and were all a genuine pleasure to talk to.

To Julie Standish, Kelsey Leonard Moore, and the rest of the Quantum Foundry, I thank you for opening my eyes to a variety of quantum-related fields while also making sure I was supported in my own. Not only was I able to talk to graduate students of other fields that I wouldn't have otherwise, but also to faculty and company partners who taught me a lot about the state of the quantum industry today.

To Dan Stack, Mike Deal, Tom Gibbons, Chris Gloo, and the rest of the Physics and CNSI staff that assisted in purchasing and maintaining our lab facilities, I thank you for always trying to meet our urgent deadlines and helping us get through some rather extreme and unorthodox scenarios, including catastrophic leaks, unexpected outages, and international politics.

To Minghan and Aaron (and Mina of course), thank you for residing with me in what currently feels like my true home. We've created many memories, including tearing out the entire kitchen floor, playing numerous games of landlord, hosting board game nights and soccer watch parties, making sushi, and adventuring to Oceanside. Collectively these experiences make the High Grove Haus a treasure, and the anticipation of coming back to it still gives me euphoria every time I touch down at SBA. Of course, none of this would have occurred if it wasn't for the generous love and affection of the Watson family, for whom words of gratitude do no justice. For allowing us into your home(s), taking care of our every request, showing us the beauty of gardening and exotic fruits, and becoming my family on the west coast, I thank you profusely.

To my friends, I thank you for reminding me how to enjoy life outside of lab. Adam and Daniel, you make me laugh more than any duo on the planet, and it feels like we haven't missed a beat even after a decade of being apart. Sid, Anand, Josh+Sarika, Adithya, Ethan, Jordan, and Cyrus, I still tell tales of our block to anyone who will listen, and I know that we'll all probably live on the same farm someday. Adib and Ahnaf, I've known you my whole life and yet that still doesn't feel long enough. Thank you for being my other Bangladeshi family, and shoutout to Ummey for being an absolute gem. Here's to many more adventures.

To Andrew Jayich and Matthew Fisher, thank you for the mentorship and guidance you've provided throughout the years. Our (almost) annual conversations always allowed me to see both theory and experiment in a bigger picture. To Andrew, I'll miss the Muppets jokes, and I hope you still think of Statler and Waldorf long after we're gone.

The last person I need to thank is my advisor, David Weld. Everyone has moments they look back on that they acknowledge significantly altered the course of their lives, and I'm certain one of those was the fateful lunch conversation I had with you at the 2018 physics visit day. You were the only professor I talked to who seemed genuinely

interested in the eclectic group of skills I had, along with an immense enthusiasm for your lab's work and a childlike curiosity about physics as a whole which has persisted to this day. When addressing my concerns about my own lack of ability and research experience, you said "Don't worry about it, the only real skill you need is plumbing." I interpreted that statement philosophically, and only found out later that it was literal. It gave me the courage to join the lab and dive in, and from there I've never looked back. I thank you for your never-ending compassion, understanding, and encouragement, and I know you're one of the main reasons I look back on my graduate school experience fondly. I can't wait to see what ideas you come up with in the future, and I'll miss the high-brow culture references and jokes you make that usually take me hours to figure out (who is that Proust guy anyway?)

Finally, these acknowledgements wouldn't be complete if I didn't mention the following entities. To the Thermofisher Neslab System III and IV Heat Exchangers, the Azurlight 130W Fiber Amplifier, the Toptica DL Pro, the Broida Hall chilled water supply, the Weld lab weekly meetings, the biweekly DL cleanups, and the "scheduled" power outages: see ya!

Curriculum Vitæ

Roshan Sajjad

Education

2024	Ph.D. in Physics, University of California, Santa Barbara.
2021	M.A. in Physics, University of California, Santa Barbara.
2018	B.S. in Mechanical Engineering and B.S. in Physics, Carnegie Mellon University

Publications

Thermodynamic engine with a quantum degenerate working fluid. E.Q. Simmons, **R. Sajjad**, K. Keithley, H. Mas, J.L. Tanlimco, E. Nolasco-Martinez, Y. Bai, G.H. Fredrickson, and D.M. Weld. *Phys. Rev. Research* **5**, L042009 (2023)

Interaction-driven breakdown of dynamical localization in a kicked quantum gas. A. Cao, **R. Sajjad**, H. Mas, E.Q. Simmons, J.L. Tanlimco, E. Nolasco-Martinez, T. Shimasaki, H.E. Kondakci, V. Galitski, and D.M. Weld. *Nature Physics* **18**, 1302–1306 (2022).

Observation of the quantum boomerang effect. **R. Sajjad**, J.L. Tanlimco, H. Mas, A. Cao, E. Nolasco-Martinez, E.Q. Simmons, F.L.N. Santos, P. Vignolo, T. Macrì, and D.M. Weld. *Phys. Rev. X* **12**, 011035 (2022).

Transport controlled by Poincaré orbit topology in a driven inhomogeneous lattice gas. A. Cao, **R. Sajjad**, E.Q. Simmons, C.J. Fujiwara, T. Shimasaki, and D.M. Weld. *Phys. Rev. Research* **2**, 032032(R) (2020).

Probing Nonexponential Decay in Floquet–Bloch Bands. A. Cao, C.J. Fujiwara, **R. Sajjad**, E.Q. Simmons, E. Lindroth, and D.M. Weld. *Zeitschrift für Naturforschung A* **75**, 5, 443-448 (2020).

Abstract

Driving Fast and Slow: Dynamics of Periodically Modulated Quantum Gases

by

Roshan Sajjad

Driven degenerate quantum gases are flexible platforms that allow for rich investigations of quantum dynamics. Certain gases, such as Bose-Einstein condensates of ^{7}Li, also afford the ability to tune interactions and thus study quantum many-body phenomena. In this thesis, I present three experiments which explore dynamic and thermodynamic quantum behavior using both periodic driving and interaction control. The experiments span a range of frequencies from Hz to MHz, and elucidate fundamental phenomena of localization and energy transfer. I will first describe an experiment which introduces interactions to the quantum kicked rotor, a prototypical quantum chaotic system, and observe the role interactions play in localization. I will then show how using the same system with altered symmetries can create a probe for previously unobserved dynamical signatures of Anderson localization. Finally, switching to a completely different regime, I'll outline how a slowly driven quantum gas can be used to realize a novel quantum thermodynamic engine.

Contents

Chapter 1

Techniques of Quantum Control

1.1 Foreword

The story I'm about to tell you should invoke the same feeling you got when you were a child entering your first playground. The structures before you were intimidating, the possibilities were endless, and you were excited to see and experience it all. This feeling has held firm throughout my graduate school career, and hopefully I can convey some of that emotion in this work. Indeed, building and maintaining an atomic physics machine is very akin to creating a playground, while performing experiments evokes the joy of using one.

The experiments I'll be discussing in this thesis involve two topics: *localization* and *thermodynamics*. These topics are fundamental in condensed matter and statistical mechanics, and our ultracold atom machines are well-suited to explore outstanding physics questions pertinent to them. This work will also demonstrate the power cold atom machines have for investigating problems in wildly different regimes. The first two experiments I discuss will analyze the behavior of atoms driven by MHz-sacle frequencies, while the last will involve driving atoms at just a few Hz.

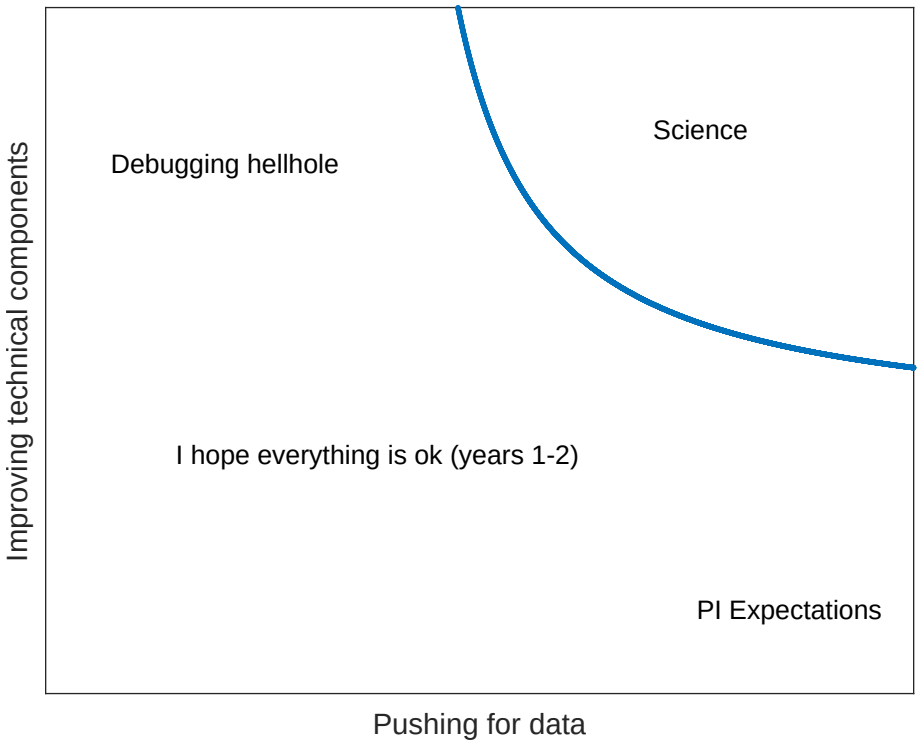

Fig. 1.1: The daily choice given to every experimental graduate student

A brief warning for future students: These machines are beasts that are impossible to fully tame, and will never be perfect. As an experimentalist, when using them you should always solve problems faster than they appear. I like to imagine that the ability to use them for science has a not-so-well defined 2D phase transition, with the two dimensions being "improving technical components" and "pushing for data" (Fig. 1.1). The former involves working to increase reliability, performing machine upgrades, and/or buying new equipment to improve the output of the experimental apparatus. The latter involves relentlessly taking data, analyzing it, and feeding back to take more data until hypotheses have been proven or disproven. The balance between the two is essentially a competition between whether your machine is good enough and whether YOU are good enough, and is a choice each graduate student faces every single day. It's always difficult to determine the right answer, but those who make the correct decision more often than

not will probably find themselves happier with their graduate school experience.

The layout of this thesis is as follows: The first chapter will detail the main techniques of quantum control relevant to our experimental setup. Chapter 2 will describe the experimental apparatus and the multi-step procedure required to create our ultracold atoms. These first two chapters are rather high level, as many of the apparatus details can found in earlier group theses [1–3]. There is a jump in technical complexity for the latter 3 chapters of the thesis, which describe experiments that I specifically worked on. Chapter 3 discusses the interacting quantum kicked rotor experiment, which is a prerequisite to Chapter 4, detailing the observation of the quantum boomerang effect. Chapter 5 will end the thesis by describing our novel quantum thermodynamic engine. But before we get there, let's start with the basics.

1.2 Lithium

The experiments discussed in this thesis were all performed with ^{7}Li, which will act as the starting point of our discussion on quantum control. ^{7}Li has many properties that are advantageous for performing quantum science, including:

- a single valence electron which yields an accessible level structure
- two hyperfine ground states with a convenient microwave transition of 803 MHz.
- a low mass of 7 amu, allowing for fast dynamics and tunneling
- tunable interactions via a broad Feshbach resonance

I'll explain each of these points in finer detail in this section.

^{7}Li is a bosonic element with 3 protons and 4 neutrons, and has 93% isotopic abundance. It is an alkali metal, meaning it has one valence electron, and this dictates much

of its quantum mechanical level structure. An atom's level structure can be expressed with Russel-Saunders notation, written in the form $^{2S+1}L_J$. Here S is the electron spin quantum number, L is the orbital quantum number, and J is the total angular momentum quantum number. For ^{7}Li, $S = 1/2$ due to the lone valence electron, and the ground state is the $^2S_{1/2}$ state. Fig. 1.2 shows the full level diagram for the first few energy levels of ^{7}Li, including the hyperfine splitting caused by the interaction of the nuclear magnetic dipole moment with the magnetic field created by the electron. For the remainder of this thesis, the transition from the ground state to the $2P_{1/2}$ state will be referred to as the D1 transition, and the transition from the ground state to the $2P_{3/2}$ state as the D2 transition.

There are a few things to note. First, the transitions from the ground to the first excited states occur around 671 nm, meaning most of the lasers used to experimentally address these states are red, typically giving the lab a sinister glow. Second, the two ground state levels are split by 803.5 MHZ, which is a convenient frequency to address via radiofrequency (RF) synthesis. RF by definition falls into the range of 3 kHz to 300 GHz, and the 803.5 MHz frequency happens to fall into one of the major frequency bands for cell phones, making commercial electronics for this frequency readily available. Third, the energy differences between the 4 magnetic sublevels in the upper excited state $^2P_{3/2}$ are all <10 MHz. This is a rather small difference compared to the natural linewidth of the transition ($\Gamma = 2\pi * 5.9$ MHz), and causes some ambiguity for which state the atom goes into when excited to this manifold (the hyperfine levels are *unresolved*). This subsequently causes ambiguity for which state the atom will decay into, which creates the need for additional lasers to address the full spectrum of states.

For exploring novel physics, ^{7}Li's light mass of 7 amu allows for fast dynamics and tunneling. The relevant energy scale of most experiments discussed in this thesis is the recoil energy $E_R = \hbar^2 k_L^2/2m$ where k_L is the wavenumber of laser light and m is the

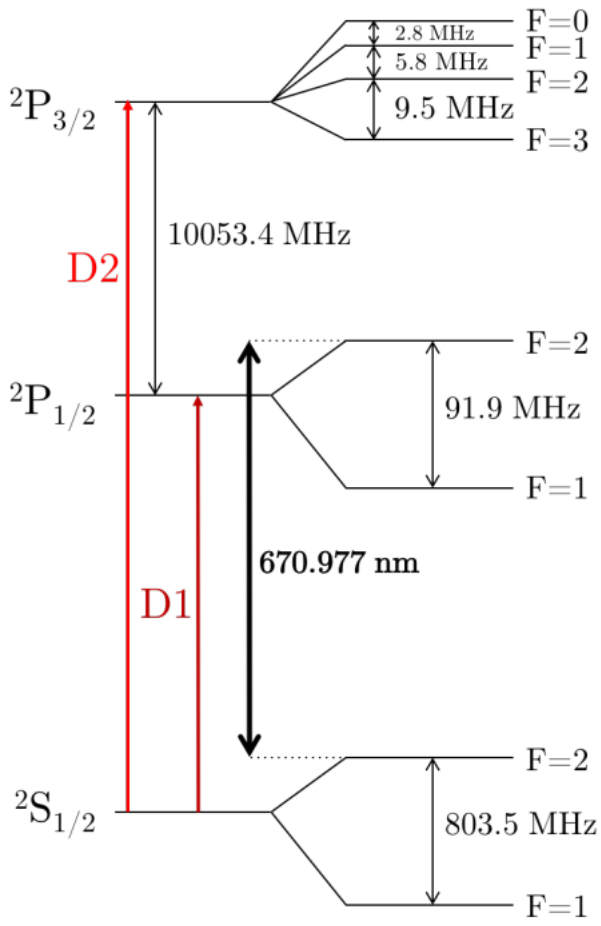

Fig. 1.2: ^{7}Li level structure, taken from [2]

mass of ^{7}Li, 7 amu. The light mass in the denominator makes the energy scale larger than those of other typical atoms used in AMO experiments (ie. Rb has a mass 12 times larger than ^{7}Li), and accordingly the relevant time scales for experiments are much shorter, typically on the order of a few ms or less.

Finally, lithium has a broad Feshbach resonance, allowing for interactions to be tuned via an applied DC magnetic field. This is further outlined in 1.5, but for now I'll say this has many experimental benefits. The ease of interaction control makes ^{7}Li an ideal tool for studying *many-body* quantum systems, where a collective of quantum particles can interact amongst themselves. Studying these types of systems is currently one of the

largest theoretical and experimental challenges in quantum science, and has applications for quantum simulation, sensing, and computing.

1.3 Laser Cooling

To get from a discussion of atoms to a discussion of experiments, we will need to trap the atoms and make them behave quantum mechanically. To achieve this, we're going to cool them down to near 0K, initially using a technique called *laser cooling*. Laser cooling is a counterintuitive method of reducing the temperature of atoms with laser light. While the nonscientist may have only seen lasers heat objects and/or blow them up in modern media, on smaller scales they interact with matter in a very different way. Consider a laser beam moving towards a counter-propagating beam of atoms. The atoms are dilute and identical, so each atom can be considered individually, and the laser can be treated as a collimated stream of monochromatic photons. If the photon frequency is close to a resonant transition in the atoms, then an atom can absorb a photon from the laser and re-emit it in a random direction. This process can happen many times, and each interaction must conserve both energy and momentum. Since the emitted photons from the interaction scatter isotropically, each absorbed photon will impart some momentum opposite to the direction of the atoms motion. Collectively, this interaction gives rise to the *scattering force* [4]. The scattering force can be calculated by multiplying the photon momentum by the scattering rate:

$$F_{scatt} = \hbar k \frac{\Gamma}{2} \frac{s}{1 + s + 4\delta^2/\Gamma^2}. \tag{1.1}$$

Here $\hbar k$ is the photon momentum, Γ the linewidth of the transition, $s = I/I_{sat}$ the saturation parameter (the intensity divided by the saturation intensity), and $\delta =$

$\omega - \omega_0 + kv$ the detuning, taking into account the doppler shift. In the limit of infinite laser power, $I \to \infty$, the maximum amount of force that can be applied if spontaneous emission is involved is $F_{max} = \frac{1}{2}\hbar k\Gamma$. Using the kinematic equation for constant acceleration

$$v_0^2 - v^2 = 2aL, \tag{1.2}$$

with a the acceleration, we can estimate the length L of atom-light interaction required to "stop" the atoms. For our experiment the ^{7}Li atoms start at a temperature of 550 K, corresponding to an initial velocity $v_0 \approx 1$km/s. Typical a values fall around

$$a \approx \frac{1}{2}\frac{F_{max}}{m} = \frac{\hbar k\Gamma}{4m} \tag{1.3}$$

with m the mass of ^{7}Li. The full stopping distance is then

$$L_{stop} = \frac{v_0^2}{2a} \approx \frac{2mv_0^2}{\hbar k\Gamma} \tag{1.4}$$

For ^{7}Li, $k = 2\pi/671$nm and $\Gamma = 2\pi * 5.9$ MHz, yielding $L_{stop} \approx 1$m. As we'll see in Chapter 2, this sets the length scale required to initiate the cooling process to quantum degeneracy.

It is difficult to understate how important laser cooling is to the field of AMO physics. Throughout this thesis we'll see how it helps achieve sub Kelvin temperatures for ^{7}Li, but it's worth noting that this technique is ubiquitously used regardless of element and particle. Indeed, atom, ion, and molecule trappers owe their existence to the discovery of laser cooling, and it is no surprise that this technique warranted the highest accolades. In 1997, Claude Cohen-Tannoudhi, Steven Chu, and William Phillips won the Nobel Prize in Physics "for development of methods to cool and trap atoms with laser light" [5].

1.4 Bose-Einstein Condensation

As atoms are cooled, it's useful to describe what happens to their *de Broglie wavelength*:

$$\lambda_{dB} = \frac{h}{p} = \frac{h}{\sqrt{2mk_BT}} \tag{1.5}$$

This quantity is an intuitively easy way to understand the wave-like nature of particles, and represents the spatial extent in which the particle can reside. For a ^{7}Li atom at room temperature, $\lambda_{dB} \approx .7\mathring{A}$, on the length scale most people are familiar with when learning about atoms in high school chemistry. However, as the temperature is lowered to 10 nK, typical of the temperatures achieved in the lab, $\lambda_{dB} \approx 12\mu$m, much larger than the interparticle spacing in the atomic cloud. In this regime, the wavefunctions of the atoms overlap and constructively interfere to give rise to a collective matter wave, the Bose-Einstein condensate (BEC). This is pictorially shown in Fig. 1.3.

While Fig. 1.3 shows a nice intuitive visualization of Bose condensation, the quantum mechanical behavior of the atoms can be understood in more detail from a statistical mechanics treatment. We start by recalling the expected occupation number for a single particle state i for bosons:

$$\langle N_i \rangle = \frac{1}{e^{(E_i-\mu)/k_BT} - 1} \tag{1.6}$$

where E_i is the energy of the single particle state i and μ is the chemical potential. At high temperatures this effectively recovers the Boltzmann distribution, $\langle N_i \rangle \approx e^{-(E_i-\mu)/k_BT}$. Now let's consider the ground state occupation, $N_0 = [e^{(E_0-\mu)/k_BT} - 1]^{-1}$. Here the difference between the ground state energy E_0 and μ is small compared to k_BT, and allows for the expansion

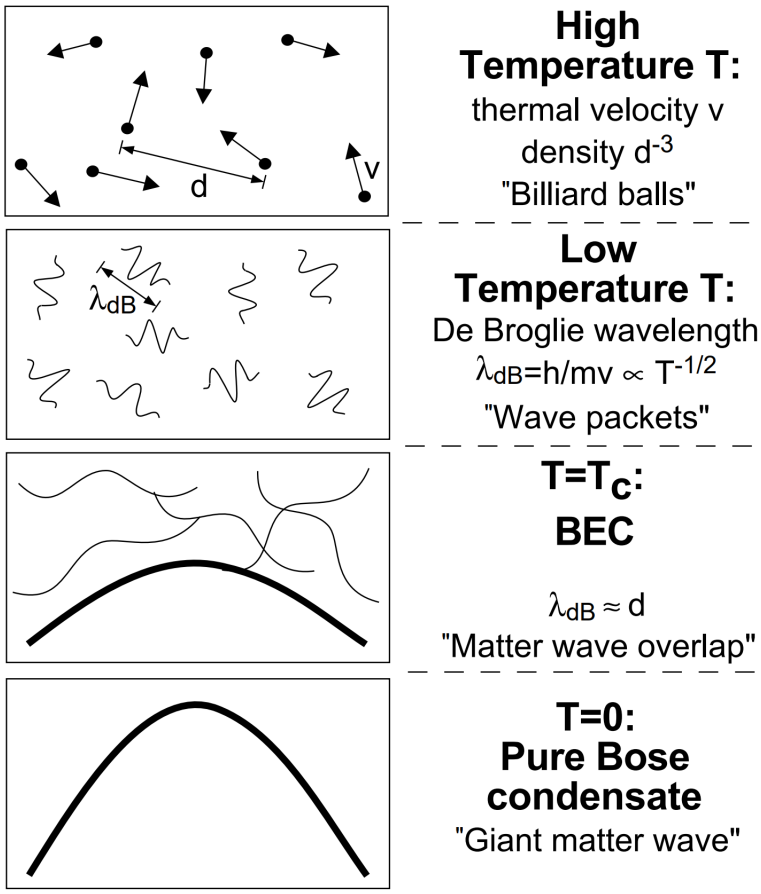

Fig. 1.3: Transition of particles from the "billiard ball" picture to Bose-Einstein condensation, taken from [6]. As they are cooled, particle de Broglie wavelengths get larger and larger until there is a collective overlap, whose resulting interference creates a matter wave.

$$E_i - \mu \approx \frac{k_B T}{N_0}. \tag{1.7}$$

As $T \to 0$, we see the energy difference and thus the exponent in 1.6 go to 0, which causes N_0 to become large. This *macroscopic occupation of the ground state* is the key feature of BECs, as all particles in the condensed phase share the same wavefunction. The temperature where this transition occurs for a harmonically trapped 3D Bose gas is

$$T_c \approx 3.31 \frac{\hbar^2 n^{2/3}}{m k_B}, \tag{1.8}$$

with n the density, derived in [7]. The density of the ^{7}Li atomic cloud is roughly 10^{12} atoms/cm^3, giving $T_c \approx 250$ nK. The *condensate fraction* n_0, or the proportion of atoms in the condensed phase, is given by

$$n_0 = \frac{N_0}{N} = 1 - \left(\frac{T}{T_c}\right)^{3/2}. \tag{1.9}$$

Thus as the temperature is decreased, more atoms enter the condensed phase from the thermal fraction ($n_{th} = 1 - n_0$). The above describes condensation of a non-interacting Bose gas, but in practice BECs have a finite interaction strength. The treatment of interactions can be quite complex, as exact solutions become quickly intractable as the particle number is increased. However, approximations can be made to glean overall behavior while reducing computational complexity. One of the most commonly used approximations is known as the Gross-Pitaevskii equation, which treats the interactions as a mean field term in the time-dependent Schrodinger equation:

$$(-\frac{\hbar^2\nabla^2}{2m} + V(\mathbf{r}) + g|\psi(\mathbf{r},t)|^2)\psi(\mathbf{r},t) = E\psi(\mathbf{r},t). \tag{1.10}$$

Here the coupling constant $g = 4\pi\hbar^2 a_s/m$ represents the mean field interaction, and is proportional to the s-wave scattering length. The potential $V(\mathbf{r})$ for our experiments is typically a 3D harmonic potential. In the strongly interacting limit, known as the Thomas-Fermi approximation, the kinetic energy term in 1.10 can be neglected, yielding a ground state density

$$n(\mathbf{r}) = \max(\frac{\mu - V(\mathbf{r})}{g}, 0). \tag{1.11}$$

This distribution is parabolic while the right hand side of 1.11 is positive and 0 otherwise. An example atomic image of this distribution is shown in Fig. 1.4. The

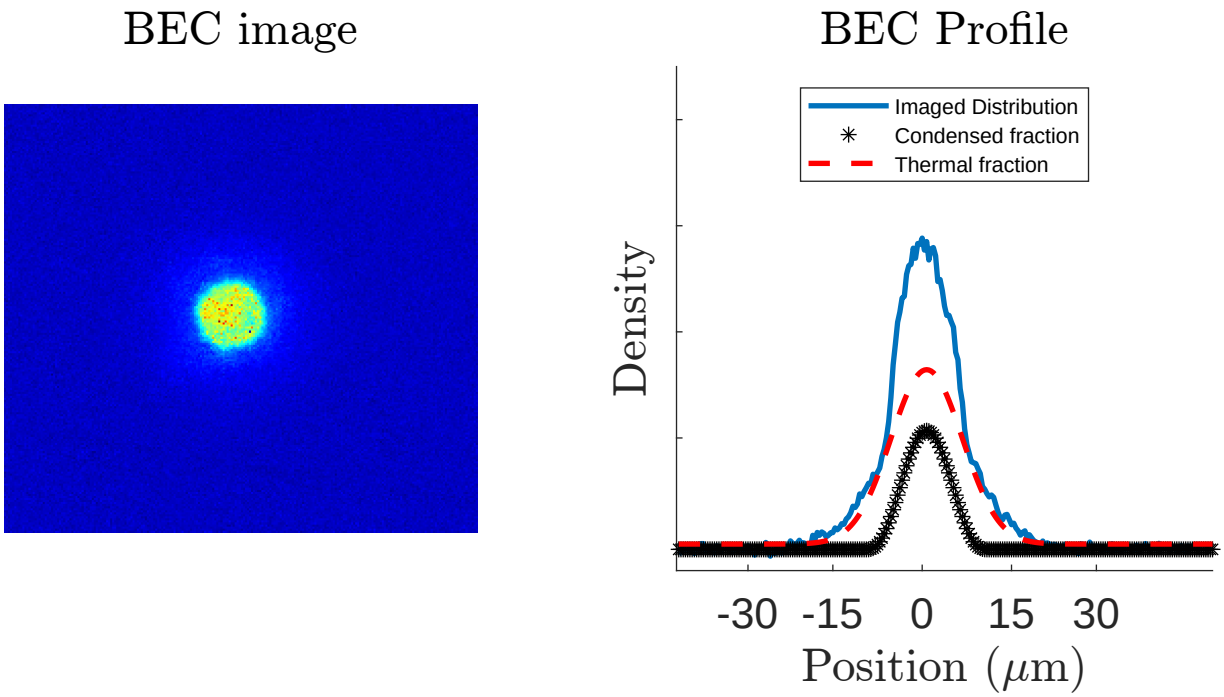

Fig. 1.4: BEC profiles. The left panel shows an example image of a BEC taken in our lab after no free expansion. The right shows an integrated density profile, with a bimodal fit (Gaussian + parabolic profiles) to distinguish the thermal fraction and the condensate.

difference between the parabolic profile and the background thermal fraction is shown.

BECs are the backbone of the experiments discussed in this thesis, and are the main tool used in the lab to explore quantum dynamics and localization behavior. In the next few sections, I'll discuss some of the tools we use to control BECs in coherent ways.

1.5 Feshbach Resonances

As stated earlier, a key feature of ^{7}Li is the tunability of its interatomic interaction strength via a Feshbach resonance. Feshbach resonances have been studied theoretically and experimentally for decades, as outlined nicely in [8], and have served as useful tools for controlling interactions and creating molecules.

The basic concept of a Feshbach resonance can be understood by analyzing the be-

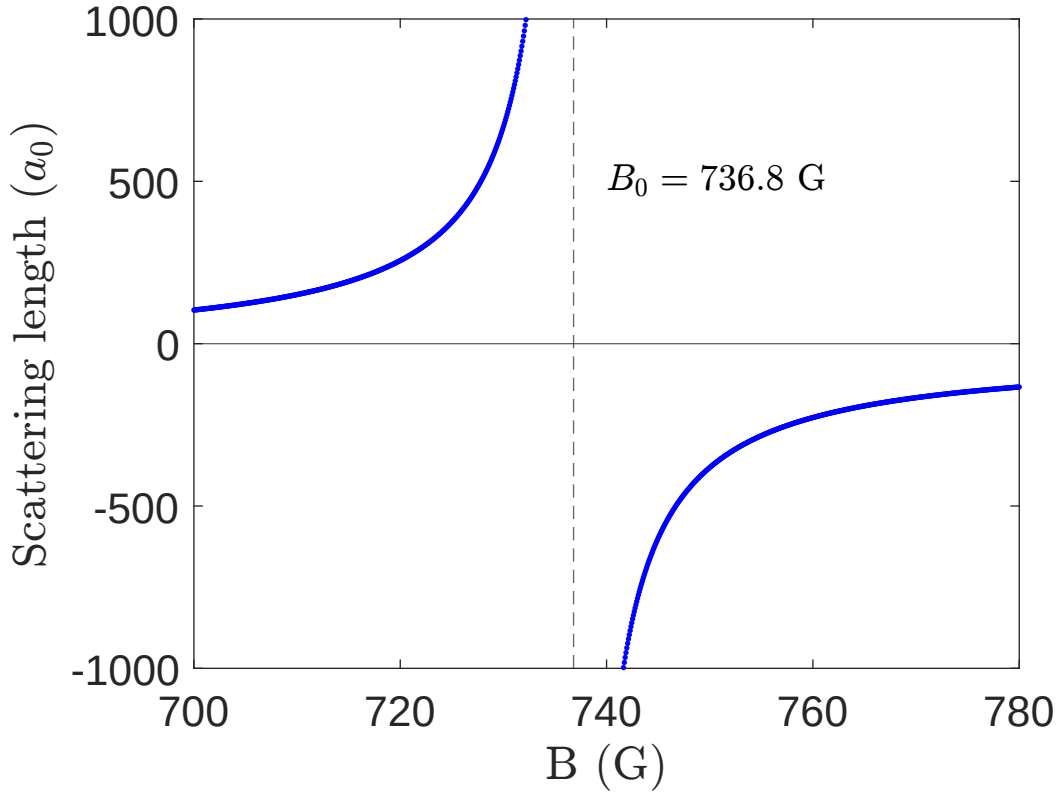

Fig. 1.5: Functional form of the scattering length around the Feshbach resonance.

havior of two atoms in a scattering event. After a collision, the atoms can occupy one of a few *exit channels*, namely they can scatter off of one another or form a bound state. If the bound state and scattering state have different magnetic moments, their relative energy can be tuned by the application of a DC magnetic field. A Feshbach resonance occurs when the energies of the two exit channel states are approximately equal, and at this resonance there is significant mixing between the bound and scattered state. In the vicinity of the Feshbach resonance, the s-wave scattering length becomes a function of the magnetic field with the form:

$$a(B) = a_{bg}(1 - \frac{\Delta}{B - B_0}) \tag{1.12}$$

where a_{bg} is the background scattering length, B_0 is the magnetic field at the location of the Feshbach resonance, and Δ is the width of the resonance. The zero crossing, where $a(B) = 0$, occurs at $B = B_0 + \Delta$. For ^{7}Li, $a_{bg} = -24.5$, $\Delta = -192.3$, and $B_0 = 736.8$G, all characterized in [9]. The functional form is shown in Fig. 1.5.

We use an H-bridge to switch our magnet coils from an anti-Helmholtz configuration to a Helmholtz configuration, and tune the current in the coils via a high power current supply to achieve our desired interaction strengths. Characterization of the scattering length can be done via holding the BEC in a dipole trap and looking at cloud expansion [9], or elastic and inelastic collisional loss rates [10]. From Fig. 1.5, it is also evident that near the resonance the scattering length can change by hundreds of a_0 over just a few Gauss, and therefore magnetic field stability is key when investigating the regime of large interactions. This is currently a very active area of improvement on the lithium machine.

1.6 Optical lattices

While BECs are interesting on their own, the physics can be leveled up a notch by having them interact with an optical lattice. An optical lattice is simply a retroreflected far red-detuned laser beam (1064 nm for our setup), which creates a standing wave potential at the atoms. The single particle Hamiltonian for a 1D optical lattice is

$$H = \frac{\hat{p}^2}{2m} + V_0 \cos^2(k_L x) = -\frac{\hbar^2 \partial_x^2}{2m} + \frac{V_0}{2}(1 + \cos(2k_L x)) \tag{1.13}$$

where V_0 is the lattice depth and $k_L = 2\pi/1064$nm is the lattice wavevector. The constant term $V_0/2$ is typically dropped for simplicity. This Hamiltonian emulates a system commonly studied in condensed matter systems — an electron moving in an atomic

lattice — and thereby provides an novel platform for **quantum simulation**. Bloch's theorem applies due to the discrete spatial translation symmetry, and the eigenstates can be written in the typical form of Bloch wavefunctions:

$$\psi_{n,k}(x) = u_{n,k}(x)e^{ikx} \tag{1.14}$$

The Hamiltonian 1.13 is convenient to use when ψ is expressed in the basis of plane waves:

$$\psi(x,t) = \sum_n c_n(t)e^{2nk_Lx}. \tag{1.15}$$

Plane waves are eigenstates of the kinetic energy operator, ie. if $|n\rangle = e^{i2nk_Lx}$, then

$$\partial_x^2 |n\rangle = -4n^2k^2 |n\rangle . \tag{1.16}$$

The lattice term can be decomposed as follows:

$$\frac{V_0}{2}\cos(2k_Lx) |n\rangle = \frac{V_0}{4}(e^{i2k_Lx} + e^{-i2k_Lx}) |n\rangle = \frac{V_0}{4}(|n-1\rangle + |n+1\rangle) \tag{1.17}$$

The lattice acts as a coupling to adjacent plane wave states! This form allows for easy diagonalization of the Hamiltonian as well as computation of the band structure, which act as a starting point for further quantum dynamics experiments. As an example, we can add one more term to the Hamiltonian of the form Fx, where F is an applied force. This gives rise to the famed *Bloch oscillation*, whereby a particle in a periodic potential under the application of a linear force will oscillate. This is due to the Bragg scattering condition off of the Brillouin zone edge. Typically this phenomenon is extremely difficult to observe in electron systems due to rapid decoherence, but ultracold atomic systems provide the perfect platform for its observation [11] due to their isolation and increased

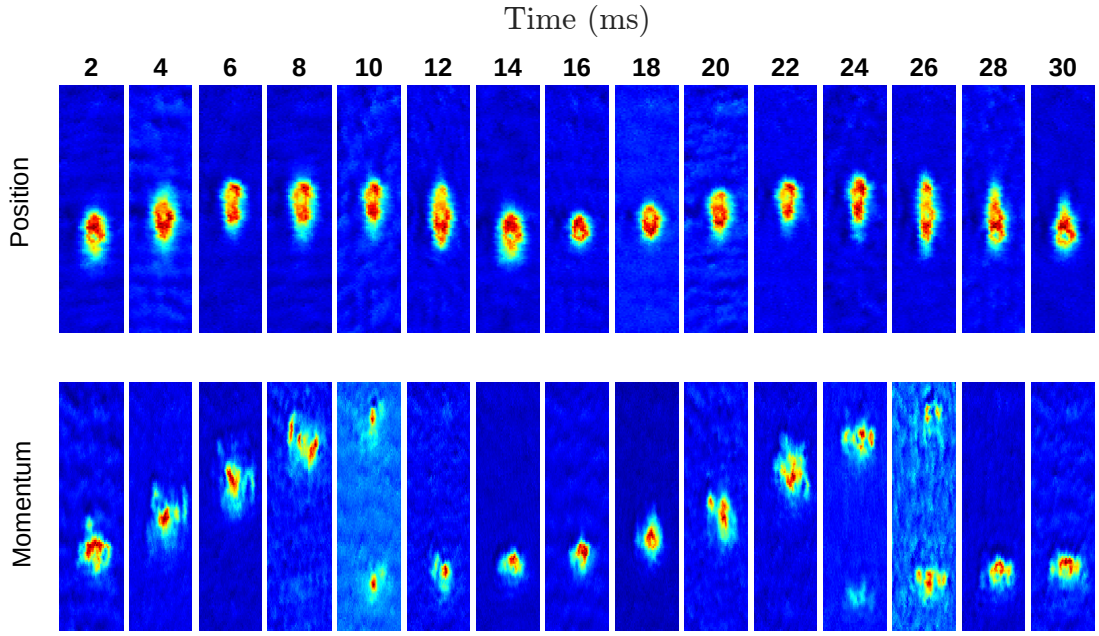

Fig. 1.6: Position and momentum space Bloch oscillations of a BEC in an optical lattice.

quantum control. An example of this phenomenon is shown in Fig. 1.6. The top row shows in-situ images of a ^{7}Li BEC in an optical lattice under the application of a force, demonstrating an oscillation in position space. The bottom row shows the atomic images after a time of flight (TOF), projecting the atoms into momentum space. The "jumps" correspond to when the atoms scatter off of the Brillouin zone.

1.7 Kapitza-Dirac Diffraction

For the experiments discussed in this thesis, the lattice is pulsed periodically in time, rather than operated in steady state. In the regime where the pulse duration is much shorter than atom dynamics, coherent scattering of the matter wave off of the lattice can occur, a phenomenon known as Kapitza-Dirac diffraction, analagous to optical diffraction off of a physical grating. This effect is most simply understood in the Raman-Nath regime, where the kinetic energy of the atoms can be neglected in the Hamiltonian, equivalent

to the thin lens approximation in optics. This is well approximated when the atom-light interaction time (experimentally, the pulse duration) is much shorter than the timescale of the recoil frequency, $\tau << 1/\omega_{rec}$. For ^{7}Li interacting with 1064 nm light, $\omega_{rec} = 25.18$ kHz, so pulses must be much shorter than 40μs. Experimentally, the pulses used in this thesis range from 300 ns to 5μs, satisying this criteria.

The physics of Kapitza-Dirac diffraction is fully described in [12]. However, there are some easier points of intuition that can be understood without full mathematical rigor. Firstly, the interaction with the pulsed optical lattice provides a means of transferring momentum to the atoms. This is achieved via absorption of a photon with momentum $\hbar k_L$ from one lattice and stimulated emission of a photon with momentum $-\hbar k_L$ into the counterpropagating lattice, changing the momentum of the atom by a quantized amount of $2\hbar k_L$.

Mathematically, a kick with the lattice can be written as a propagator of the form $e^{-iV\tau\cos(2k_Lx)/\hbar}$, with V the lattice depth and τ the pulse duration. Using the Jacobi-Anger expansion, the propagator can be written as

$$e^{-iV\tau\cos(2k_Lx)/\hbar} = \sum_{n=-\infty}^{\infty} (-i)^n J_n\left(\frac{V\tau}{\hbar}\right) e^{i2nk_Lx} \tag{1.18}$$

where J_n is the nth Bessel function of the first kind. From the summation we can see that the lattice kick couples the atoms to adjacent momentum states with spacing $2\hbar k_L$, and the probability of populating a $2n\hbar k_L$ momentum state is proportional to $J_n^2(V\tau)$. Experimentally, after pulsing the lattice to achieve this coupling, we can allow the atoms to undergo a free expansion (which I'll refer to as a TOF, or time-of-flight, for the remainder of this thesis) such that these momentum components resolve themselves spatially, shown in Fig. 1.7. Larger lattice depths allow for more significant coupling to higher momentum orders.

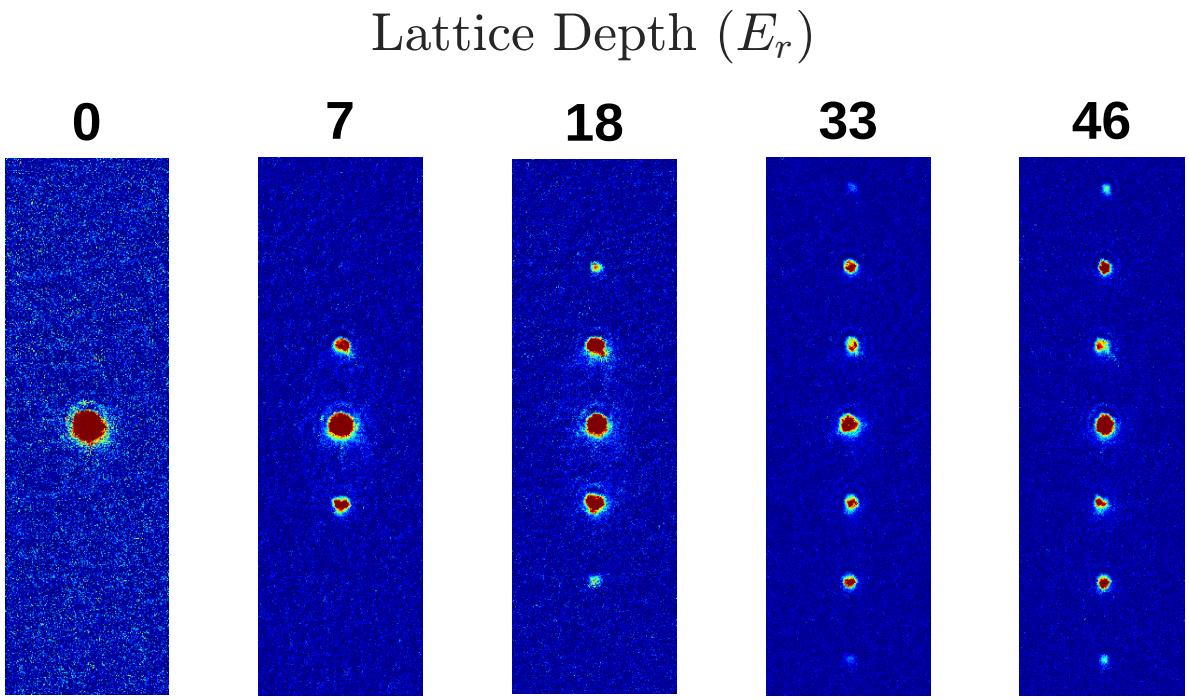

Fig. 1.7: Kapitza-Dirac Diffraction. Images are of BECs subjected to a 3 μs optical lattice pulse of varying depth, followed by a 2 ms free expansion. The spatial separation of each order to its neighbors is ≈ 200 μm.

This phenomenon will become relevant again in chapters 3 and 4, but I'll also mention that it provides a useful mechanism for calibrating the optical lattice depth. We can count the number of atoms in each momentum order and compare the result to a numerical TDSE simulation, accounting for finite width effects of both the BEC and lattice beam. This is nicely outlined in [3].

1.8 Anderson Localization

So far in this chapter I have discussed properties of BECs and their interaction with optical lattices, but zooming further out, what outstanding questions in physics can be explored with these quantum systems? A key use case is *quantum simulation*, specifically the ability to replicate and explore Hamiltonians describing other physical systems,

typically in condensed matter. One fundamental example of this is the concept of *Anderson localization*. Anderson localization is a phenomenon whereby wave propagation is suppressed in the presence of disorder. It was first suggested by P. W. Anderson [13], who argued that electrons could localize in an atomic lattice if enough randomness is present, ie. through defects or impurities. This behavior is present in a variety of physical systems, including semiconductors, photonic waveguides [14], and disordered optical potentials [15], and provides a simple and useful framework for studying condensed matter systems.

For a 1-D lattice in the tight-binding limit, the Anderson Hamiltonian is

$$H = -J \sum_{ij} (c_i^\dagger c_j + c_j^\dagger c_i) + \sum_i \epsilon_i c_i^\dagger c_i, \tag{1.19}$$

where J is the hopping amplitude, $c_i^\dagger$ and c_i represent the fermionic creation and annihilation operators for site i, and ϵ_i is a random on-site energy at site i, drawn from a uniform distribution [-W/2, W/2] where W represents the amount of disorder.

There are a few observations to be made here. In the disorder free case W=0, the second term in the Hamiltonian goes to 0, the remaining term is translationally invariant, and the eigenstates are simply Bloch waves. These states are maximally delocalized through the system. The infinite disorder case $J/W \to 0$ is also straightforward, with eigenstates taking the form $\psi_i(j) = \delta_{i,j}$. Intuitively, these eigenstates are localized to one site, and an initial eigenstate in this limit will stay localized for all time t.

The interesting behavior in the Anderson model arises when there is competition between the hopping term and the disorder. In Anderson's original work [13], he suggested for strong but finite disorder, diffusive propagation will vanish for a quantum particle. This occurs due to wave interference, as amplitudes which propagate away from the origin

destructively interfere. In 1D and 2D, the amount of disorder required for localization to occur is arbitrarily small, while in 3D there is a transition between the localized and delocalized phases.

I've provided example MATLAB code for the 1D tight-binding model so new physicists can explore the behavior themselves:

```
%Initialize parameters and create Hamiltonian
sites = 100; J = 1; W = 10;
eps = W*rand(1,sites)-W/2; %Random between [-W/2, W/2]
H = diag(eps.*ones(1,sites)) + diag(-J*ones(1,sites-1),1) +
   diag(-J*ones(1,sites-1),-1);

% Initial localized state in 1 site
init(round(sites/2)) = 1;

%Prepare propagator
U = expm(-1i*H);

steps = 20;
%Matrix to save position distribution
px = zeros(length(init),steps+1);
px(:,1) = init.*conj(init);

%Time evolution
for ii = 2:steps+1
```

```
    init = U*init;
    px(:,ii) = init.*conj(init);
end
figure(1)
imagesc(px)
```

The parameters J and W can be varied, and the change in localization behavior can be easily observed, as seen in Fig. 1.8. Because the potential is randomly generated for each instance of the program, the results will vary for intermediate values of J/W, and the true behavior can be gleaned from averaging over many instances of the randomness.

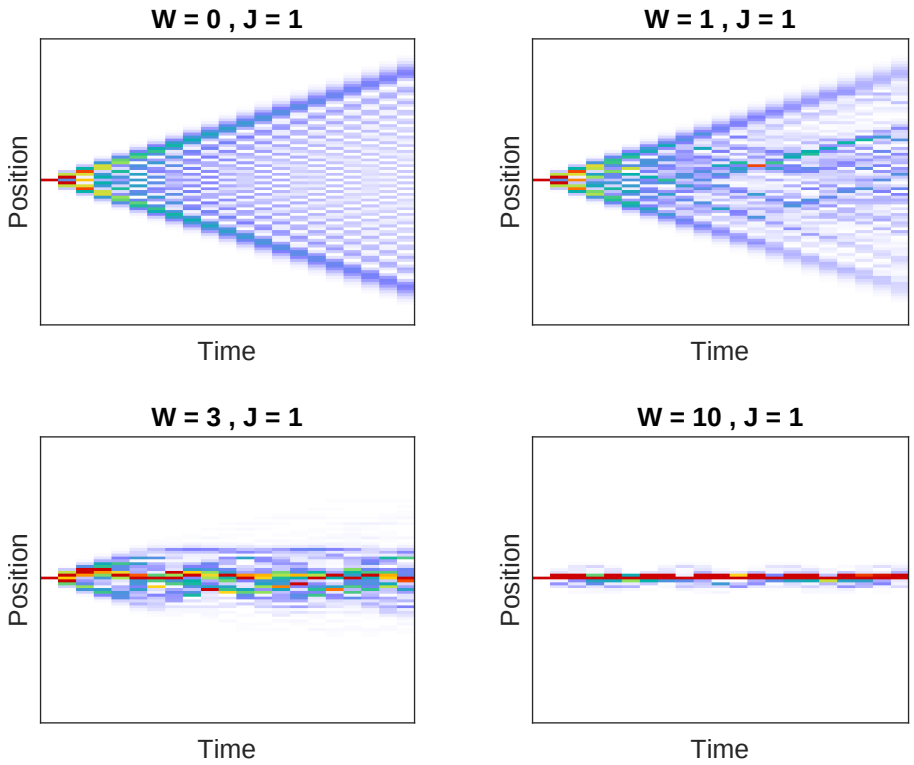

Fig. 1.8: Position space distribution of a quantum particle during evolution in a 1D Anderson localized system for varying randomness W.

Chapter 2

Experimental Apparatus and Creating Ultracold Atoms

This chapter describes the apparatus used for the experiments discussed in the rest of the thesis. The physical nature of the lithium BEC machine will be described, followed by an explanation of the sequence used to cool atoms to quantum degeneracy. Aspects of optical lattices, imaging, and control software are discussed in more detail towards the end of the chapter.

2.1 ^{7}Li Bose Einstein Condensate Apparatus

Our experimental apparatus is a 10 foot long ultra-high vacuum (UHV) chamber which generates BECs of ^{7}Li. The procedure required to cool lithium to quantum degeneracy is quite involved, but successfully creates robust and reliable BECs of up to 1 million atoms. For more in-depth discussion on the construction of the apparatus, see [1–3]. A model of the machine is shown in Fig. 2.1, which will serve as a useful reference throughout this section. To clarify the orientation for the rest of the chapter,

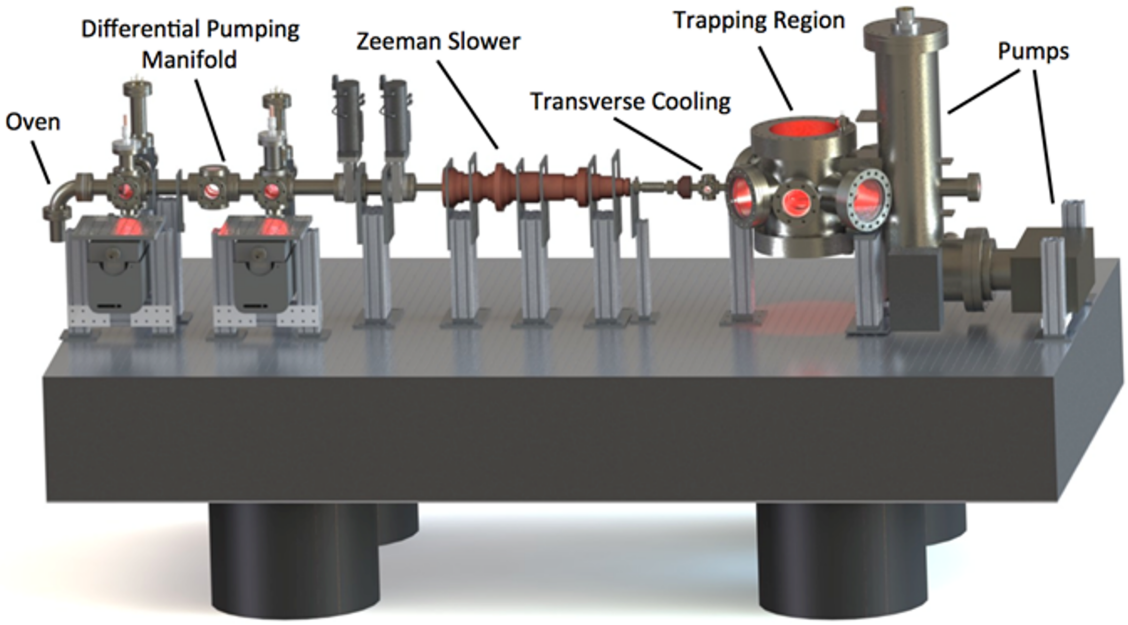

Fig. 2.1: CAD model of the UHV lithium BEC machine. The atoms come out of the oven section at speeds of 1 km/s, and are progressively cooled until they reach a final temperature of 10 nK in the trapping region.

the oven is the north (N) side of the machine, and the trapping region is south (S).

The first (leftmost) part of the vacuum chamber is half-nipple attached to an elbow, an oven housing a 25g roll of lithium heated up to 500C. The heated lithium becomes a dilute vapor which exits the oven via a nozzle, created by placing 660 stainless steel microcapillary tubes into a triangular groove. The nozzle collimates the atoms into a beam by only passing atoms with small transverse velocities, with a divergence half-angle of 1.2°. This atomic beam first passes through a cold plate, an aluminum block with a 1/2" diameter aperture that collects stray lithium atoms with larger divergence angles. The cold plate is inserted into the vacuum chamber via a copper feedthrough.

As a brief aside, in the fall of 2023 we replaced the oven after running out of ^{7}Li in the oven after 4.5 years of use. After replacing the oven, we baked the oven at 560C for a week, which caused a buildup of lithium on the old cold plate. Be wary of this if increasing the oven temperature. Buildup on the cold plate can be seen by looking

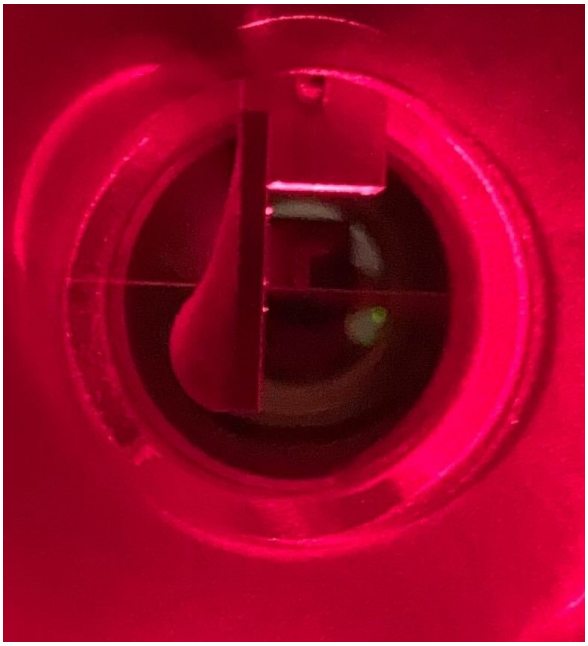

Fig. 2.2: Buildup of lithium on the old cold plate due to high oven temperatures. The deposit blocked the aperture for the atomic beam, resulting in a lower flux into the trapping chamber. This can be seen by eye when looking at the atomic beam before and after the cold plate, with a drastic reduction in beam fluorescence at the output.

through the first viewport of the chamber after the oven 2.2. The newly machined cold plate has a larger hole (1/2" instead of 3/8" diameter), and is placed slightly lower such that the beam passes through closer to the center of the hole 2.3.

After the cold plate there is a section of transverse cooling (TC) to further collimate the atomic beam. This is accomplished by taking both cycler and repump light, red-detuning their frequencies by 3Γ, and aiming them at the atomic beam from the horizontal and vertical viewports after the differential pumping tube. Both beams are retroreflected to allow for full 2D steering. Traditionally, only the horizontal TC beam has provided an advantage for the loading rate of magneto-optical trap (MOT), but that condition can change if the atomic beam direction changes. Both beams are expanded via a cylindrical telescope along the atomic beam direction to maximize coverage of the atoms. This TC is crucial for the cooling sequence, as we've traditionally seen gains of 1.5-2x in the

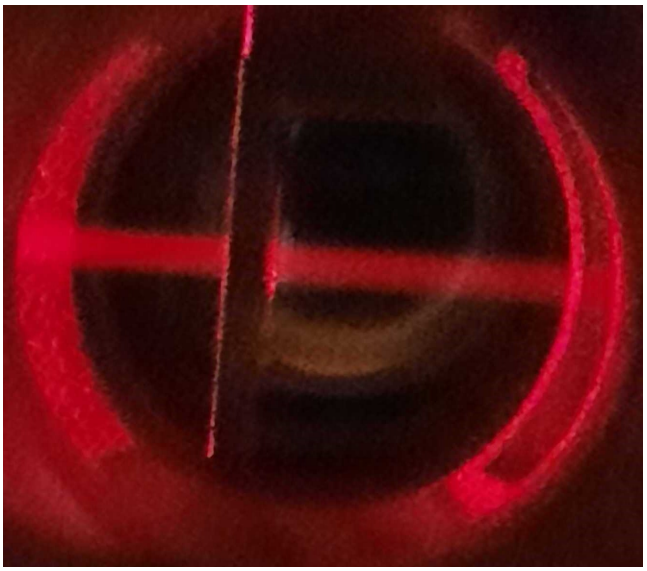

Fig. 2.3: Newly machined coldplate with no lithium buildup.

fluorescent MOT load rate when using it. The estimated saturation parameter for the beam is .2 ($I_{sat} = 2.54\,\mathrm{mW/cm^2}$), and the addition of power into this beam has never seen a roll off in MOT load increase. Future generations could think of installing a separate tapered amplifier (TA) for TC as an option to increase MOT load rates.

Following the first TC section, there are 2 gate valves to separate the different sections of the UHV system. The extra one is for redundancy, but these allow for replacement or repair of one section of the machine without damaging the vacuum of the other.

While the atomic beam propagates through the UHV chamber, there is a counter-propagating 671 nm laser beam, which we refer to as the *Zeeman slower beam*, that originates at the other end of the chamber. The purpose of the slower beam is to cool the atoms as they progress. Since the atoms slow down as they move closer to the science chamber (due to interacting with more photons), they begin to fall out of resonance with the slower beam. To compensate for this, there is a 1m long Zeeman slower placed before the science chamber to complete the initial cooling of the atoms. The Zeeman slower is a tapered solenoid that adjusts for the changing Doppler shift by applying a spatially

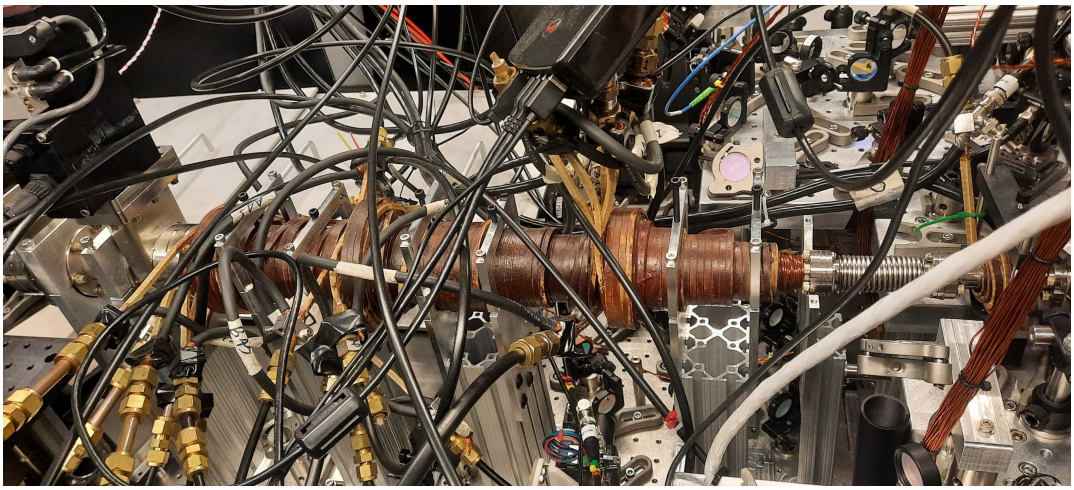

Fig. 2.4: Li Zeeman slower.

dependent magnetic field. This applied Zeeman shift allows for cooling velocity classes down to < 50m/s, the velocities necessary to capture the atoms in a magneto-optical trap (MOT). To first order, the Zeeman shift is

$$\Delta E_Z = g_F m_F \mu_b B, \tag{2.1}$$

which corresponds to 1.4 MHz/G for the ^{7}Li D2 transition. After the Zeeman slower is one more section of TC, to collimate the atomic beam before entry into the main chamber. Importantly, the detuning of this second stage of TC (known as TC2) is smaller than the detuning of the first stage of TC (TC1) to compensate for the fact that the average transverse velocity class is slower further down the machine.

The main chamber has 5 optical access axes. There are 4 parallel to the X-Y plane of the chamber, allowing for all horizontal arms of the various cooling stages. The N-S axis viewports allow for the atomic beam to enter the main chamber from the north and the slower beam to pass through from the south. The NW-SE and NE-SW axes have four 6" diameter viewports which allow access for MOT, gray-molasses (GM), and dipole-trapping beams, which are more thoroughly described in the following sections.

The last planar axis, W-E, has one re-entrant window and is used both for an extra pair of MOT beams (the initial six beam MOT was insufficient due to a physical constraint of 65° on the horizontal MOT arms, so there are now 8 beams), as well as the optical lattice optics. The last axis, running from the top to the bottom of the chamber, has two re-entrant windows which allow for close placement of the MOT and Feshbach coils to the atoms. This is also the main imaging axis of the apparatus. All chamber viewports are anti-reflection coated for 671 nm and 1064 nm, but only the top and bottom are also coated for 532 nm, the wavelength used for the plug beam during the magnetic evaporation stage.

2.2 Cooling Sequence

This section will detail how to cool a dilute gas of ^{7}Li to quantum degeneracy. More information can be found in [1, 3].

2.2.1 Magneto-Optical Trap

After the atoms travel through the UHV apparatus into the main chamber, they are captured in a magneto-optical trap (MOT). For our setup, this is a combination of eight red-detuned 671 nm laser beams and a quadrupolar magnetic field. The laser beams create an optical molasses that covers all spatial axes, and the quadrupolar magnetic field applies a spatially-dependent Zeeman shift to bring atoms back into resonance with the cooling beams as they move away from the trap center. The beams are all σ^+ or σ^- polarized to ensure the atoms resonantly absorb photons from the beam that will push them back towards the magnetic field zero location. A schematic of a MOT is shown in Fig. 2.5.

The force created by the MOT can be understood by utilizing the equation for the

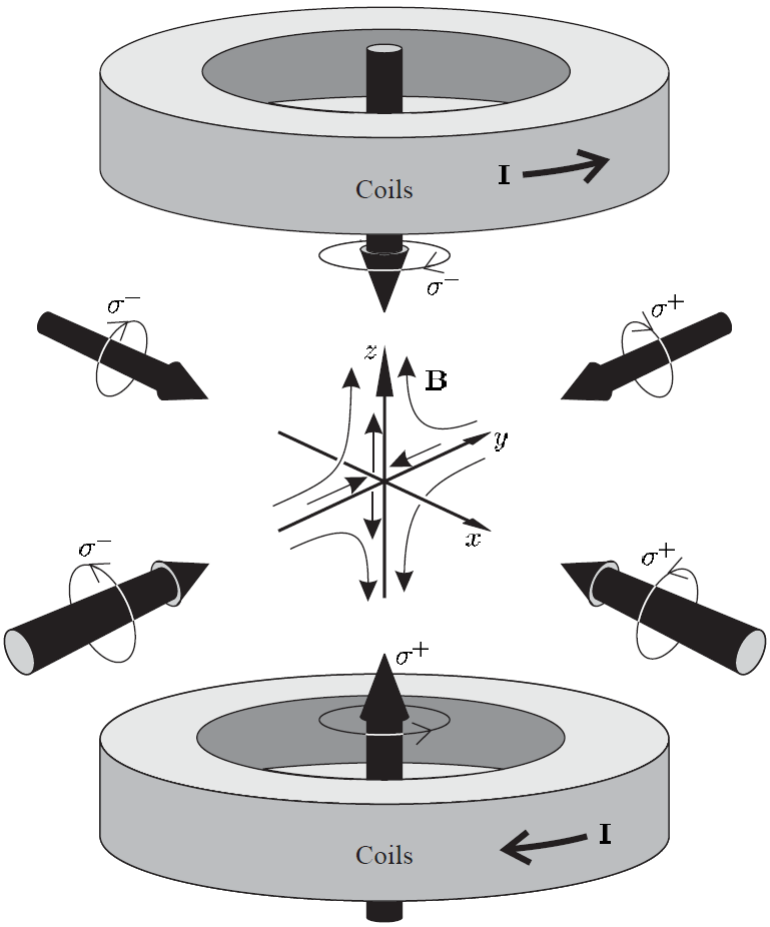

Fig. 2.5: Schematic of MOT taken from [4]. Coils with current running in the anti-Helmholtz configuration generate a quadrupolar magnetic field, while 6 laser beams provide optical cooling along all 3 spatial axes.

scattering force 1.1:

$$F_{MOT} = F^{\sigma^+}_{scatt}(\omega - kv - (\omega_0 + \beta z)) - F^{\sigma^-}_{scatt}(\omega + kv - (\omega_0 - \beta z)) \qquad (2.2)$$
$$\approx -2\frac{\partial F}{\partial \omega} kv + 2\frac{\partial F}{\partial \omega_0}\beta z.$$

The first term ($\propto v$) acts like a drag force, while the second term acts as a restoring force, with βz representing the spatially dependent Zeeman shift.

Since the upper manifold of hyperfine states is unresolved for the D2 transition in

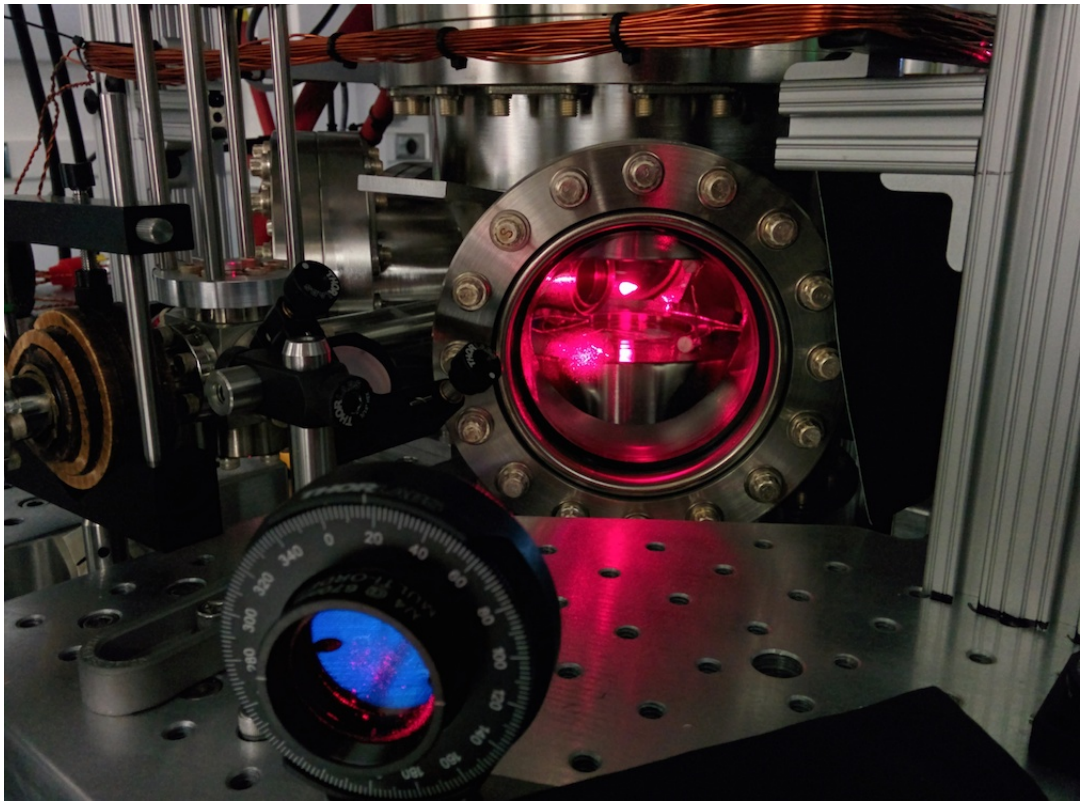

Fig. 2.6: Picture of our ^{7}Li MOT in the lab. The fluorescence is due to atoms emitting 671 nm photons after absorbing the laser cooling light.

^{7}Li, the atoms can decay into the $F = 1$ or $F = 2$ ground state in the $2S_{1/2}$ manifold after being excited. This requires each MOT beam to have two colors: a "cycler" which addresses the $F = 2$ to $F' = 3$ transition, and a "repumper" which addresses the $F = 1$ to $F' = 2$ transition. These are separated by the ground state splitting of 803.5 MHz, and empirically we've found that both require roughly the same amount of power to optimize MOT loading. To generate the quadrupolar magnetic field, a current is driven through a pair of anti-Helmholtz coils placed above and below the atoms (see Fig. 2.5). The typical gradient created by these coils is ≈ 20 G/cm.

In the experiment we typically load the MOT for 15 s, capturing $\approx 10^9$ atoms. The MOT can be seen by eye due to the emitted photons from the atoms (Fig. 2.6), and this fluorescence can be captured on a photodiode. Since the MOT plays a large role in

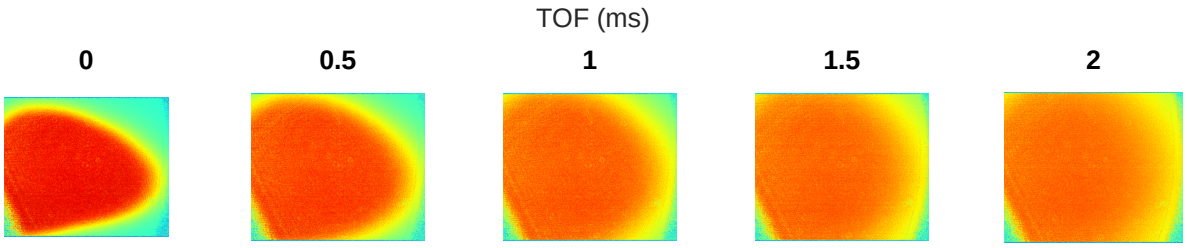

Fig. 2.7: Images of atomic cloud for increasing times of flight after the MOT stage. The overall length and width of each image is $\approx$ 5mm.

the atom number used in experiments, we try to maintain consistency by measuring the fluorescence and triggering the next stage of the cooling sequence to start after the MOT reaches a specific threshold photodiode voltage. We typically take diagnostic images from the top for various times of flight (TOFs) to gauge this consistency. An example of one such run is shown in Fig. 2.7. In the next stage, the compressed MOT (CMOT), we bring the cycler closer to resonance by 2.5Γ, decrease the repump intensity to near 0, and increase the magnetic field gradient by a factor of 5 for 28 ms, increasing the density of the MOT by a factor of 2 before entering the GM stage.

I have a few notes about the MOT for future students. My mentor Cora used to say "a MOT only has three components: atoms, lasers, and magnets". Indeed, when debugging MOT issues this has always stuck with me. When running the machine and discovering the lack of a MOT, there are only a finite number of things that can be preventing it, all of which fall into one of the three components. I've outlined some of them below:

1. Atoms
   (a) Beam shutter is closed
   (b) Oven has run out of lithium (this only happens once every 5 years or so)
2. Lasers

(a) MOT AOMs are not switched on

(b) MOT beam polarization has drifted

(c) MOT beam power has dropped

(d) Spectroscopy is not locked, or the frequency has shifted (rare but has happened)

(e) Zeeman slower beam is not locked

(f) Transverse cooling is blocked or subpar

3. Magnets

(a) Magnets are not turned on

(b) Magnets are not in anti-Helmholtz configuration

(c) Magnets do not have appropriate current running through them

The MOT can only theoretically cool atoms down to the Doppler temperature ($\approx$ 140 μK for the D2 transition), and experimentally the temperature ($\approx$ 1 mK) is well above this limit due to imperfections. To get to colder temperatures, we next employ a *sub-Doppler* cooling technique known as gray molasses (GM).

2.2.2 Gray Molasses

GM is a variant of Sisyphus cooling, aptly named in its analogy to the punishment of Sisyphus in Greek mythology, who is forced to roll a boulder up a hill for all of eternity. In our case, the scheme involves getting atoms to "roll" up a potential hill while losing kinetic energy, followed by an excitation and pumping procedure to bring them back to the bottom of the hill. Repeating this procedure many times successfully cools the atoms to sub-Doppler temperatures.

The theory of GM is well outlined in [16, 17], but I'll give an intuitive picture for ^{7}Li and our setup here. GM utilizes a two-photon Raman transition between the two hyperfine ground states off-resonantly coupled to an excited state, in our case using the D1 transition to the $2P_{1/2}$ state. Light is applied to the atoms near this two-photon resonance condition and is retroreflected, creating a spatially modulated AC-Stark shift along each axis. In the dressed-state picture, orthogonal superpositions of the electronic ground states act as a convenient basis, with one "coupled" state $|\psi_c\rangle$ undergoing transitions to the excited state $|\psi_e\rangle$ while the "noncoupled" state $|\psi_{nc}\rangle$ remains completely dark to it.

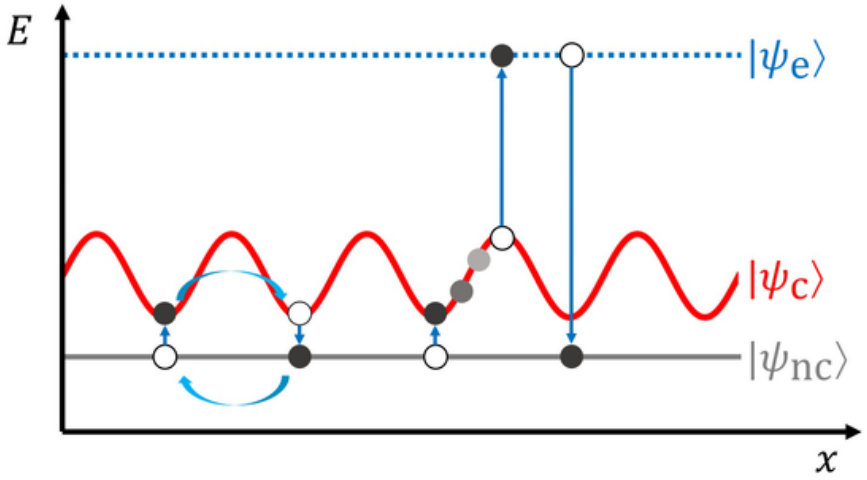

Fig. 2.8: Energy diagram of the gray molasses scheme. Image taken from [18].

The life of an atom in this cooling scheme goes as follows, depicted in Fig. 2.8:

1. An atom starts in $|\psi_c\rangle$ at the bottom of a potential well due to the periodic Stark shift created by the laser.

2. Under time evolution in the atom-light interaction, the atom moves up the potential hill, losing kinetic energy along the way.

3. At the top of the hill the atom is excited to $|\psi_e\rangle$, as $|\psi_c\rangle$ couples to $|\psi_e\rangle$ via dipole

transitions mediated by the laser.

4. By spontaneous emission the atom enters $|\psi_{nc}\rangle$ from $|\psi_e\rangle$.

5. $|\psi_{nc}\rangle$ is optically dark to the laser, so the relevant Hamiltonian is now just the kinetic energy operator. Since $|\psi_{nc}\rangle$ and $|\psi_c\rangle$ are not eigenstates of the momentum operator, $|\psi_{nc}\rangle$ can evolve into $|\psi_c\rangle$ under free evolution with a frequency proportional to the momentum. Thus, hotter atoms are preferentially selected to enter step 1 again.

6. Steps 1 through 5 are repeated until the atoms no longer have the energy to climb the potential hill.

Or GM scheme typically cools the atoms down to 50 μK while maintaining a majority of the atoms from the MOT. This allows for significant capture in the next stage, the magnetic trap. Example images of the atomic cloud for various TOFs are shown in Fig. 2.9. In-depth descriptions of the physical setup of GM can be found in [1, 3]. The one crucial feature of the optical path is the presence of a 9.2 GHz EOM which is used to shift the laser table light from D2 to D1, as the D1 excited state manifold is resolved and thus can be used for a two-photon Raman scheme. The main beam is passed through the EOM and injection locked to a slave laser, which is used to seed a tapered amplifier on the main apparatus table to obtain the appropriate amount of power. The beam is then passed through an 803.5 MHz EOM to generate the second frequency for the two-photon scheme, equivalent to the ground state splitting. Finally, the beam is split into two paths: one which travels through the horizontal plane of the main chamber and is retroreflected in a bow-tie configuration, and another which travels along the vertical axis starting at the bottom of the chamber and is retroreflected after going through the top bucket window.

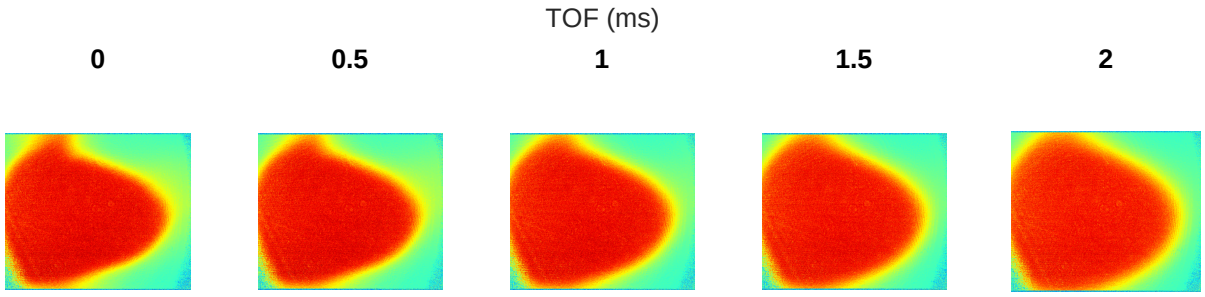

Fig. 2.9: Images of atomic cloud for increasing times of flight after gray molasses. The overall length and width of each image is $\approx$ 5mm. The cloud experiences very little expansion over the range of TOFs shown, highlighting the drastic decrease in temperature compared to that of the MOT. The wisp at the top of the first few images are atoms leaving the trap due to misalignment between the MOT and GM beams. Minimizing this loss is typically a useful way to ensure the GM beams are well aligned.

2.2.3 Magnetic Trap and RF Evaporation

The next stage in our cooling sequence involves loading the atoms into a pure magnetic trap. The reason for doing so is because laser cooling techniques can only achieve temperatures down to around 50μK, after which evaporative cooling techniques must be used. This is analagous to cooling that occurs for a hot cup of coffee, which cools down when thermal energy is carried away by hot atoms in steam. The atoms remaining rethermalize via collisions and achieve a colder temperature. Crucially, this cooling is only limited by atom number, and allows us to achieve temperatures lower than the BEC transition temperature.

^{7}Li's ground state has eight magnetic sublevels, three for the $F = 1$ state and five for the $F = 2$ state. Since the g-factor is positive for the $F = 2$ state and negative for the $F = 1$ state, the states that are magnetically trappable are $|F, m_F\rangle = |2, 2\rangle, |2, 1\rangle,$ and $|1, -1\rangle$, as their energies increase with increasing magnetic field due to a positive Zeeman shift 2.1. In a quadrupolar magnetic field, this corresponds to atoms needing more energy as they move away from the zero-field point. The rest of the magnetic sublevels are either untrapped or antitrapped.

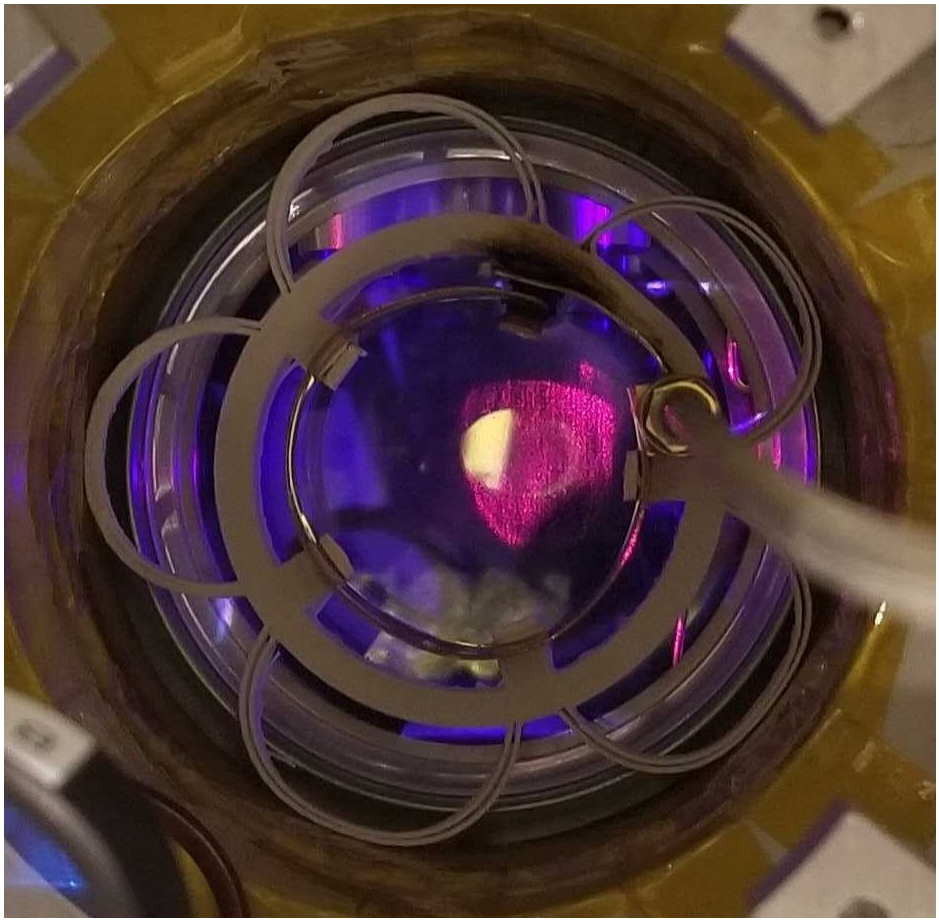

Fig. 2.10: Lithium RF antenna on top of the main chamber. The antenna is a single spiral of flat copper wire mounted in a 3D printed PLA mount.

In order to get the atoms to a magnetically trappable state, we utilize an optical pumping procedure where we shine σ^+ light resonant with the D1 transition for 450 μs while applying a DC magnetic field to create a weak quantization axis parallel to the light. The σ^+ transitions preferentially transfer the atoms to higher m_F levels until they reach the $|2,2\rangle$ state, at which point they become optically dark. Since the atoms can fall from the excited $2P_{1/2}$ state into the $F = 1$ ground state, we apply a second frequency of light shifted 803.5 MHz to address the D1 transition from the $F = 1$ state. This is achieved by passing the spin-polarizing light through an 803.5 MHz electro-optic modulator (EOM) and increasing the amplitude of the sideband.

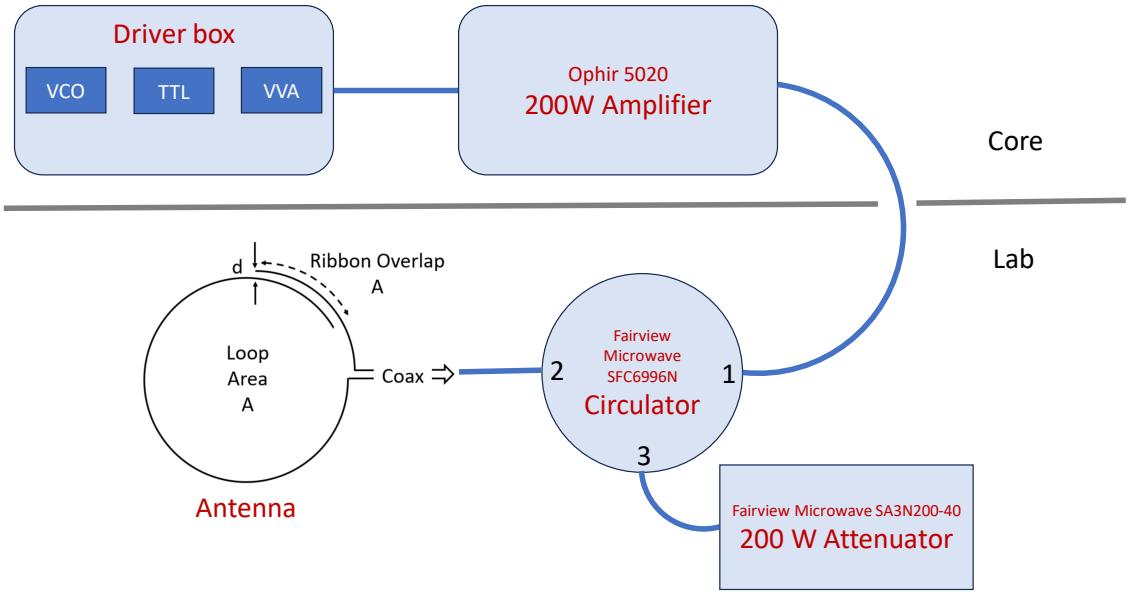

Fig. 2.11: Schematic of electronics which generate the frequency sweep for RF evaporation. Antenna picture taken from [1].

Once the atoms have entered the $|2,2\rangle$ state, they are loaded into the magnetic trap created by the same coils used for the MOT. The coils are ramped in 150 ms. Historically, a high-voltage capacitor bank was used to accelerate the ramp, achieveing 100 G/cm in as little as 100 μs, but this is no longer used due to not showing any benefit empirically. The final gradient for the magnetic trap is much larger than that of the MOT, typically 420 G/cm compared to 20 G/cm.

Once the atoms are loaded into the magnetic trap, we perform evaporation via an RF knife. The top of the main chamber has a homemade single spiral antennna, shown in Fig. 2.10, tuned to be resonant around 800 MHz for this purpose. The RF is swept from a frequency of 927 MHz to 805 MHz, progressively expelling the hottest atoms (which are closer to the edges of the trap). This is an extremely lossy process where over 90% of the atoms are removed from the trap.

A schematic of the RF setup is shown in Fig. 2.11. The initial RF is generated in a

driver box typical of those found in the lab, with a VCO, TTL, and VVA to control the frequency, on/off state, and amplitude respectively. The RF is then fed into an Ophir 5020 200W amplifier, which is necessary due to the antenna being ex situ to the chamber. Before my time, there was a feedthrough placed within the chamber to avoid this massive power draw, but unfortunately this was broken during the initial main chamber bake. The driver box and amplifier are kept on the other side of the lab wall (in the core, aka the bowels of Broida Hall) to prevent stray RF reflections from interfering with lab electronics. The amplified RF signal goes through a circulator into the antenna, after which it gets dumped into a 200W RF attenuator.

At the center of the trap the magnetic field goes to 0, which causes the atoms to undergo *Majorana spin flips* [19]. This can be thought of as a spin's inability to align to a quantized axis, which allows it to precess randomly. When the atoms move away from the field zero they will once again have a well defined axis, but if the spin has flipped when this occurs then they may be in an antitrapped state and can leave the trap. To remedy this loss mechanism, we shine a tightly-focused blue detuned 532 nm "plug" beam directly into the field zero location, repelling the atoms from the trap center and preventing Majorana losses. Traditionally this has been one of the least stable parts of the machine, as the area window the plug has to reside in is only tens of μm wide, and can shift depending on thermal fluctuations in the magnets or beam path. The laser creating the plug beam was traditionally a 10W Lighthouse Photonics Sprout, but has since been upgraded to a Coherent 18W Verdi for increased stability. The position of the plug beam is steered by a Newport 8821 Picomotor kinematic mirror mount on the second to last mirror before the main chamber.

A typical TOF run for RF evaporation from the magnetic trap is shown in Fig. 2.12. The temperature at the end of RF evaporation is usually 10 μK, with 30 million atoms remaining in the trap. Now there only remains one more step of evaporation required to

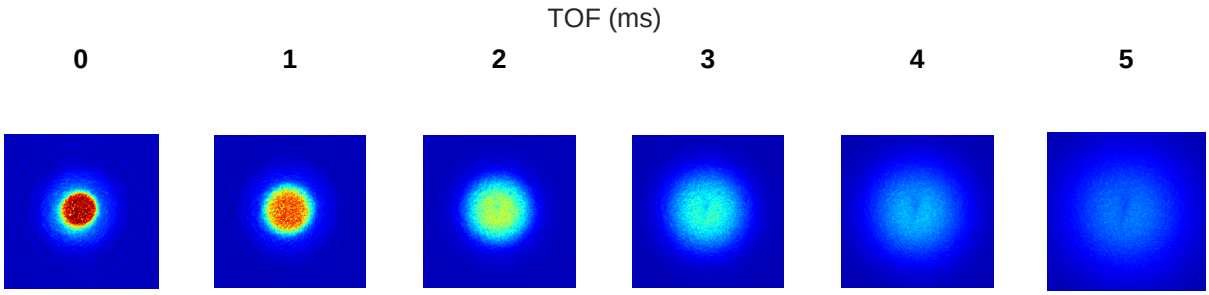

Fig. 2.12: Images of atomic cloud for increasing times of flight after RF evaporation. Each image is approximately 1 mm x 1 mm. The hole feature that appears in the center of the cloud for larger TOF values is created by the 532 nm plug beam, which turns off after the end of RF evaporation but leaves a residual effect on the atoms.

cool below the critical temperature, which I'll describe this in the next section.

2.2.4 Optical Dipole Traps and Optical Evaporation

Before performing the final evaporation stage, the atoms must be transferred to a different m_F level, due to the fact that the $|2,2\rangle$ state has a negative background scattering length of $a = -28\ a_0$. This leads to instability when creating BECs (though it is possible [20]), and it becomes necessary to put the atoms in a state where the interactions are positive. For ^{7}Li, a convenient state to use is the $|1,1\rangle$ state, which has a broad Feshbach resonance at 736.8 G and thus allows for easy tuning of the s-wave scattering length.

To accomplish this state transfer, we first load the atoms from the magnetic trap into an optical dipole trap (ODT), created by crossing two focused 1064 nm beams with $1/e^2$ radii of 80 μm. This light is generated from an Azurlight 130W fiber amplifier seeded by a Coherent Mephisto. The beams create a trap using the AC Stark shift, with the potential taking the form

$$U(\mathbf{r}) = \frac{3\pi c^2 \Gamma}{2\omega_0^3 \Delta} I(\mathbf{r}) \tag{2.3}$$

where Γ is the linewidth, Δ is the detuning, $\omega_0 = 2\pi c/\lambda$, and $I(\mathbf{r})$ is the intensity.

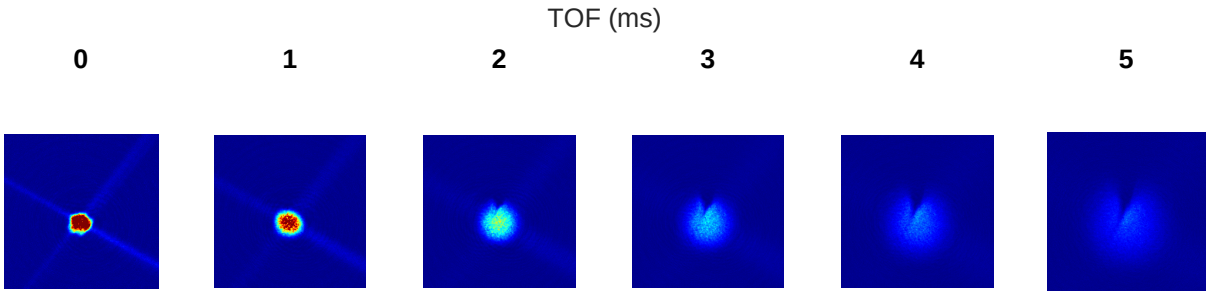

Fig. 2.13: Images of atomic cloud for increasing times of flight after transfer to the optical dipole trap. Each image is approximately 1 mm x 1 mm. The cut at the top of the images for TOF 2-5 ms is due to the residual 532 nm plug beam.

Each ODT beam has a maximum power of 20 W, which allows for a max trap depth U_{max} well above 50 μK. When transferring the atoms, we simultaneously ramp down the magnetic trap and ramp up the power of the ODT beams over 100 ms, typically capturing 1/4 of the atoms. Atomic images for a TOF experiment after the transfer to the ODT is shown in Fig. 2.13. To transfer them to the $|1,1\rangle$ state, we perform a rapid adiabatic passage by sweeping the RF frequency from 809.6 MHz to 807.5 MHz over 60 ms in the presence of a small DC magnetic field to split the different m_F levels. The coils used for the MOT stage are at this time switched from anti-Helmholtz to Helmholtz to prepare the field for the Feshbach resonance.

Typically a moderate positive scattering length is beneficial for the final evaporation stage in order to ensure the atoms rethermalize in a small amount of time while making sure two- and three-body losses are mitigated. We tune the magnetic field to 720 G, corresponding to a scattering length $\approx 240\ a_0$ via 5.4 before starting evaporation. Evaporation is achieved by smoothly lowering the power in the ODT beams over the course of 4.5s with an exponential form $e^{-t/\tau}$ with τ empirically set around 2s. The power is reduced from 20W to $<$ 2W, with 90-95% of the atoms leaving the trap. The final cloud typically contains 10^5 to $3 * 10^5$ atoms, though we have reached as high as 10^6 atoms by modulating the ODT AOM frequencies at 10-40 kHz, realizing a painting procedure

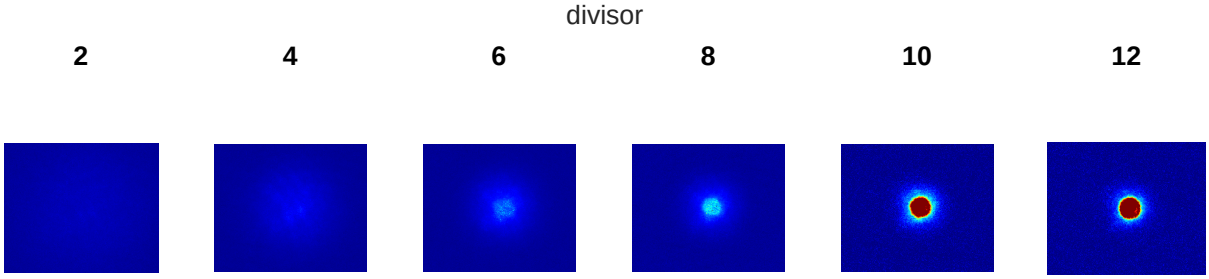

Fig. 2.14: Images of atomic cloud for increasing divisor after a 3 ms TOF. A clear condensed cloud is observed for divisors 10 and 12. The diameter of the BEC is ≈ 50 μm.

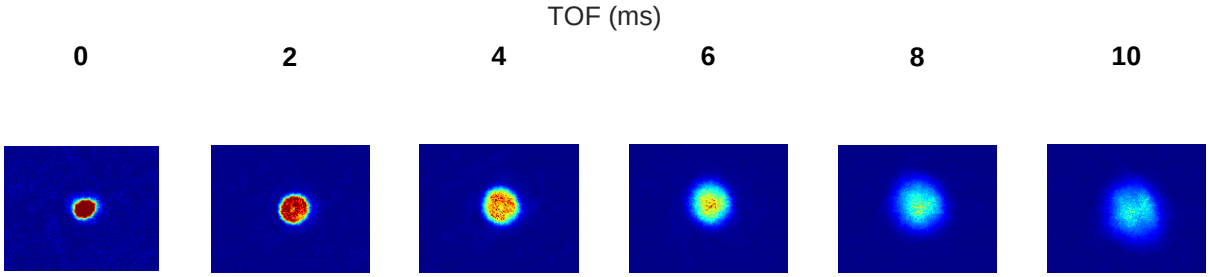

Fig. 2.15: Images of atomic cloud for increasing times of flight after the final optical evaporation stage. The atoms are now in the BEC stage. The diameter of the BEC is ≈ 50 μm.

which increases the effective trap volume. The temperature of the atoms at the end of optical evaporation is 10 nK, and we have successfully created a BEC!

Atomic images of the cloud after optical evaporation to different power levels (and a TOF) are shown in Fig. 2.14. The final power goes from high to low moving left to right, with the divisor number indicating $Power_{ODT,initial}/Power_{ODT,final}$. The evaporation time is held constant over all runs. It is evident that when the power is reduced only by a small amount, the cloud remains thermal and thus expands over a large region post-TOF. As the power is reduced more, a condensate starts to form, and in the right most image only the condensate remains with negligible atoms in the thermal fraction. Atomic images of the BEC during a TOF are shown in Fig. 2.15. Due to the extremely cold temperatures, very little motion or change is seen in the cloud until much higher expansion times. Note that the TOF times in previous stages only went from 2 to 5 ms.

2.3 Optical Lattices

After creating a BEC, many of our experiments involve applying an optical lattice to the atoms, the physics of which is explained in section 1.6. The light for the optical lattice is generated from the same Azurlight 130W fiber amplifier used for our ODTs. Typically, more power can be diverted to the lattices from the ODT path using a set of Pacific Laser Equipment RSC-103E waveplate rotators which control the power distribution between the dipole trap beams and the lattice beams. Since the lattices only turn on after the end of optical evaporation, this power transfer is warranted, as little to no power is used in the ODTs during lattice experiments.

The main features of the lattice path include: a) an AOM for fast switching of the lattice, b) the input lens to focus the lattice beam onto the atoms, c) a pickoff to allow for imaging of the lattice beam without damaging the camera, and d) the retro mirror, which is used to overlap the input and retro beams. One unique feature of our apparatus is the presence of a second coaxial lattice, which has its own AOM path and shares b), c), and d) with the first lattice. There are two $\lambda/4$ waveplates before the retro mirror to adjust the relative spatial phase of the lattices, which is discussed in the experiment section of Chapter 4 4.2. The procedure to align the lattice is slightly involved, which I've outlined below for students on the lithium machine.

Lattice alignment procedure :

1. Input alignment:

   (a) Take an image of the BEC from the lattice axis

   (b) Divert all power into whichever lattice beam is being aligned

   (c) Make sure the lattice AOM efficiency is good, and that the 0th order is appropriately dumped

(d) Center the lattice beam on input lens before the chamber

(e) Image the lattice beam on the lattice-axis camera and overlap to the BEC position using the picomotor. The lens and the camera will act as the two points of alignment. The input should be roughly aligned now.

2. Retro alignment:

(a) Find the retro beam using card + lens cloth. This part can be quite tricky, so use all tools at your disposal, including the military grade IR viewer.

(b) Once the retro beam has been found, slowly work backwards along the path while adjusting the retro knobs. The other lattice path can also be used here to identify the retro beam, as it mixes on the cube pre-chamber.

(c) Retro all the way back to the first isolator after the ALS output. Once there is retro power out of the rejection port, touch the retro knobs until the rejection power is maximized. The retro should be coarsely aligned now.

3. Fine tuning:

(a) Start taking KD runs. After creating the NI BEC, kick with the lattice for 1-3 us at maximum power. Make sure there is a nonzero TOF, otherwise the momentum orders won't resolve themselves.

(b) Hopefully at this point there should be multiple momentum orders present. Start turning the retro knobs in small evenly spaced increments, taking an image in between each turn. If alignment is improving, more orders will be present.

(c) If the atoms look bowed/curved along the lattice axis, that's usually an indication the input beam has to be aligned better, so touch that before making further retro turns.

(d) Maximize the number of orders seen during KD. At this point, the lattice should be well aligned.

2.4 Imaging

Imaging is the main method for taking data on the lithium machine. Taking pictures of the BEC, both in-situ and post-experiment, can yield information about position and momentum space distributions, as well as relevant quantities like energy and temperature. The following section will discuss the physics of absorption imaging as well as the experimental setup on the ^{7}Li apparatus to achieve it.

2.4.1 Absorption Imaging

Absorption imaging treats the atoms as a medium for light to propagate through. If the medium absorbs light, then the intensity I will attenuate according to **Beer′s law**:

$$dI = -\mu I dx, \tag{2.4}$$

which states that light is lost proportionally to its intensity and path length. Integrating the above equation through the whole medium (of length x, let's say), the expression for the intensity after the medium becomes

$$I = I_0 e^{-\mu x} = I_0 e^{-OD} \tag{2.5}$$

The term in the exponent is referred to as the optical density (OD), which is related

to the resonant cross section σ_0 via the relation

$$OD = n\sigma_0 \tag{2.6}$$

where n is the number density of the atoms. This is usually the relevant quantity of interest, as data analysis begins with reconstruction of the atomic distribution. When imaging, the beam of resonant light is shone on the atoms, and a picture of the atoms' shadow is captured on the camera. The resonant light is attenuated according to Eq. 2.5, and the resultant OD is used to reconstruct the spatial form of the atoms.

2.4.2 Experimental setup for imaging

The imaging light is prepared from a branch of the master laser path, and is tuned to resonance with the D2 line. Once fibered onto the machine table, the beam has a waist of 3 mm and is collimated. To image the atoms, the resonant beam must pass through the atoms, and the position of the atoms must be imaged by the camera. A 4f telescope is used to accomplish this, shown in Fig. 2.16. In this configuration, the atoms are at the focal plane of the first lens (the *objective* lens) of the telescope. This lens has a focal length f_1 of 200 mm, and is placed 200 mm after the atoms on the path. After the objective lens is a second lens (the *refocusing* lens) with a focal length f_2 of 500 mm and a distance $f_1 + f_2$ between the two lenses. Finally, the camera is placed a distance f_2 from the refocusing lens, completing the 4f setup. A resonant beam passing through this 4f telescope will image the atoms' shadow onto the camera, magnified by a factor f_2/f_1. The PCO camera has a pixel size of 6.5 μm x 6.5 μm, which after magnification becomes a resolution of 6.5 μm/(500/200) = 2.6 μm per dimension at the atoms.

In practice, one picture isn't a good metric for capturing the atomic distribution,

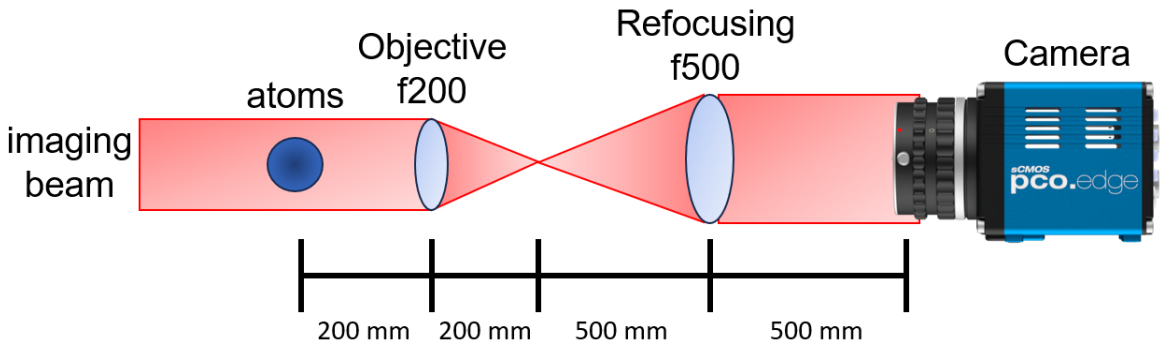

Fig. 2.16: 4f telescope system for atomic imaging.

as the image captured by the camera includes background light as well as parts of the imaging beam which are not seen by the atoms. To account for this, three images are taken in the following order: i) an resonant pulse which passes through the atoms (the *probe with atoms*, or PWA), ii) a resonant pulse a short time later, which images just the beam (*probe without atoms*, or PWOA), and iii) a dark image with no resonant pulse, which captures the background. The OD can then be computed as

$$OD = \ln\left(\frac{\text{PWA} - \text{Dark}}{\text{PWOA} - \text{Dark}}\right), \tag{2.7}$$

which gives a more accurate description of the atom count per pixel area. The resonant pulses are typically applied for 5μs to image the atoms while their motion is negligible.

2.4.3 Issues and Limitations

Absorption imaging is useful due to its ease of setup, usage, and output simplicity. However, there are a few drawbacks and pitfalls to be aware of when using this method.

These include saturation intensity, focusing, detuning, and fringes.

Saturation Intensity - When shining resonant light for imaging, it's possible to enter a regime where the attenuation becomes nonlinear through the atoms if the imaging beam has too large of an intensity. This can be characterized by the *saturation intensity*, which for ^{7}Li on resonance is defined as

$$I_{sat} = \frac{\pi hc}{3\lambda^3 \tau_s} = 2.54 \text{ mW/cm}^2, \tag{2.8}$$

where λ is the resonant wavelength 670.961 nm and τ_s is the excited state lifetime of 27.1 ns. Typically, the desired intensity of the imaging beam $I << I_{sat}$. To gauge this, the saturation parameter $s = I/I_{sat}$ can be calculated from experimental parameters. The simplest approach is to perform a dimensional analysis to get I, which has units of power/area.

The readout from the PCO gives total counts, N_c. Counts doesn't give much information as a unit, but can be converted by multiplying by the conversion factor c_f, the number of electrons per count, and dividing by the quantum efficiency (QE), the fraction of photons that get converted into electrons by the sCMOS. This yields an expression for the number of photons:

$$N_\gamma = \frac{N_c c_f}{\text{QE}}. \tag{2.9}$$

The power of the imaging beam during a resonant pulse can be defined as

$$P = E/t = E_\gamma N_\gamma / t = \frac{hc}{\lambda t} \frac{N_c c_f}{\text{QE}} \tag{2.10}$$

where $E_\gamma = hc/\lambda$ is expressed in terms of the imaging wavelength, and t is the pulse duration, typically 5 μs. The expression for power is now fully expressed in terms of experimental parameters. For the PCO, the QE is 60% and the conversion factor is 0.46 [21].

To compute the area, the number of pixels in the region of interest N_p must be converted to the area at the region of the atoms. This can be done by multiplying by both the pixel length l_p (6.5 μm) and dividing by the magnification m (2.5 for the current setup) along each dimension:

$$A = N_p(l_p/m)^2. \tag{2.11}$$

Finally, an expression for the intensity I is obtained by putting the above expressions together:

$$I = \frac{P}{A} = \frac{N_c c_f hc}{N_p(l_p/m)^2 \lambda t \mathrm{QE}}. \tag{2.12}$$

The saturation parameter s is then computed by dividing the above by I_{sat}. In practice we usually image with $s \sim .2$. If s is too high or too low, we adjust the imaging power using the VVA on the final imaging DP AOM and recompute s with the increased or decreased N_c.

Focusing - When imaging, the atoms should be at the focus of the objective lens in the 4f telescope. Unfortunately, moving the objective lens on the imaging setup is an ergonomic nightmare, so if the imaging system is misfocused typically adjustments are performed by moving the refocusing lens. To perform this alignment, it's most useful to

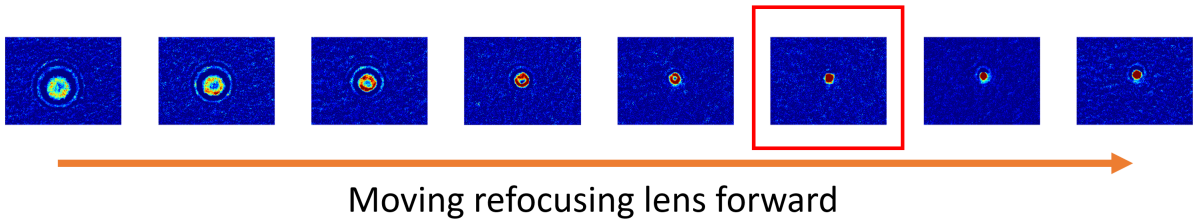

Fig. 2.17: Images of the BEC as the refocusing lens in the 4f system is moved forward. The lens is shifted ≈ 1 cm between every image. The optimal focus point is boxed in red, with minimal rings and aberrations compared to the other positions.

image the BEC at various lens positions while moving the lens over a span of many cm. The BEC size should be minimized at the correct focus position, and will typically look the sharpest while having few rings around the cloud. The presence of rings signals a defocused image (Fig. 2.17).

For some experiments, it's most useful to be focused at a specific TOF. Ideally this would be done by moving both the objective and the refocusing lens such that the atoms at that TOF (which are in a different position than atoms at 0 TOF) begin the 4f setup. Again, as we are unable to easily adjust the objective lens, typically just the refocusing lens is adjusted to maximize image quality at that specific TOF.

Detuning - The imaging beam needs to be resonant with the D2 line. However, this is complicated by the fact that the resonance shifts depending on the applied magnetic field, and the magnetic field changes for different interaction strengths due to the Feshbach resonance. To remedy this, we have 3 imaging paths (hopefully only 1 in the future using an offset lock scheme), one for imaging in the high-field (HF) regime close to the Feshbach resonance, one for the low-field (LF) regime close to 0 G for the cooling sequence before BEC, and one for the noninteracting (NI) regime close to $0a_0$. These 3 paths cover almost all interaction scenarios investigated during experiments. For the HF regime, if we change the magnetic field to access different interaction strengths, the final AOM frequency can be tuned to follow accordingly. This sweeping of the AOM frequency is a useful tool to

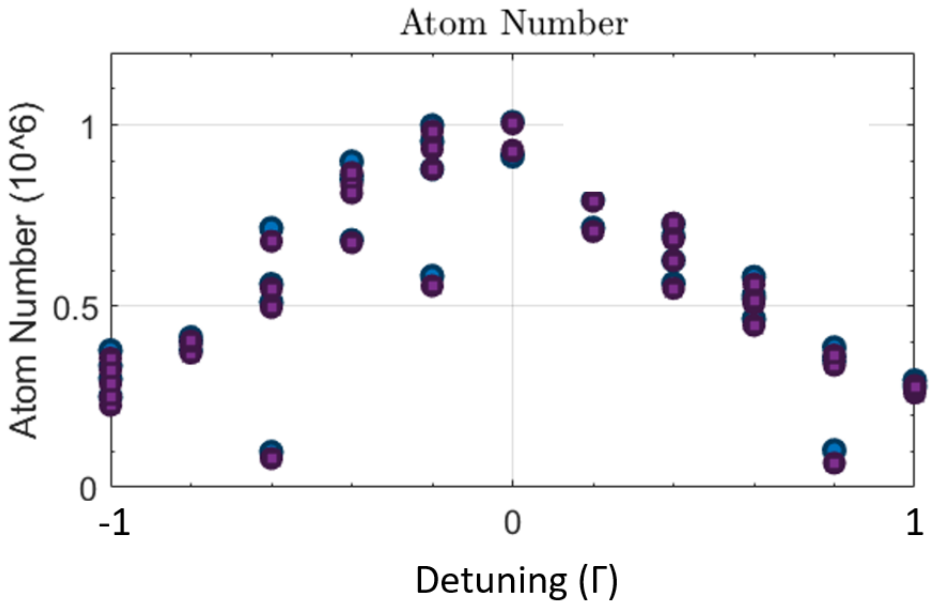

Fig. 2.18: BEC atom number as the image beam detuning is scanned. Here $\Gamma = 2\pi * 5.9$ MHz.

ensure proper detuning, and a typical signal in atom number can be observed (Fig. 2.18).

Fringes - Fringes are the bane of image data analysis. They manifest as periodic fluctuations in counts across an image, usually with many components at different frequencies. They are created by inadvertent interferometers, and vary due to outside light sources, vibrations (ie. people opening and closing doors, walking, loud music, etc.), and airflow. Many steps have been taken to mitigate the effects of these fringes, both pre- and post-analysis. All optics have been converted to 1" diameter pedestals from 1" length posts, and the mirrors have been upgraded from 1" to 2" diameter. This has helped stabilize the path from vibrations. In addition lens tubes and new machine enclosures have mitigated a large portion of the light pollution entering the imaging system. After images are taken, we use a fringe removal method [22] to remove remaining fringes after processing. All of these measures have helped, but fringes remain an issue that can always be improved upon.

2.5 Cicero control software

The experimental sequence requires precise timing and control of analog and digital outputs which interface with a host of electronic and opto-electronic components (ie. magnets, RF drivers, shutters, switches, etc.). To coordinate this matrix of outputs, we use a program called Cicero, initially developed at MIT in the lab of Wolfgang Ketterle [23]. Cicero communicates with a 10 MHz FPGA (Opal Kelly XEM3001), and allows for timebase control ranging from a few μs to minutes. Digital control is performed via 2 National Instruments PCIe-65353 10 MHz digital I/O cards in home-built boxes capable of outputting 32 channels each. Analog control is performed via 3 National Instruments PCI-6713 cards, which have 8 outputs each and can generate 12-bit signals ranging from -10 to 10V. This architecture allows for the control of the nearly 100 combined digital and analog channels required to successfully make and probe quantum dynamics with BECs. While the manual for Cicero provides adequate documentation for setup, there are many subtleties that I provide in this section which may be useful for future students.

2.5.1 Main GUI

Fig. 2.19 shows a typical GUI one encounters when using Cicero. Each column (known as a 'word') is a time sequence where individual analog and digital outputs can be modified and set. The colored red, black, and green sections show the waveforms of all analog channels and how they change per word. Similarly, the bottom orange, brown, blue, and green section describe the state of each digital channel per word, with light brown designating an off state and any other color designating an on state. The array of words creates a sequence, which represents the set of control directions required to generate our quantum gas up to any desired state, from the MOT to BECs in lattices and everything in between. Pre-loaded sequences can be set via the drop-down bar to the

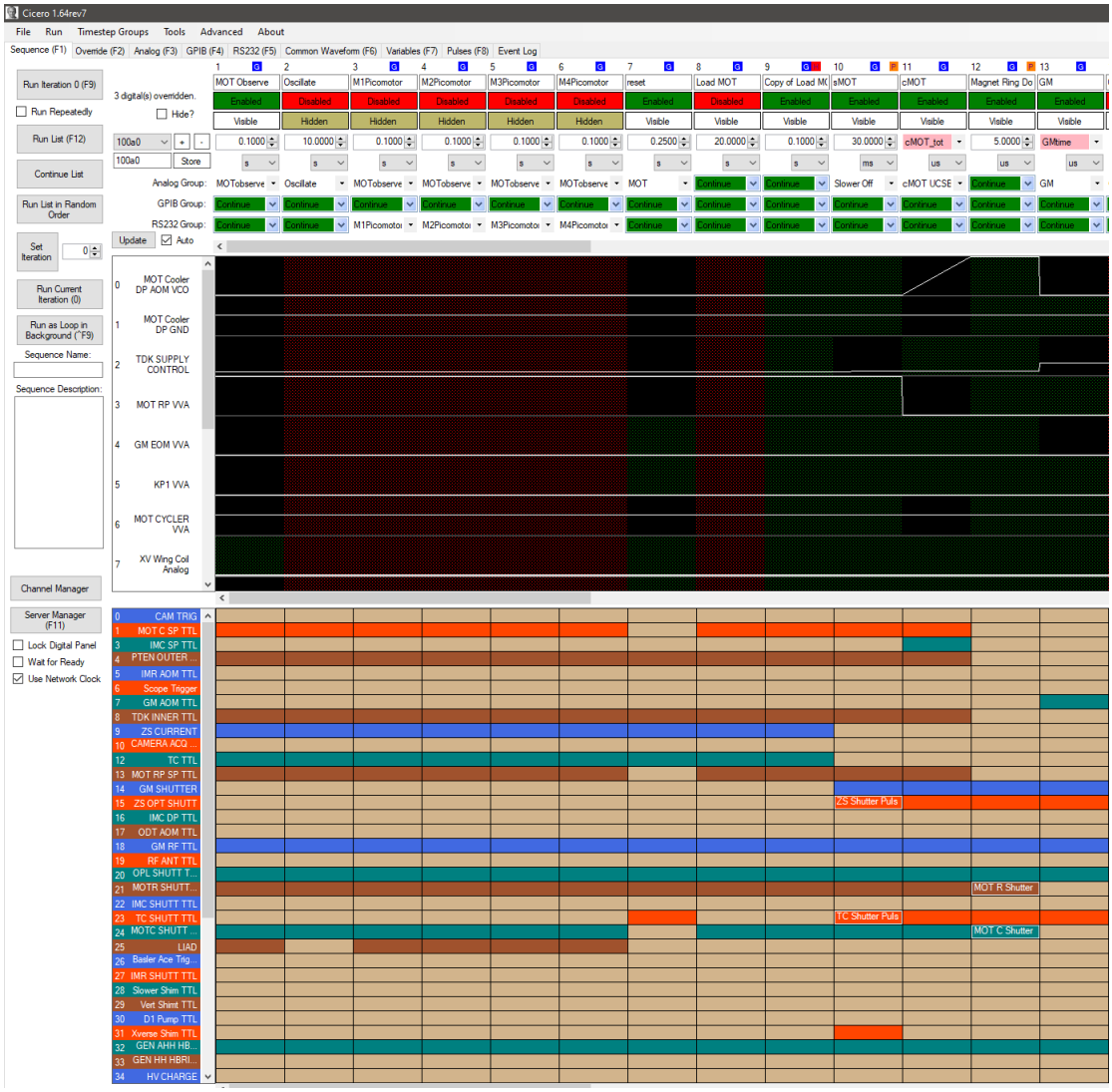

Fig. 2.19: Example Cicero GUI.

left of the first word (100a0 for this example). Sequences can be run using one of the run buttons in the left sidebar, with choices of running single iterations or entire lists (running lists with variables are discussed later in the section). WARNING: once a run button is pressed, the sequence cannot be stopped unless aborted. When aborting a sequence, the analog and digital outputs will typically stop in whichever word the sequence is aborted in. This can pose a real danger if certain magnets are on at high voltages/currents or lasers are at full power. It is prudent to be aware of this, and if aborting mid-sequence

it is good practice to go back to the first word (typically MOT Observe), right click and hit Output Now. This reverts the outputs to the state at the beginning of the sequence, which doesn't pose a danger.

2.5.2 Overrides

Overrides are used to manually set analog and digital outputs. In the GUI shown in Fig. 2.20, the left column has digital overrides that can be used to turn specific channels on and off. The right side shows analog overrides, where constant voltages can be set for specific outputs. These are most useful as testing and debugging tools. While obvious applications include testing the functionality of analog and digital outputs, it's worth noting that anything left overridden when running a sequence will not change during the sequence, even if there are directions to do so in certain words. This is the main aspect to be aware of, as there are often situations where running sequences will occur directly after debugging with overrides, and if overrides are left on the sequence output on the atoms will be undesirable.

Specific to the lithium machine, overrides are typically a way to assess specific laser paths. When attempting to turn on specific light (ie. any of the imaging beams), it is necessary to familiarize oneself with all AOMs and shutters upstream, as they will all have to be toggled in the overrides to generate the desired light. Luckily if this is ever unclear, one can check the word in the sequence where the desired light is generated and copy all of the necessary overrides from looking at the outputs set in that word. This can generally be applied to replicating anything that occurs in sequence that needs to be debugged ex-situ. Again certain safety precautions need to be taken, as overriding magnets with high currents can cause rapid heating and lead to eventual meltdown of the magnet wires.

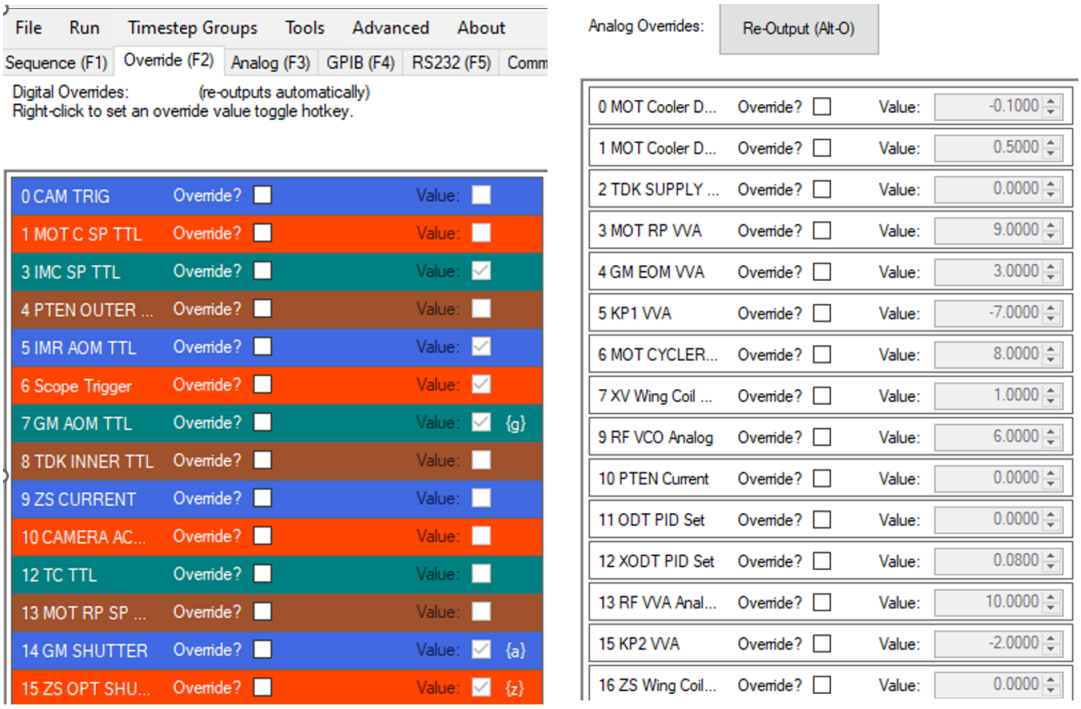

Fig. 2.20: Cicero overrides tab. The left image shows the override panel for digital channels while the right shows the overrides for analog channels. The analog channels can be set to specific desired voltages.

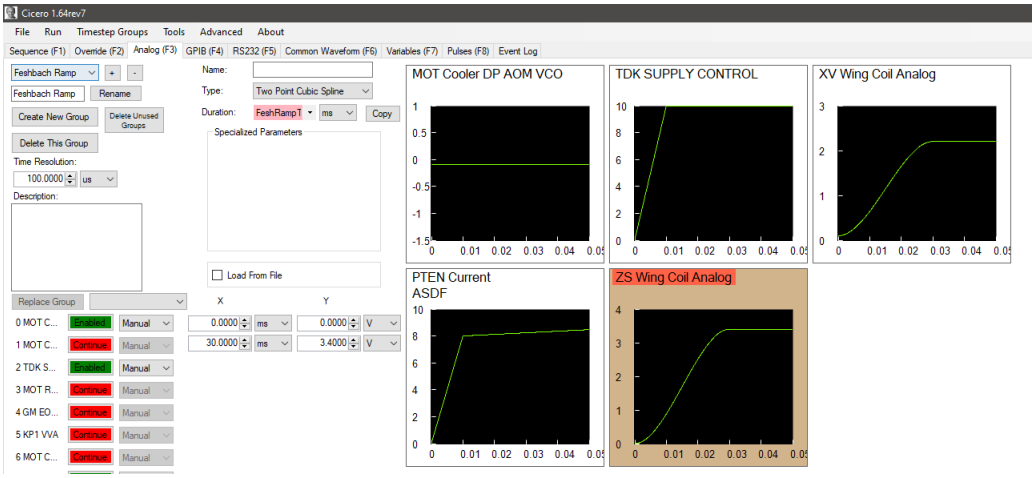

Fig. 2.21: Example analog word in Cicero. The waveform for each analog channel in the word can be set in the tab.

2.5.3 Analog Channels

While digital channels are simple to set due to their binary on-off nature, analog channels require specific user-set waveforms for the entire duration of each word, and thus more effort from the user. There are in-built Cicero functions to generate waveforms of specific types, such as piecewise linear, exponential, two point cubic spline, step, and sinusoidal. These can be selected from the "Type" dropdown menu. If a channel is unchanged during a word it can simply be continued from the previous, selected on the left sidebar.

There are two special cases where users can unleash Cicero's true power of arbitrary waveforms: equations and custom waveforms. The equation option allows the user to write a functional form in plain text using Cicero variables as inputs. The mathematical functions available to type can be found in the Variables tab under "Equation Help". The custom waveform option allows the user to upload a csv of time-voltage pairs, giving the user freedom down to the individual timestep. This functionality is extremely important when undergoing nonadiabatic ramp protocols requiring nonstandard functional forms, further discussed in 5.5.1.

2.5.4 Variables

Variables are the ultimate tool of the experimentalist, and all reside in the Variables tab shown in Fig. 2.22. Each variable is bound to a value, as well as one or multiple locations within a Cicero sequence. Variables give the user control over voltages and times in the sequence, and allow for easy tweaking when specific feedback is learned from runs. The list feature allows variables to be bound to a certain array of values, and running a whole list allows the user to understand how the atoms behave during a specific stage of the sequence as a variable is changed.

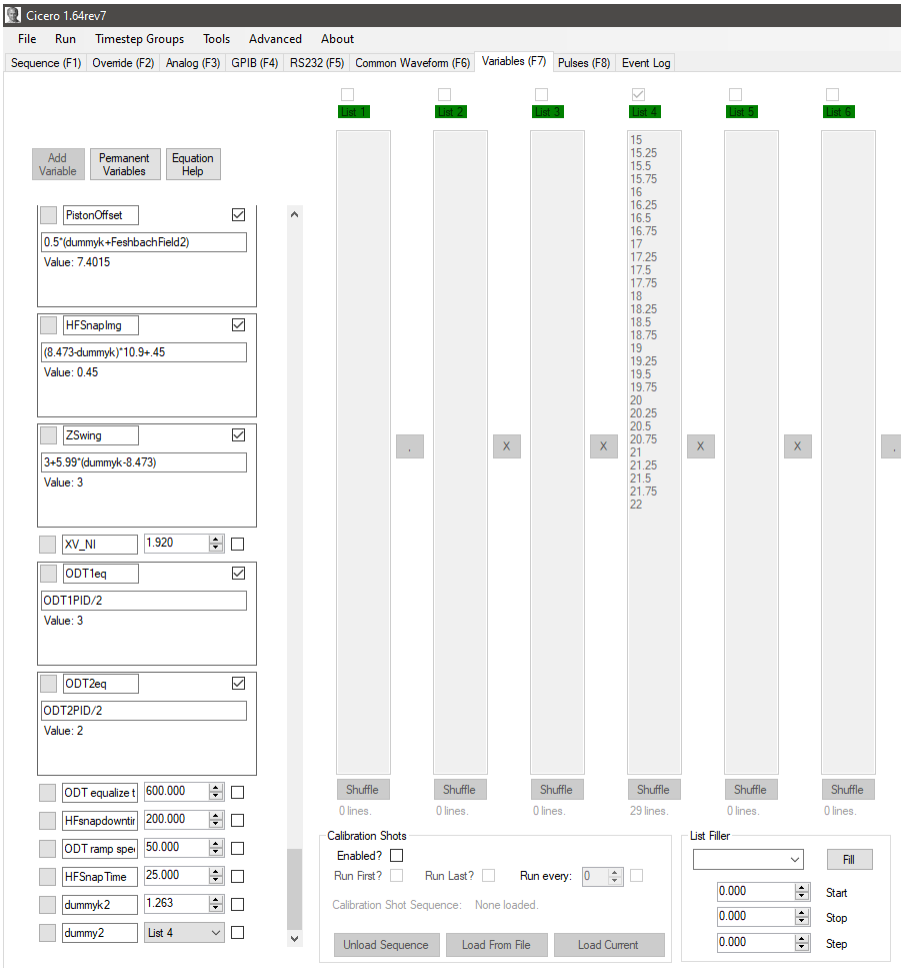

Fig. 2.22: Cicero variables tab.

2.5.5 Useful functions

Hold and retrigger - At certain points during the sequence, it becomes necessary to move on to the next step when a certain condition is met. To achieve this, a step can be held until it receives a specific trigger using the hold and retrigger function. The prominent example on the lithium machine is moving onto the GM cooling step after the MOT has reached a certain size. We use a comparator circuit that reads a voltage from the photodiode measuring the MOT fluorescence, and the circuit only triggers once the voltage is past a specific threshold, which tells Cicero to move to the next word. Recently,

there have been ideas to use this function to coordinate the running of the lithium and strontium machine in tandem, such that lithium's parasitic RF radiation does not affect strontium's laser locks or optical lattices.

Timestep groups - For many experiments, certain collections of words will have to be repeated over and over again , especially for experiments where Hamiltonian parameters have to be cyclically varied. To accomplish this, a *Timestep group* can be created using the "Timestep group" tab at the top of the GUI. The number of times the group will loop can be set in the same tab by selecting the desired group and clicking "Loop Timestep group". After creating a new group (or if a group already exists), words can be added to the group by right-clicking at the top of the word and selecting "Timestep group". Crucially, when running Cicero it's important to make sure there are no stray words in between words of a specific group, as Cicero will throw an error. All words within a group should contiguously follow one another.

"**Dummying" into a word** - Often times when debugging, it's useful to see what effect a change of variable has on the atoms, as described in 2.5.4. This can be accomplished in various ways, and it's important to understand the differences between each method. For the following scenarios, I'll use the FeshbachField variable set in the Feshbach Ramp word as an example, which controls the current in the magnets used to generate the magnetic field for the Feshbach resonance.

First, the variable itself can be bound to a list of different values. Running the list will take successive runs where the magnetic field and thus the interaction strength will be changed, but crucially the amount of *time* it takes to perform the ramp ($\approx$ 50 ms) will not change. Thus binding the variable in this way will change both the final value of the ramp as well as the ramp rate.

Second, the amount of time the word takes can be changed. This can be accomplished by binding the FeshRampT variable, which sets the word duration, to a list of different

values. This will change the amount of time the Feshbach Ramp word takes, but will not change the final values of FeshbachField. Thus, this list will change the ramp rate.

In both of the previous examples, variables are changed but the entirety of the Feshbach Ramp word is completed during the run. However, it's often useful to see what's happening *during* a word itself. This is where the lab lingo of *dummying* into a word comes from. Instead of binding FeshRampT to a list, a new variable, usually "dummy", is bound instead. Then, the word duration of Feshbach Ramp is changed to dummy. When making this change, FeshRampT is still bound as the end time of FeshbachField within the analog word itself. Thus, binding dummy in this way will actually create time slices of the original Feshbach Ramp word, and iterating through dummy values from 0 to FeshRampT constitutes reconstructing the entire "movie" of the word. Doing this maintains the same ramp rate, but changes both the FeshbachField value and the duration of the word in each run.

Iterating through multiple variables - In many experiments there is a need to iterate two variables at a time, perhaps to explore a phase space. Cicero allows the user to do this by binding multiple variables to different lists. Once bound, the lists can either be dotted or crossed, using the * or x symbols respectively between the lists. For two lists of values [a_1, a_2, a_3,...a_n] and [b_1, b_2, b_3,...b_n], the dot operation will iterate through the lists in the order $[a_1, b_1]$, $[a_2, b_2]$, $[a_3, b_3]$,...,$[a_n, b_n]$ akin to a typical dot product in linear algebra. The cross operation will iterate in the order $[a_1, b_1]$, $[a_1, b_2]$,...$[a_1, b_n]$, $[a_2, b_1]$,... for a list of length n. The dot operation will require the lists to be equivalent lengths n and will run for n iterations, whereas the cross operation on a list of length m and a second list of length n will run for m x n iterations.

Variable preview changes - When in the middle of a list run, if there is a need to suddenly change one of the variables, this can be accomplished by pressing the variable preview button on the active window. This will open a window with a list of all variables

and their associated values, which can be changed. If a value is changed, a red button will appear next to it, which will have to be pressed to lock in the change. If the button changes to green, the variable will successfully change on the next run of the machine and remain there permanently until changed again.

Buffers - The main way I have crashed Cicero during my 5 years of running the lithium machine is by attempting to run words for too short of a time (the FPGA's time resolution is limited to 3 μs, and any shorter results in timing errors on the National Instruments cards). However, sometimes the error can occur if the time resolution of the word is much shorter than the overall length of the word, which can overflow the buffer. If encountering a Cicero crash after setting a variable or a time to a few μs, it's always worth comparing that value to the duration of the word to make sure they are not many orders of magnitude off (ie. occasionally setting a resolution of 1 μs for a 1s word can lead to a crash).

Chapter 3

Interacting Quantum Kicked Rotor

The prior two chapters have covered all of the ingredients required to start exploring new physics with BECs, and I'll now begin discussion of the experiments relevant to this thesis. In this chapter I will overview the interacting quantum kicked rotor, and how our lithium BEC machine is used to probe localization and many-body physics in this quantum chaotic system.

3.1 Background and Theory

3.1.1 Kicked Rotor

The kicked rotor is a quintessential model studied in nonlinear dynamics/chaos theory that shows a transition from integrability to chaos. I'll first explain the classical system, and then detail how it changes in the quantum regime.

To start, imagine a bead confined to a ring that is periodically kicked along one axis, as shown in Fig. 3.1.1. This can also be thought of as a pendulum periodically kicked by gravity (if we had the power to turn gravity on and off). The Hamiltonian for this system consists of two terms:

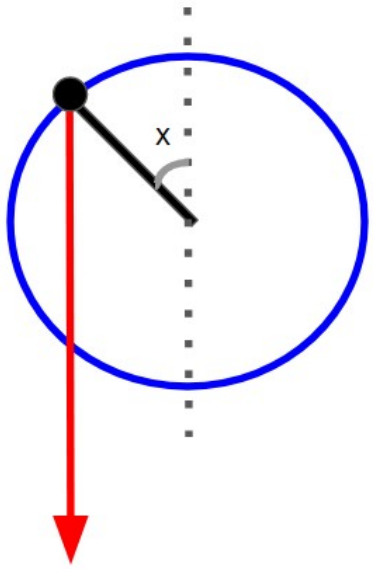

Figure 3.1: Protypical kicked rotor. A bead is confined to a ring and is periodically kicked along one axis.

$$\mathcal{H} = \frac{p^2}{2m} + K\cos\theta \sum \delta(\frac{t}{T} - n) \tag{3.1}$$

The first term is simply the kinetic energy, while the second is a periodic kick applied with strength K and period T, with δ being the Dirac delta function. The dynamics of this Hamiltonian are best illuminated by looking at the phase portrait stroboscopically. When sampling the dynamics once per period, the system is characterized by the Chirikov standard map [24,25], which shows how the momentum and angular position update every period:

$$p_{n+1} = p_n + K\sin\theta_n,\ \ \theta_{n+1} = \theta_n + p_{n+1}. \tag{3.2}$$

Here p is the momentum and θ the angular position, both modulo 2π for this analysis. The full behavior is described by the Kolmogorov-Arnold-Moser theorem [26], but the

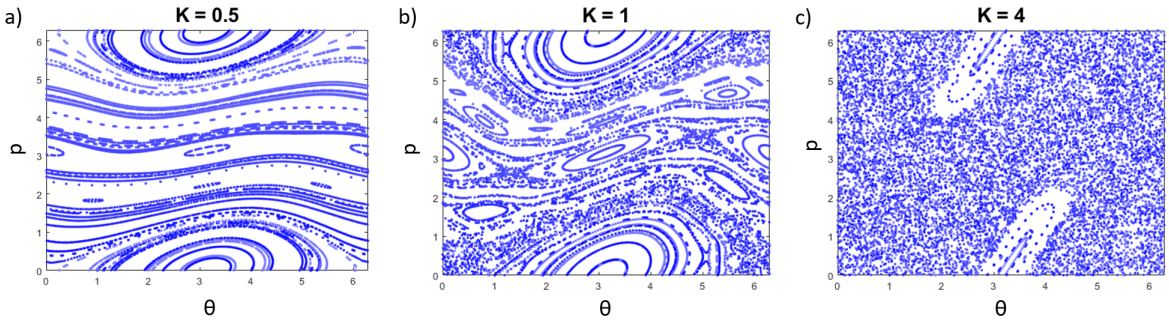

Fig. 3.2: Standard map for three different values of kick strength K, across the transition $K = .97$.

main feature is that the kicked rotor shows a transition from integrability to chaos as the kick strength K is varied. For low values (below $\sim .97$, the critical value), the phase portraits show coherent orbits, shown on the left in Fig. 3.2.

As K is increased, these orbits are destroyed, and beyond the critical value the kicked rotor exhibits a transition to chaos, whereby trajectories now explore the full phase space. This is shown on the right two plots of Fig. 3.2. One crucial feature in the chaotic regime is that the system is globally diffusive, meaning its energy increases linearly with time or kick number. This will be an important feature when comparing to the quantum version of the kicked rotor.

3.1.2 Quantum Kicked Rotor

What happens to this rotor in the quantum regime? The dynamics are now governed by the time-dependent Schrodinger equation:

$$(-\frac{\hbar^2\partial_x^2}{2m} + K\cos(x)\sum_n \delta(t - nT))\psi = E\psi \tag{3.3}$$

Intriguingly, the quantum kicked rotor (QKR) has a direct mapping to Anderson localization, outlined in [27–29].

We start with the Floquet operator of the QKR:

$$U(\alpha) = e^{-ip^2T/2\hbar}e^{-iV\cos(\mathrm{x})/\hbar} \tag{3.4}$$

where the first exponential represents the free evolution of duration T and the second exponential corresponds to the kick. A new operator M can be introduced such that

$$e^{-iV\cos(\mathrm{x})/\hbar} = \frac{1+iM}{1-iM}. \tag{3.5}$$

The eigenvalue equation for this system becomes

$$e^{-ip^2T/2\hbar}\frac{1+iM}{1-iM}\left|\phi_\alpha\right\rangle = e^{-iE_\alpha T/\hbar}\left|\phi_\alpha\right\rangle, \tag{3.6}$$

where $|\phi_\alpha\rangle$ is a Floquet eigenstate and E_α is a quasienergy. The eigenstates can now be expanded in the momentum basis:

$$\frac{1}{1-iM}\left|\phi_\alpha\right\rangle = \sum_m c_m \left|m\right\rangle \tag{3.7}$$

where $\hat{p}^2\left|m\right\rangle = \hbar^2m^2\left|m\right\rangle$. Eq. 3.6 can now be written as

$$e^{-ip^2T/2\hbar}(1+iM)\sum_m c_m\left|m\right\rangle = e^{-iE_\alpha T/\hbar}(1-iM)\sum_m c_m\left|m\right\rangle. \tag{3.8}$$

Both sides can be multiplied by $e^{\frac{ip^2T/2}{2\hbar}}e^{iE_\alpha/2\hbar}$ to yield

$$e^{-i(p^2/2-E_\alpha)T/2\hbar}(1+iM)\sum_m c_m\left|m\right\rangle = e^{i(p^2/2-E_\alpha)T/2\hbar}(1-iM)\sum_m c_m\left|m\right\rangle. \tag{3.9}$$

Finally, by projecting each side with $\sum_n |n\rangle \langle n|$ and rearranging terms, we obtain

$$\epsilon_n c_n + \sum_{m \neq n} \langle n| M |m\rangle c_m = -M_0 c_n \tag{3.10}$$

where $M_0 = \langle 0| M |0\rangle$ and $\epsilon_n = \tan(\frac{-\hbar^2 n^2/2 - E_\alpha}{2\hbar})$. Eq. 3.10 is the TDSE for a 1D Anderson model with site energy ϵ_n, tunneling amplitude $\langle n| M |m\rangle$, and total energy $-M_0$. There are two caveats to this mapping: i) the on-site energies are pseudorandom as opposed to purely random, and ii) the hopping amplitudes $\langle n| M |m\rangle$ couple to more than the nearest neighbor, but fall off exponentially. Nonetheless, this mapping is sufficient for the QKR to display Anderson localization-type behavior. This localization manifests in momentum space, and is dubbed *dynamical localization*. This strictly contrasts to the classical kicked rotor, where energy grows diffusively with time and experiences no localization.

Since localization in position space manifests as a suppression of diffusion, it's natural to expect localization in momentum space to manifest as a suppression of energy growth, which can be tested experimentally. An early experiment performed by Mark Raizen's group at UT Austin [30] repeatedly kicked a cold cloud of sodium atoms with an optical lattice, and demonstrated a saturation in energy even as more kicks were applied. This paved the way for QKR AMO experiments to explore further localization phenomena, including the observation of 2D Anderson localization as well as the 3D metal to insulator transition [31–33].

The interplay of localization and interactions is a deep and historic topic arising in a variety of condensed matter systems. The simplest implementation of interactions to the Hamiltonian is the addition a mean-field term, creating the Gross-Pitaevskii equation [7]:

$$(-\frac{\hbar^2\partial_x^2}{2m} + K\cos(x)\sum_n \delta(t-nT) + g|\psi|^2)\psi = E\psi, \tag{3.11}$$

written here for the QKR in 1D. The coupling constant $g = 4\pi\hbar^2 a_s/m$ represents the mean field interaction, and is proportional to the s-wave scattering length.

The introduction of interactions starts to probe the concept of *many-body localization* (MBL), which theorizes that localized systems can be stable even in the presence of interactions [34, 35]. Experimental explorations have not yet yielded definitive evidence of MBL (or MBDL, many-body *dynamical* localization), but have yielded intriguing observations of long-lived prethermal states [36, 37] as well as anomalous diffusion [38]. The interacting QKR is a natural venue to ask the question of MBDL existence, but surprisingly this has only been explored theoretically. Ref. [39] models the interacting QKR via the Gross-Pitaevskii equation (GPE) in 1 dimension, treating interactions in the mean field picture. In this model energy grows subdiffusively, with the growth exponent varying between 0.4 and 0.6 depending on both the kick and interaction strengths. This work implies the breakdown of dynamical localization in the presence of interactions for this model, but acknowledges that further work is needed to find any universal exponent. In addition, the applicability of mean-field theory is questionable and requires further theoretical and experimental understanding.

3.1.3 Many-body time reversal

Dynamical delocalization induced by interactions suggests a transition into the regime of many-body chaos. The strength of this transition can be probed using the concept of *time reversal*. When the QKR is kicked at the Talbot resonance, the time it takes for all modes to accumulate an integer multiple of 2π phase, the phase evolution from the free propagation becomes the identity for modes of type $|2n\hbar k_L\rangle$,

$$e^{-i\frac{\hat{p}^2}{2m\hbar}T}, T = T_{\text{Talbot}} = 9.93\mu s, \tag{3.12}$$
$$e^{-i\frac{\hat{p}^2}{2m\hbar}T_{\text{Talbot}}} = e^{i2\pi n^2} = 1.$$

For this resonance condition, only the kicks affect wavefunction evolution. This provides an interesting opportunity where if the kicking phase is reversed, it should be possible to "undo" the effects of prior kicks. This can be achieved by setting the free evolution after m kicks to half of the Talbot period, and then kicking another m times. Let's examine this for $m = 1$. The wavefunction after this protocol will be

$$|\Psi_f\rangle = e^{-iV\cos(2k_Lx)/\hbar}e^{\frac{-ip^2T_{\text{Talbot}}/2}{2m\hbar}}e^{-iV\cos(2k_Lx)/\hbar}|\Psi_i\rangle \tag{3.13}$$

Let's assume $|\Psi_i\rangle$ is the zero momentum plane-wave state. Following 1.18,

$$|\Psi_f\rangle = e^{-iV\cos(2k_Lx)/\hbar}e^{\frac{-ip^2T_{\text{Talbot}}/2}{2m\hbar}}\sum_{n=-\infty}^{\infty}(-i)^nJ_n(\frac{V}{\hbar})|n\rangle\,. \tag{3.14}$$

The free evolution propagator can be simplified,

$$e^{\frac{-ip^2T_{\text{Talbot}}/2}{2m\hbar}} = e^{-i\pi n^2} = (-1)^{n^2} = (-1)^n, \tag{3.15}$$

and Eq. 3.14 becomes

$$|\Psi_f\rangle = e^{-iV\cos(2k_Lx)/\hbar}\sum_{n=-\infty}^{\infty}i^nJ_n(\frac{V}{\hbar})|n\rangle\,. \tag{3.16}$$

Conveniently, the summation can be transformed by undoing the Jacobi-Anger ex-

pansion, recovering the initial state:

$$|\Psi_f\rangle = e^{-iV\cos(2k_L x)/\hbar} e^{iV\cos(2k_L x)/\hbar} |\Psi_i\rangle = |\Psi_i\rangle \,. \tag{3.17}$$

Thus, the sequence realizes a time-reversal protocol. The reversal still holds for multiple kicks, since in the resonant case each extra kick can be viewed as a rescaling of the kick strength. This so called Loschmidt time-reversal was theorized as a cooling mechanism for atomic matter waves [40], and then later experimentally proven [41] in 2011. The metric used to measure the efficacy of the reversal is the return fidelity,

$$F = |\langle\psi| U_2^\dagger U_1 |\psi\rangle|^2 \tag{3.18}$$

where U_1 and U_2 are time-evolution operators differing by some perturbation. For the experiment, the BEC has a finite quasimomentum width as well as interactions, which both limit F. For the latter, a question of how the many-body quantum chaotic regime affects F is intriguing, as chaotic systems imply extreme sensitivity to initial conditions and inherently implies a degree of irreversibility. This is what this part of the experiment will probe, discussed at the end of the next section.

3.2 Experimental Procedure

Our experiment begins with the creation of a ^{7}Li BEC, as outlined in Chapter 2, of around 10^5 atoms with a scattering length of $240a_0$ in an ODT. After the final optical evaporation step, we tune the s-wave scattering length of the atoms via the ^{7}Li Feshbach resonance. The ODT is then snapped off and the BEC is subjected to a pulse train of optical lattice kicks, which creates the QKR. A significant amount of effort is devoted to

proper alignment of the optical lattice, described in 2.3.

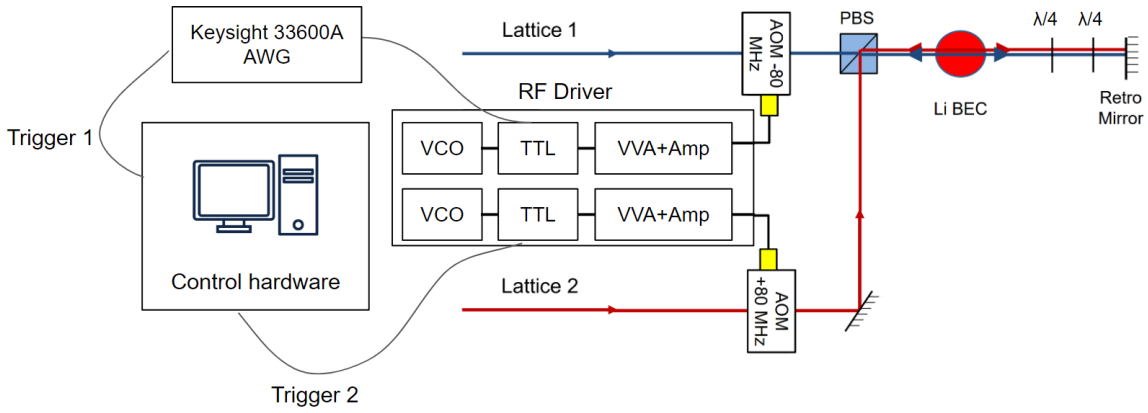

Fig. 3.3: Electronic and optical setup for the optical lattices. A driver box comprising of 2x voltage-controlled oscillators (VCO), TTL switches, and VVA+amplifiers creates an 80 MHz RF source with appropriate amplitude to drive each AOM controlling one of the optical lattice paths. For the lattice used in the QKR experiments (Lattice 1), the TTL is controlled by a Keysight AWG generating a pulse train. The retroreflection of the incoming laser beam by the retro mirror creates a standing wave optical lattice potential experienced by the atoms in the Li BEC.

The optical lattice was driven by a home-built RF driver box controlling the amplitude and timing of the lattice acousto-optic modulator (AOM) output (see Fig. 3.3). The AOM driving frequency (80 MHz) was generated by a Minicircuits VCO whose output is connected to a TTL switch (ZASWA-2-50DR+). This TTL is turned on and off via an external Keysight 33600A arbitrary waveform generator (AWG), which applies the pulse train for the experiment. Kicking waveforms are generated in MATLAB and can be uploaded to the AWG via ethernet or USB. The output of the TTL goes through a VVA followed by an amplifier which delivers 2W of RF to the AOM. The electronics inside the driver box are duplicated for the driving of our second coaxial lattice, which will be used for the next experiment described in the thesis. The light for the lattice is generated by a 130W 1064 nm Azurlight fiber laser, seeded by a Coherent Mephisto 1064 nm seed laser.

The three crucial features of the kicking lattice are its amplitude, pulse width, and timing. The amplitude controls the kick strength K in the Hamiltonian, and this is set via application of a voltage to the VVA. The timing between kicks, T, is fully controlled by the Keysight pulse train, with negligible timing noise from the TTL switch. The delay between pulses can be chosen arbitrarily, but there are a few experimental considerations which narrowed down the possible range of Ts. Initially many experiments were performed around $T = 10$ μs, close to the Talbot time ($T_{\text{Talbot}} = \pi\hbar/2E_{\text{R}} \approx 9.93\mu$s.) While this T easily populates many orders due to its proximity to resonance, after even tens of kicks atom counting for larger modes starts to fall below the noise floor of the camera, and with further kicks, start to leave the field of view of the camera. In addition to staying away from resonance, the atoms must be subjected to large numbers of kicks ($\sim$ 1000) to accurately observe the delocalization behavior reported. If T is set too large, the atoms undergo a significant amount of free expansion and fall out of the beam waist of the lattice. For a lattice beam waist of 100μm, the atoms fall out in 4.5 ms, thus requiring that nxT be significantly smaller than that timescale. On shorter timescales, the validity of the QKR mapping to our system becomes less clear due to the finite pulse widths of our kicks. Our AOMs have rise and falls times of 150 ns, and we experimentally find that $\tau < 300\mu s$ leads to instability in the lattice amplitude. Since $T >> \tau$, this sets a lower bound for the period. For the experiments shown in the paper, a value of 1.2us was used, compromising between the two regimes and allowing all experiments to be completed in $\sim$ 1 ms. After the kicks, the BEC undergoes a 3.5 ms free expansion to resolve the momentum modes populated by the experiment. The atoms are imaged via absorption imaging, and the energy is extracted after processing.

3.3 Data Analysis

The following is taken from the Methods section in [42], describing how the images are processed and data is extracted. Because the momentum distributions of the interacting samples change significantly over the course of the delocalization experiments, the quantities shown in Fig. 3.11 are computed directly from raw or averaged images as opposed to fitting procedures. However, this can make measurable quantities such as energy sensitive to noise, especially near the edge of the camera sensor due to the quadratic weighting. To maximize the signal-to-noise ratio in our measurement, we analyze raw images using an adaptive region-of-interest (ROI). First, a single base ROI capturing all detectable atoms at all times is created for each interaction strength. The integrated density in this ROI is used to post-select images with total atom numbers falling within a $\pm 10\%$ window of the mean, in order to reduce variations in the interaction energy, which depends directly on atom density. For these data we take 10 images at each kick number, of which typically 4-7 are discarded by this post-selection procedure. The ROI boundaries at each kick number are then determined by the points at which the cumulative summed distributions of the averaged image outward from a center point reach a threshold value. The thresholds are set empirically and the boundaries obtained by the following procedure. First we compute the transverse bound by integrating out the entire axial direction to get the overall transverse distribution, find the point it crosses an 85% threshold and then expand the resulting boundary by a factor of 1.5 to ensure all atoms are captured. We then compute an axial boundary going point by point along the transverse direction; at each transverse point we integrate over 10 neighboring transverse pixel rows to get a "local" axial distribution, find the point it crosses a 99.8% threshold and expand by a factor 1.15. Finally we smooth each ROI boundary and take a moving average across different kick numbers (4 on each side). Crucially, we have confirmed that

the qualitative observation of delocalization is not significantly altered from the simple case where we use just the initial single base ROI across all shots. However, the details of the trends should be more accurately captured by the adaptive procedure because the signal-to-noise ratio over the ROI is optimized at each kick number. All measurable quantities are then calculated from the imaged densities within this region.

Since we do not observe any substantial atom loss during the kicking duration, we treat the imaged atomic densities as normalized distributions. For Figs. 3.11a-b, we compute the measured quantities from individual experimental runs and then average the results, with the reported error bar as the standard error of the mean. A smoothing filter is applied to the displayed densities in Figs. 3.12c-h for visual clarity.

To measure the energy, we compute the post-expansion spatial variance of the distribution in both the kicking z and transverse x directions of the image. Assuming cylindrical symmetry, the kinetic energy is then calculated as $m\left(\langle z^2\rangle + 2\langle x^2\rangle\right)/2t_{\mathrm{TOF}}^2$ with $t_{\mathrm{TOF}} \approx 3.5$ ms (see section 2.4 for a discussion of possible corrections to the conversion of position to energy). For an accurate measurement of the interacting samples, inclusion of the transverse energy is necessary to account for energy-conserving scattering processes that occur both during the kicking and TOF. In addition, the inhomogeneous intensity profile of the beam $I(x, y)$ leads to a transverse energy oscillation in all samples including the noninteracting ones (see supplementary info in [42]). Since we are not interested in this effect, we remove it to leading order by subtracting off the noninteracting transverse energy from each trace, so that the noninteracting energy is purely the kinetic energy along the kicking direction. To compute the error bars on the interacting data, we add the error of the total interacting energy and noninteracting transverse energy in quadrature. The single-particle localization energy E_{loc} is estimated by averaging the noninteracting trace for $n \geq 100$, and the reported uncertainty is based on the standard deviation of those points. We note that this uncertainty is not only due to experimental

imperfections, but also due to natural dynamical fluctuations.

3.4 Characterizations

Before discussing the main results of this work, I'll highlight some of the intermediate work required to successfully complete this experiment. This section will summarize some of the nitty gritty, elbow-greasy efforts to accurately understand the interacting nature of our atoms, as well as the quantum phase evolution of the atoms during the initial portion of the QKR protocol.

3.4.1 Scattering length verification

The s-wave scattering length of the atoms is directly controlled by their proximity to the Feshbach resonance. Typically, to know this value we measure the current in the magnet coils via a fluxgate sensor and use that value as a proxy for the magnetic field. However, since the scattering length is critical to the analysis of the QKR, a second method was used to verify the value using a procedure analagous to [43].

To measure the scattering length, we perform an experiment equivalent to a 1-kick QKR experiment on a BEC with nonzero interactions, populating only the $0\hbar k_L$and $\pm$ $2\hbar k_L$ modes. After the kick, as the atoms undergo a time of flight, pairwise scattering events occur between each of the momentum orders. Let's consider just the $0\hbar k_L$ and $2\hbar k_L$ collision mode. In the frame moving at $1\hbar k_L$, this scattering event (now a collision between $-\hbar k_L$ and $\hbar k_L$ modes) creates a halo of atoms moving isotropically away from the origin, with each output pair having equal and opposite momentum of $\hbar k_L$ in an arbitrary direction. When taking images after a TOF, this manifests as a halo around the location of where an $\hbar k_L$ mode would lie, midway between the $0\hbar k_L$ and $2\hbar k_L$ mode. Those two modes lie on the edge of the halo. This halo phenomenon occurs for every

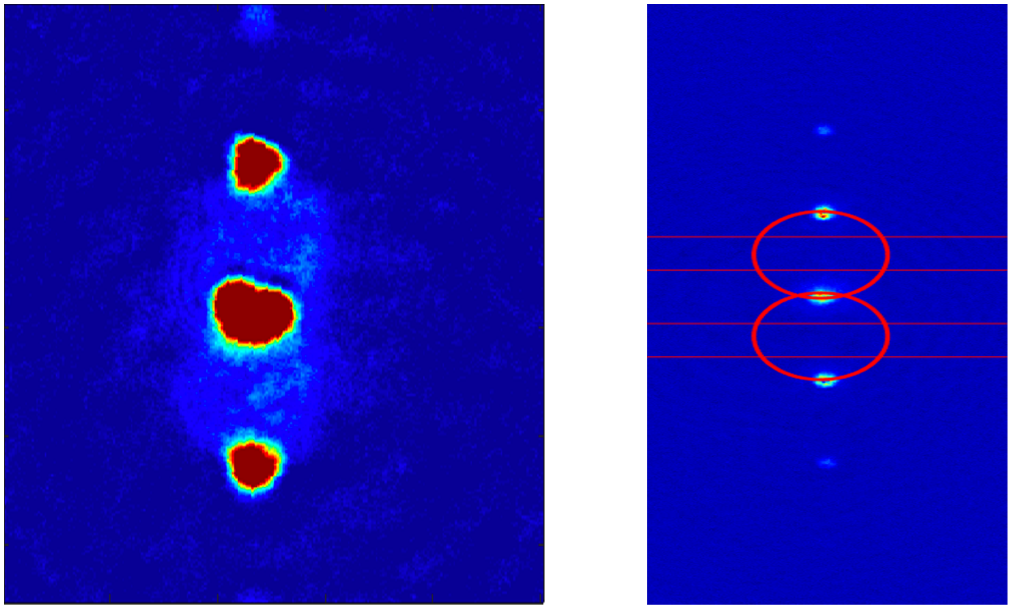

(a) Example scattering halos for $760a_0$ (b) Analysis region of halo

Figure 3.4: Scattering halos after a 1-kick experiment

pair of momentum modes, with the radius of each halo post-TOF equalling half the difference between the momenta. Examples of such halos can be seen in Fig. 3.4a. After taking images, we count atoms within a slice of each halo, shown as the intersection between the circles and horizontal lines in Fig. 3.4b. The selected region is chosen to minimize counting of non-scattered atoms in the modes, typically performed by looking at one-dimensional integrated densities along the transverse direction and determining the region that has negligible atom population from the unscattered discrete modes. Once the scattered atoms have been counted in the intermediate region of the halo, a value for the total number of scattered atoms in the halo can be determined by multiplying by the ratio of the halo volume to the counted volume. Once the number of scattered atoms have been counted, the interaction strength can be determined following the analysis performed in [43]. Within error, this method yields the same value for the scattering length as Eq. 1.12. This concludes an independent check on the scattering length which

can be used as a comparison to more conventional methods used for Feshbach resonances, such as those outlined in [9, 10].

3.4.2 Small kick number characterization

While a QKR experiment involves investigating behaviors after hundreds or thousands of kicks, it is first important to understand what happens to the atoms after just a few kicks. We have already explored Kapitza-Dirac diffraction in previous sections, but I'll use this section to specifically talk about the atomic phase after small numbers of kicks.

A natural starting point is to ask how do the atoms respond when the pulse time is varied for one kick. To explore this, I'll follow the analysis from [44]. First, let's revisit the fact that a BEC in an optical lattice gives rise to a band structure where the eigenstates are Bloch states. I'll write these states as $|n, q\rangle$, where n denotes the band index and q is the quasimomentum. The Bloch states can be expanded in the momentum basis with periodicity $2\hbar k$:

$$|n, q\rangle = \sum_{m=-\infty}^{\infty} a_{n,q}(m) \, |\phi_{q+2m\hbar k}\rangle \, , \tag{3.19}$$

where $|\phi_{q+2m\hbar k}\rangle$ is a plane-wave with momentum $q + 2m\hbar k$. Pre-kick, we can treat the BEC as a plane-wave $|\Psi(t = 0)\rangle = |\phi_q\rangle$. When suddenly subjected to the lattice, the state is projected onto the Bloch state basis:

$$|\Psi(t = 0)\rangle = \sum_{n=0}^{\infty} |n, q\rangle \, \langle n, q|\phi_q\rangle \, . \tag{3.20}$$

From 3.19 we know $\langle n, q|\phi_q\rangle = a^*_{n,q}(0)$. Thus, the BEC wavefunction evolves according to

$$|\Psi(t)\rangle = \sum_{n=0}^{\infty} a^*_{n,q}(0) e^{-iE_n(q)t/\hbar} \, |n, q\rangle \, , \tag{3.21}$$

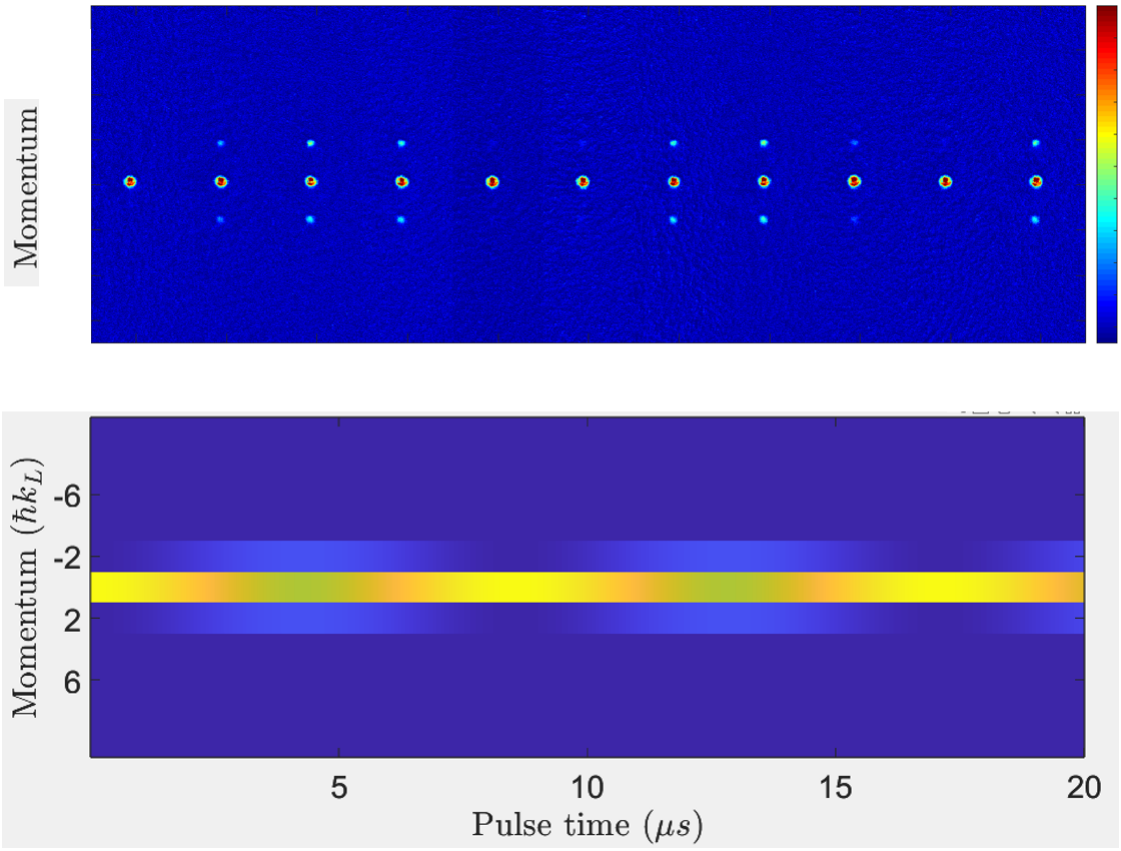

Fig. 3.5: 1-kick momentum state oscillations as the pulse time is varied for a $3.5E_R$ lattice. The top panel shows experimental data after a 2ms TOF. The bottom panel shows results of a TDSE simulation for the same parameters. The bandgap between the 0th and 2nd bands is 117 kHz, reflected in the observed oscillation period of 8.5 μs. The x-axes are the same for both panels.

where $E_n(q)$ is the eigenenergy of band n at quasimomentum q. We typically end our experiments by snapping off the lattice to allow the atoms to undergo a TOF, and this action projects the wavefunction back into the plane-wave basis. The coefficients $b_q(m)$ for each plane-wave $|\phi_{q+2m\hbar k}\rangle$ become

$$b_q(m) = \sum_{n=0}^{\infty} a^*_{n,q}(0) a_{n,q}(m) e^{-iE_n(q)t/\hbar}. \tag{3.22}$$

With this form for $b_q(m)$, there arises interference between the factors in the exponent, which physically manifests as an oscillation in the momentum state occupation. An

example of this is shown in the top panel of Fig. 3.5. The oscillation frequency is the band gap frequency between the bands of the two populated modes, which in this case are the 0th and 2nd band for a $3.5E_R$ deep lattice. The measurement of this frequency can be a useful tool to calibrate the lattice depth. Simulations using TDSE are shown in the bottom panel, showing excellent agreement with experimental data and verifying the oscillation frequency.

From the above, along with the prior analysis of Kapitza-Dirac diffraction, we know that for one kick the pulse amplitude and width dictate which momentum modes become populated, what their relative populations are, and how they interfere and accumulate phase. Now let's move on to two kicks.

For two identical kicks, the new degree of freedom is the free evolution time of the atoms between the kicks. Since the only populated states are integer multiples of $2\hbar k_L$, the relevant timescale with which the states accumulate phase will be the Talbot time, derived in section 3.1.3. We can probe this phase evolution with an experiment analogous to a Ramsey interferometer. In a typical Ramsey sequence, two $\frac{\pi}{2}$ pulses are applied to a two-level system with a variable wait time in between, with the output phase varying according to the evolution between the pulses. We similarly use this technique and observe oscillations in atomic population at the Talbot time, and observe coherence for many periods (see top panel of Fig. 3.6) . This can be modeled with TDSE similarly to the one kick experiment, and oscillations with a period of the Talbot time are readily observed in the bottom panel of 3.6. The feature in the middle of the oscillations can be attributed to the fact that 3 momentum states are occupied as opposed to two, but the times sampled in the experiment don't resolve this feature. The decay in amplitude of the oscillation is due to nonzero interactions for this experimental set (the s-wave scattering length is 240 a_0). This decay can potentially be used as a mechanism for determining the onset of decoherence due to interactions.

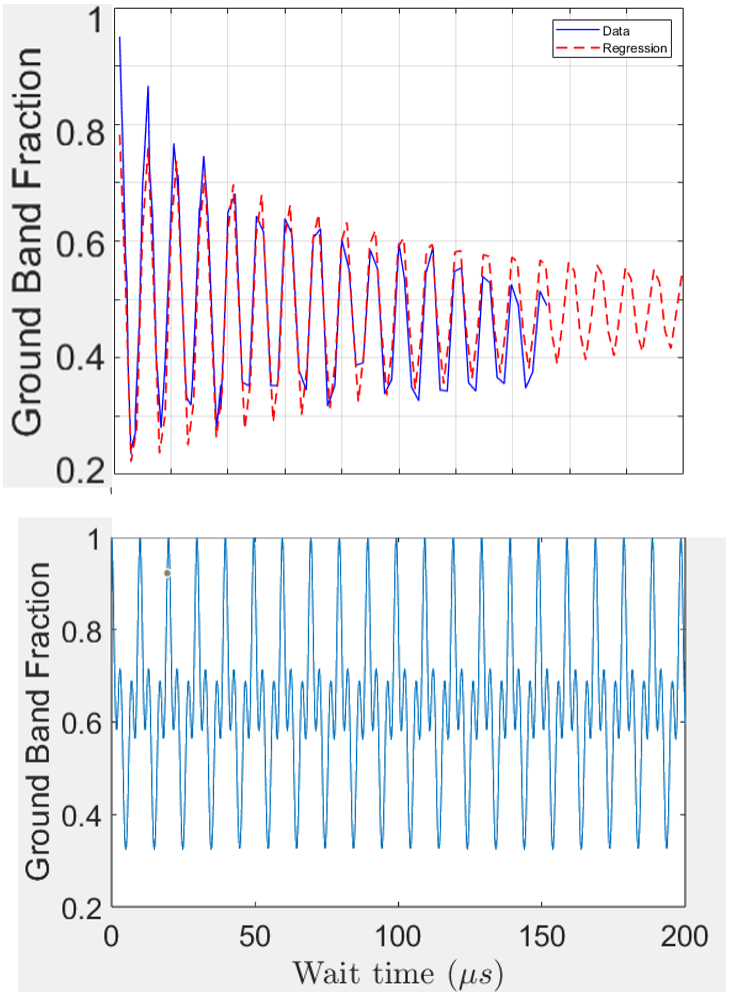

Fig. 3.6: 2-kick interferometric experiments for a 13 E_R lattice showing coherent oscillations in the ground band ($0\hbar k_L$) population. Top panel shows experimental data with an overlaid decaying sine regression. Bottom panel shows TDSE simulations at equivalent parameters also showing oscillations at the Talbot period. The x-axis is the same for both plots. The kick pulses have a duration of 2.2 μs, corresponding to a $\pi/2$ pulse, where 2π is again the band gap period.

3.4.3 Quantum Resonances

One last feature of the QKR that can be explored in the low kick regime is the *quantum resonance* [45, 46], which occur for specific values of T. We've already discussed the primary resonance, which occurs when kicking at the Talbot time $T_{Talbot} = 9.93$ μs such that the 0 momentum state can grow unbounded in energy. There also exist higher order

quantum resonances which occur at fractions of the Talbot time. An example of a higher order resonance is shown in Fig. 3.7, where the atoms are kicked at a period of $T_{Talbot}/2$. This is known as the *antiresonance*, and is equivalent to performing successive 1-kick time reversal experiments, as discussed in 3.1.3. In theory, these resonances occur for any period $\frac{r}{s}T_{Talbot}$ where r and s are integers [30]. Examples of higher order resonances are shown in Fig. 3.8, where various values of $\frac{r}{s}$ are marked with vertical lines. The signature of a higher order resonance typically manifests as a feature when looking at the energy of the atoms as a function of T, and occurs due to nonrandom phase interference between the momentum modes. While the resonances theoretically only occur for the 0 momentum mode, our quasimomentum width ($\approx 0.1\hbar k_L$) is sufficiently narrow to resolve these features. The physics of the resonances is interesting on its own, but for our application they mainly serve as regions to avoid when choosing values for the period. This minimizes unwanted signatures in energy when trying to isolate the effects of interactions. This was a problem faced for many weeks when initially taking data, as faster energy growth decreases SNR. This is due to each of the individual orders having less atoms overall, and the higher momentum orders exploring the edges of the camera sensor.

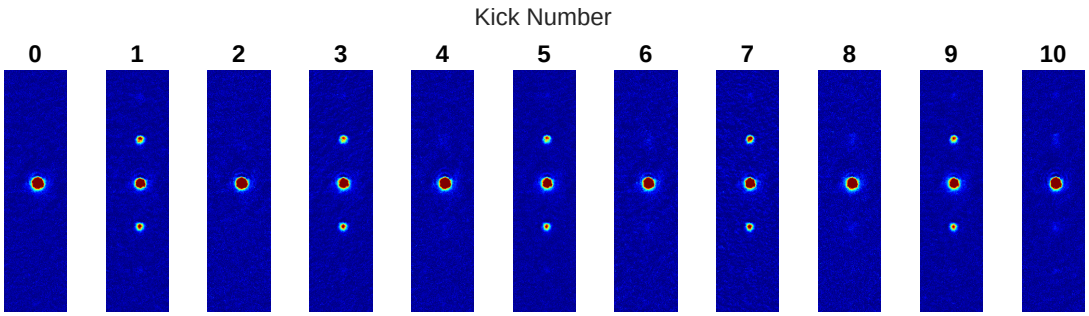

Fig. 3.7: Atomic images after a 2 ms TOF for successive kick numbers at the antiresonance, with a period of $T = 4.95$ μs. The atoms oscillate between the 0th and 1st momentum orders, with no clear energy growth.

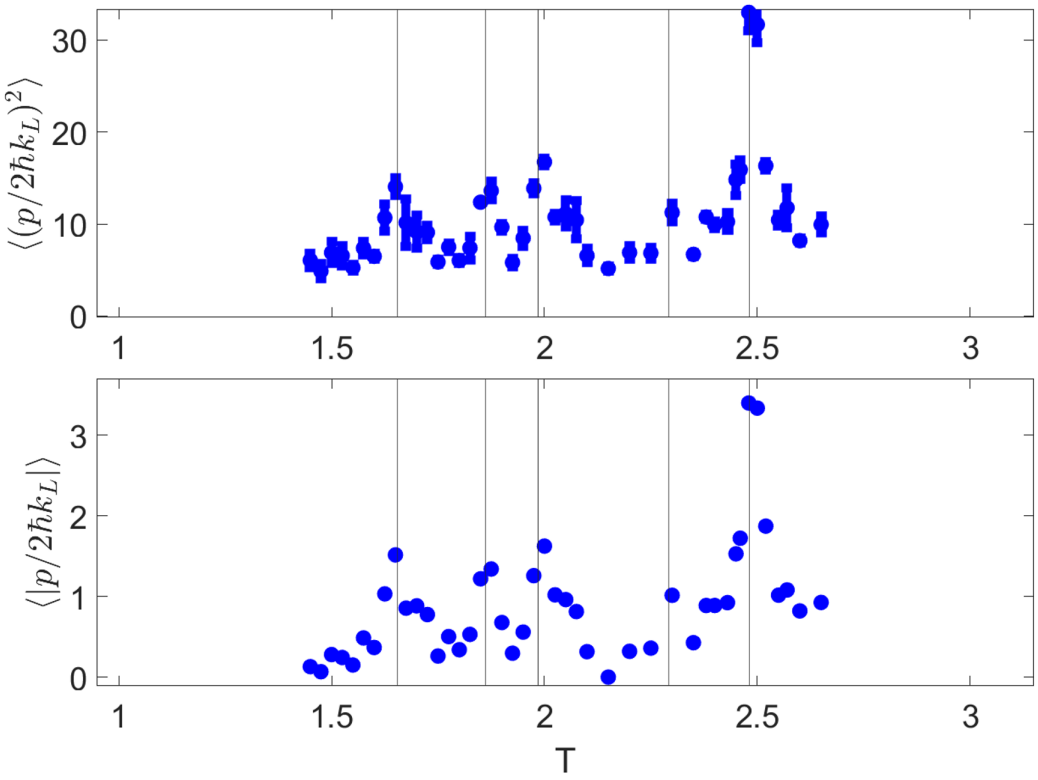

Fig. 3.8: Energy and absolute momentum for a 10-kick QKR experiment while varying the period T. Higher order fractional resonance features can be seen following the vertical lines left to right at 1/6, 3/16, 1/5, 3/13, and 1/4 multiples of T_{Talbot}. The x-axis unit is μs.

3.5 Results

This section closely follows a blog post I wrote for the Behind the Paper blog in Nature [47]. This work has also been published in Nature Physics [42].

The first result to examine is the QKR without the presence of interactions. What do we expect?

In Fig. 3.9, a stacked sequence of images reveals the momentum distribution of the atoms as a function of the number of kicks applied. The first few kicks populate non-zero momentum states, but subsequent kicks do not further alter this distribution; in effect, the momentum distribution is "frozen", despite continued violent kicking! This

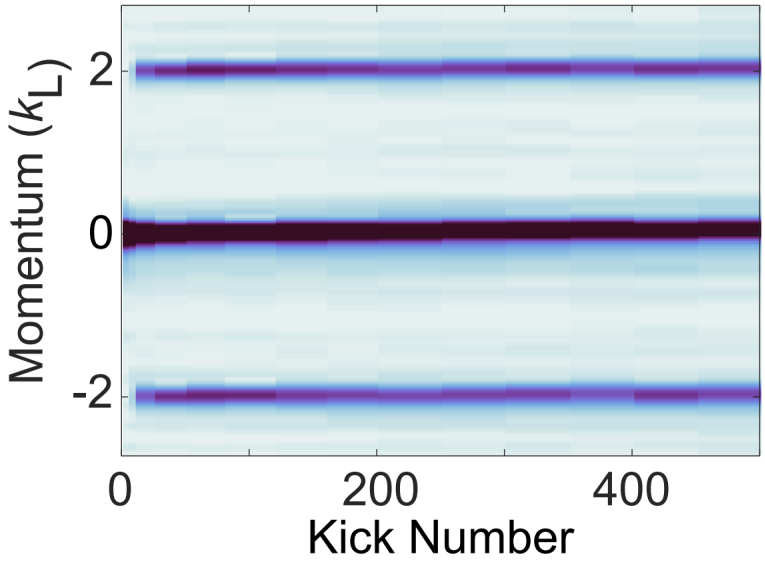

Fig. 3.9: Noninteracting QKR momentum distribution for variable kick numbers

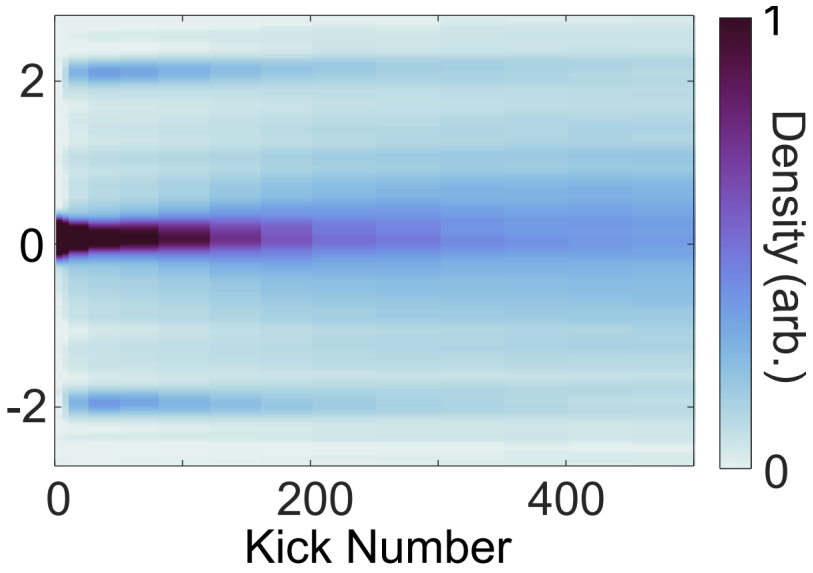

Fig. 3.10: Interacting QKR momentum distribution for variable kick numbers. S-wave scattering length set to $240a_0$

surprising and non-intuitive result showcases the emergence of dynamical localization.

Now let's add interactions into the mix, shown in Fig. 3.10. As time progresses and more kicks are applied, the atoms begin to smear between the momentum states due to interparticle scattering, resulting in a blurrier image as you move towards the right

in the figure. The way in which these scattering events affect the overall momentum distribution provides insight into how interactions affect dynamical localization. Let's explore this more quantitatively.

Fig. 3.11a is a graph of kinetic energy (proportional to the variance of the momentum distribution) over time for 3 different s-wave scattering lengths (0 a0, 240 a0, and 760 a0 where a0 is the Bohr radius, shown by the circles, squares, and diamonds respectively). Larger values of the scattering length correspond to stronger interatomic interactions.

Here the breakdown of dynamical localization is clear. For the noninteracting sample, the energy stays constant even out to 1000 kicks. As the interactions are increased to 240 a0, there is a departure in energy after a few hundred kicks, and we can see for the 760 a0 case that the energy grows at all times. Crucially, this energy growth is significantly slower than the diffusive growth expected for the classical system, shown by the solid blue line and associated data (triangles) in the inset. This "anomalous diffusion" has been predicted in prior theory work [39], but the good agreement of that prediction with our data is rather surprising due to the 3D nature of the experiment and lack of transverse confinement.

One further method by which we can gain insight is to examine the evolution of the momentum distributions directly. In Fig. 3.12, time progresses from yellow to purple, and the two columns show the same data but on different scales (linear vs. log on the y-axis).

In the noninteracting case (c,f), we can see similar momentum distributions for all values of n past 10, indicative of the aforementioned "freezing" of the distribution caused by localization. For the larger interaction strengths, we see the smearing expected due to the presence of interactions, but perhaps surprisingly also see a much larger departure in the tails of the distribution (most prominently shown in h, which is plotted logarithmically). This distribution is still not entirely explained, as there is no expectation for

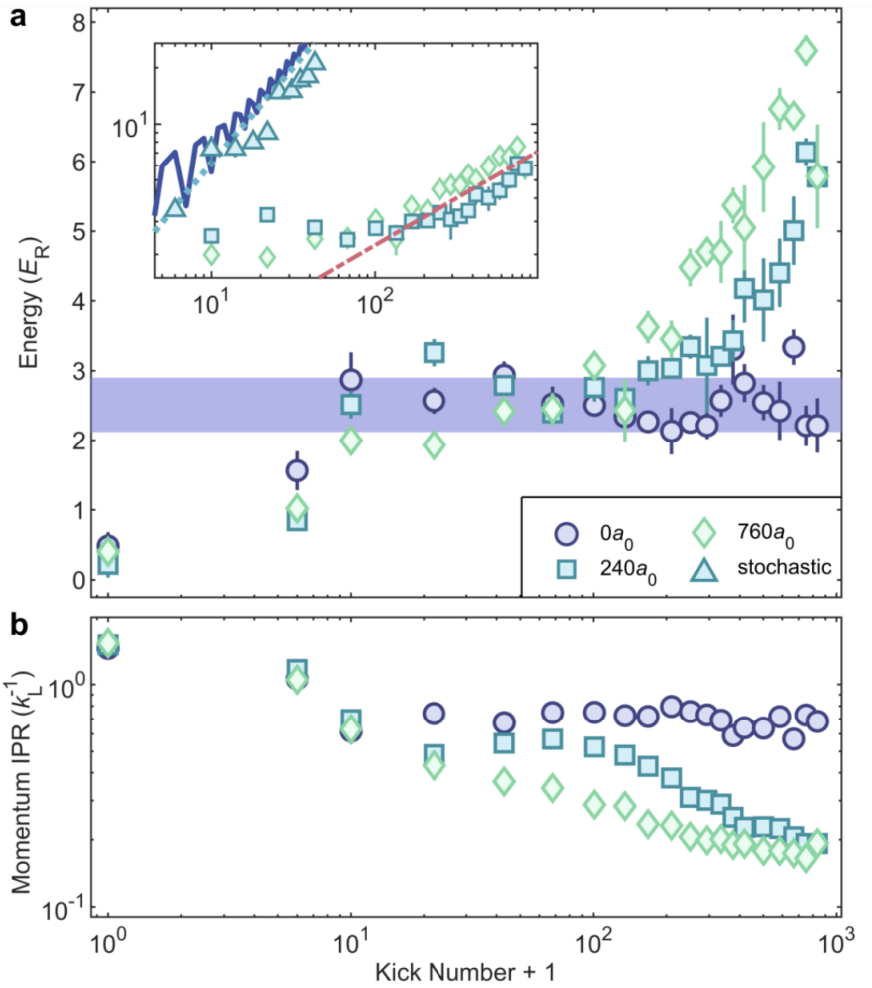

Fig. 3.11: **Observing the interaction-induced emergence of quantum chaos.** (**a**) Energy versus kick number for different scattering lengths a. Blue horizontal shaded region indicates the measured single-rotor localization energy of $E_{\mathrm{loc}} = 2.5(4)E_{\mathrm{R}}$. Here $V_0 = 64E_{\mathrm{R}}$, $T = 1.2\mu$s and $\tau = 300$ ns ($K \approx 2.3$ and $\bar{k} \approx 1.5$). The inset contrasts the measured interaction-induced anomalous diffusion with classical-like diffusion caused by random kicking, the latter achieved by adding random offsets to the average kick spacing T drawn uniformly from the interval $[-T/4, T/4]$. The solid curve is noninteracting quantum theory and the dotted line is a diffusion curve $4Dn/\bar{k}^2$ with $D \approx 0.19$ extracted from the classical standard map. The red dot-dashed line is a subdiffusive $\sqrt{n}$ law serving as a guide to the eye. Error bar computation is discussed in the Methods section. (**b**) Evolution of effective 1D momentum-space IPR.

the lower energy modes to maintain an exponentially localized envelope.

This interaction-induced delocalization marks a transition to the regime of many-

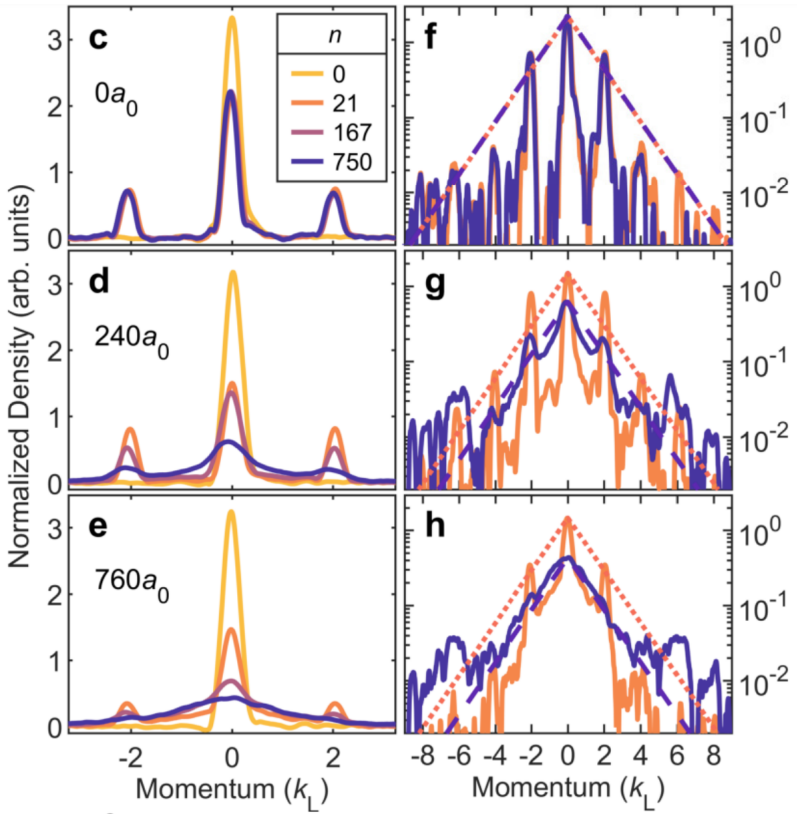

Fig. 3.12: (**c-e**) Normalized momentum space densities at various kick numbers n. (**f-h**) The same densities on a logarithmic y-scale. The orange dotted and purple dashed lines are exponentially localized curves $\sim \exp(-k/k_{\mathrm{loc}})$ with $k_{\mathrm{loc}} = 1.2(1)k_{\mathrm{L}}$ and amplitude normalized to match the peak of the measured distributions at the given kick number. (**i**) Deviation from exponential localization over time based on integrated ratio between measured and exponential distributions with error bars computed from uncertainty in k_{loc}.

body quantum chaos, which we can probe in another interesting way. Prior experiments [41] have shown that effective reversal of the flow of time can be achieved by reversing the phase of the kicks in the QKR when on resonance, or equivalently waiting a half period between two equal trains of resonant kicks. This protocol effectively allows us, if nothing interferes with the reversal, to go "backwards" in time after a set number of kicks and return to the initial state. The effectiveness of the procedure can be measured by comparing the final state to the initial state.

A schematic of this protocol is shown in Fig. 3.13, and an example data set is shown

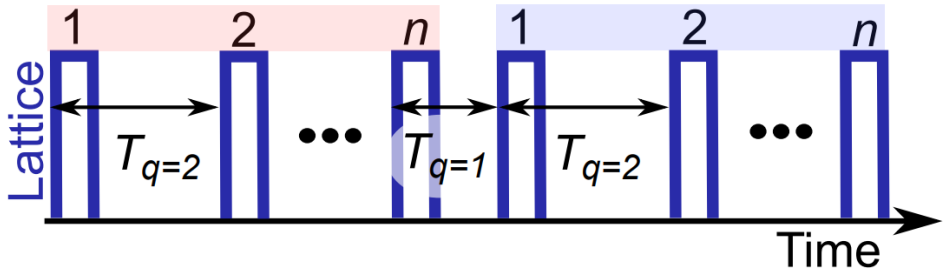

Fig. 3.13: Schematic of the time-reversal echo sequence with two trains of n pulses with period $T_{q=2} \approx 9.95\mu$s separated by a wait-time of $T_{q=1} \approx 4.98\mu$s. The first set of n kicks propagates the system *forward* in time and a second time-reversal set of n kicks propagates it *backwards*.

in Fig. 3.14.

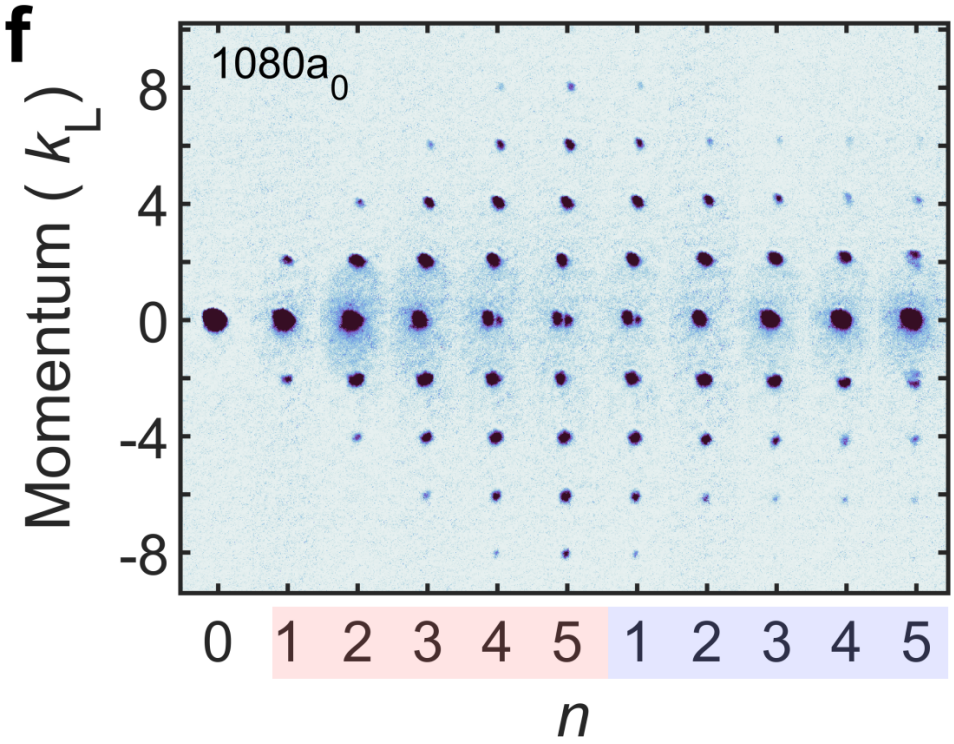

Fig. 3.14: Averaged absorption images of a BEC after the first n kicks of a $2n = 10$ echo protocol, for a scattering length of 1080 a_0.

Five resonant kicks are initially applied to the BEC, followed by a half period delay before applying 5 more resonant kicks. We see that once we start applying the second set of kicks, the momentum orders start to "come back" (not to be confused with the famed

"quantum boomerang" [48]). If the Hamiltonian was perfectly reversed, after the 10th kick we'd observe the initial 0 momentum state again, but the finite momentum width and the inability to reverse the interaction energy modifies this picture. The modification due to the interactions is what we wanted to investigate.

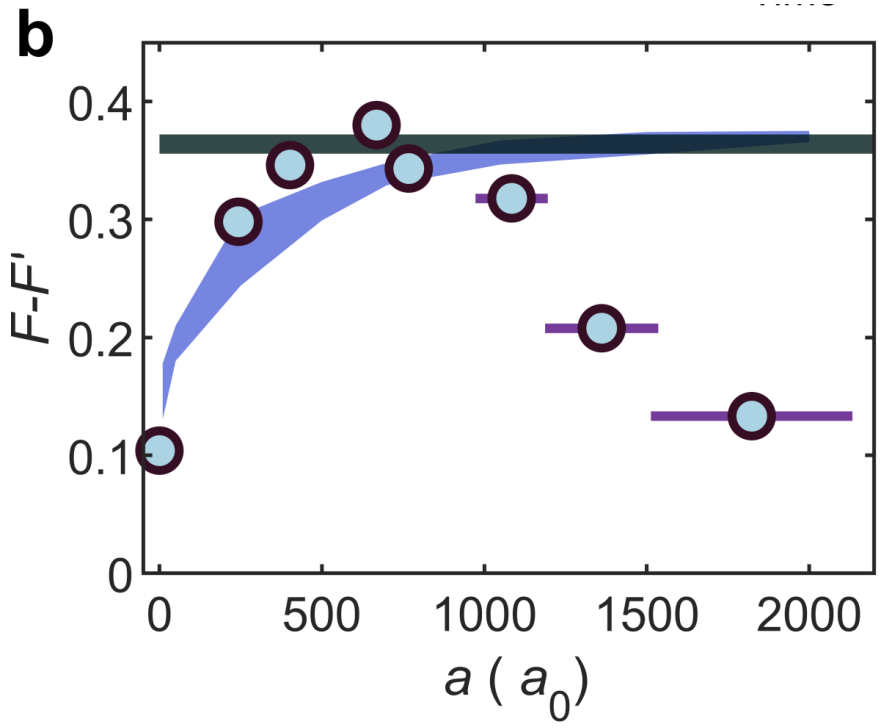

Fig. 3.15: Measured differential fidelity $F - F'$ for a range of scattering lengths a=[0,1800]a0 for 2n=8, where 2n indicates the total number of kicks. The circles show the experimental data. The blue-shaded curve shows the results of a non-interacting numerical simulation and the horizontal line shows the simulated asymptotic value of $F - F'$. The clear departure of the most strongly interacting points from this line is a signature of the interaction-driven destruction of reversibility.

Fig. 3.15 shows the fidelity, or the degree to which time reversal is preserved, as a function of interaction strength. This brings us to the last surprising point of the experiment: the fidelity is non monotonic with respect to interaction strength! Intuitively, one would expect that as interactions are increased, interatomic collisions would scramble the phase information required to successfully reverse time. While this is true after a certain value, we observe that for smaller interactions the fidelity actually increases as

the strength is increased. As unexpected as this seems, the behavior can actually be explained with a fundamental argument about BECs: as the interaction strength is increased, the Thomas-Fermi spatial width increases, and correspondingly the width in momentum space decreases, increasing the fidelity. This is shown by the shaded blue theory curve in the figure. Crucially, this occurs before the collisional time scale of the smaller interaction strengths. As interactions are turned up, interactions dominate the dynamics before the time reversal can occur, inducing irreversibility.

3.6 Conclusions

In conclusion, we have experimentally realized a many-body ensemble of quantum kicked rotors. Following the evolution of interacting samples over hundreds of kicks, we observe signatures of an initial transient steady state, followed by an interaction-induced breakdown of dynamical localization via anomalous diffusion, signaling the onset of many-body quantum chaos. Characterization of the departure from the dynamically localized state indicates subdiffusive energy growth with an exponent near 0.5, easily distinguishable from classical Joule heating in a randomly kicked system, and reveals momentum space distributions which are not exponentially localized. Measuring echo time-reversal dynamics with a quantum resonance enabled us to directly probe the role of interaction-induced irreversibility in driving a transition to many-body quantum chaos. Together, these results demonstrate and quantitatively illuminate the emergence of interaction-driven quantum chaos in a paradigmatic localized system.

Chapter 4

Quantum Boomerang Effect

The next experiment uses the quantum kicked rotor as a starting point to observe a fundamental *dynamical* signature of Anderson localization known as the quantum boomerang effect. In detailing this effort I'll introduce a unique feature of our lithium machine, a second coaxial optical lattice, and argue that we have realized a probe for the quantum-mechanical nature of localization. An extensive discussion of symmetry is included to fully characterize the existence of the quantum boomerang in the kicked rotor.

4.1 Existence and Realization

While Anderson localization has been a staple of condensed matter theory for over 50 years, its dynamical signature known as the quantum boomerang effect (QBE) wasn't discovered theoretically until 2019. The QBE involves a particle initialized in an Anderson localized system with some nonzero initial velocity. If the system is classical, the expectation is for the particle to move some distance away from the origin and and eventually stop, a mean free path argument that can be demonstrated via the Boltzmann equations [49]. In the quantum regime, the particle's behavior is remarkably different.

Instead of stopping some distance away from the origin, a quantum particle will turn around after an initial departure, return to its origin, and remain there. This is a result of the combination of Anderson localization and time reversal symmetry inherent to the system.

4.1.1 Proof of the QBE

The existence of the QBE can be demonstrated fairly simply, relying only on the two ingredients mentioned above. The proof below follows [49]. Start with a 1D system obeying the Hamiltonian

$$H = \frac{-\hbar^2\nabla^2}{2m} + V(x), \tag{4.1}$$

where V(x) is an uncorrelated random potential whose average value is 0. A normalized Gaussian wavepacket $\Psi_{k_0} \propto \exp[-x^2/(2\sigma^2) + ik_0x]$ is initialized in this potential with a finite momentum $\hbar k_0$. The probability distribution can be written as

$$|\Psi(x,t)|^2 = \sum_{n,m} \langle\phi_n|\Psi_{k_0}\rangle \langle\Psi_{k_0}|\phi_m\rangle \phi_n(x)\phi_m^*(x)e^{-i(\epsilon_n-\epsilon_m)t/\hbar} \tag{4.2}$$

where ϵ_n and $|\phi_n\rangle$ are the eigenenergies and eigenstates of H. Since the eigenstates are localized, the system is constrained by both a localization length and time. For times much longer than the localization time the off-diagonal oscillatory terms $n \neq m$ in Eq. 4.2 disappear, yielding

$$|\Psi(x,\infty)|^2 = \sum_n |\langle\phi_n|\Psi_{k_0}\rangle|^2|\phi_n|^2. \tag{4.3}$$

This system obeys time-reversal invariance, so $\phi_n(x)$ are real and $\langle\phi_n|\Psi_{k_0}\rangle = \langle\phi_n|\Psi_{-k_0}\rangle^*$. Thus, Eq. 4.3 is independent of the sign of k_0, and the long-time density distribution is equivalent to that of one where the initial wavepacket has a symmetric velocity distribution. The center of mass therefore must return to the origin at long times, realizing the QBE.

4.1.2 Realization of the QBE in the quantum kicked rotor

In section 3.1.2, the mapping between the QKR and AL was established. The QBE is expected to exist in AL systems, and thus can be expected to exist in the QKR as well, with the boomerang occurring in momentum space rather than position space. This was first theorized and numerically simulated in [29] in 2021. I'll first show the derivation of the conditions necessary for the QBE in the QKR, published in Appendix A of our paper [48], then show the results of the simulation from [29].

We consider the canonical QKR Hamiltonian considered in the previous chapter with a slight modification

$$\mathcal{H}_\alpha(t) = \frac{p^2}{2} + K\cos x \sum_{n=-\infty}^{\infty} \delta(t - n - \alpha). \tag{4.4}$$

To be explicit, here we define α on the interval $[0, 1]$, taking the cases $\alpha = 0$ and 1 to be distinct from each other and consistent with the definition in the Floquet operator

$$U_\alpha = e^{-i(1-\alpha)p^2/2\hbar} e^{-iK\cos x/\hbar} e^{-i\alpha p^2/2\hbar}. \tag{4.5}$$

α, which we'll refer to as the *Floquet gauge*, represents the fraction of period waited before subjecting the wavepacket to the first kick. Different α values are graphically depicted in Fig. 4.1. $\alpha = 0$ corresponds to the kick occurring immediately when the evolution

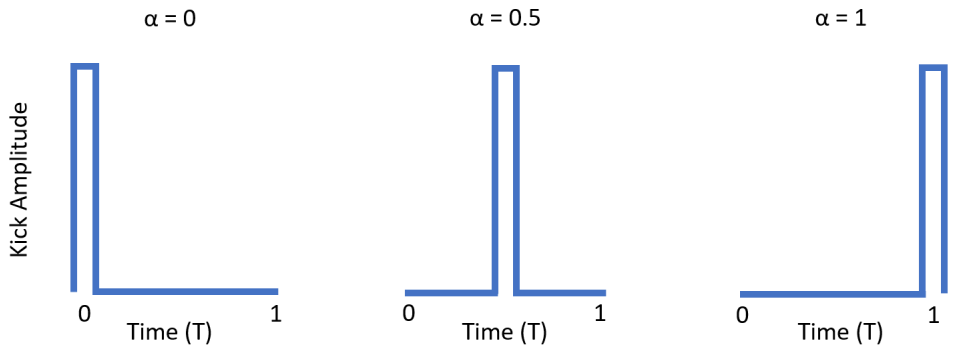

Fig. 4.1: Visualization of different α values. The plots show time series of the kick amplitude immediately after preparation of the initial state, at $t = 0$. The kicks here are shown as pulses to reflect our experimental protocol.

starts, and the propagator becomes equivalent to standard QKR propagator 3.4. $\alpha = 1$ corresponds to a full period of free evolution before the first kick is applied, while $\alpha = 1/2$ causes the two free evolution terms in the propagator to become equivalent. The full propagator describes the time evolution over the range [n-α, n+1-α], with n representing the time the instantaneous kick occurs.

In the following, we refer to symmetry operations only about fixed axes. $\mathcal{H}_\alpha$ is parity inversion ($x \to -x$, $p \to -p$) symmetric at all times

$$[\mathcal{P}, \mathcal{H}_\alpha(t)] = 0. \tag{4.6}$$

The operator $\mathcal{P}$ obeys $\mathcal{P}^\dagger p \mathcal{P} = -p$. Only for $\alpha = 1/2$ does the system also become time-reversal ($t \to -t$, $p \to -p$) symmetric. The complex conjugation operation $\mathcal{K}$ associated with time-reversal acts on the position space wave-function as $\langle x | \mathcal{K} | \psi \rangle = \psi^*(x)$. For the $\alpha = 1/2$ case, $\mathcal{H}_\alpha$ is additionally parity-time inversion ($t \to -t$, $x \to -x$) symmetric.

We use the following intuitive definition for the QKR boomerang effect in momentum space. (i) The boomerang should exhibit non-trivial average momentum dynamics at short times, in particular a departure from followed by a relaxation toward the initial

value. (ii) At late times, a true boomerang should have an average momentum equivalent to the initial momentum. Explicitly, we will show that (i) is only compatible with parity asymmetric states. Restricting ourselves to the case of 0 initial momentum, we then show that time-reversal symmetry of the quenched initial state and Floquet gauge guarantees (ii).

We consider solutions to the time-dependent Schrodinger equation $i\hbar\partial_t |\psi(t)\rangle = \mathcal{H}_\alpha(t) |\psi(t)\rangle$, where $|\psi(t=0)\rangle$ is the initial state quenched into the Hamiltonian. Our analysis will concern the behavior of $\langle p(t)\rangle = \langle\psi(t)| p |\psi(t)\rangle$. First we consider the evolution of an arbitrary state $|\psi(t=0)\rangle$ and its parity inverted counterpart $|\phi(t=0)\rangle \equiv \mathcal{P}|\psi(t=0)\rangle$. Let $\langle p(t)\rangle$ and $\langle\tilde{p}(t)\rangle$ correspond to the time-evolved states $|\psi(t)\rangle$ and $|\phi(t)\rangle$ respectively. From parity symmetry (4.6), we have $|\phi(t)\rangle = \mathcal{P}|\psi(t)\rangle$, and from this can conclude

$$\langle\tilde{p}(t)\rangle = \langle\psi(t)|\mathcal{P}^\dagger p\mathcal{P}|\psi(t)\rangle = -\langle p(t)\rangle. \tag{4.7}$$

This holds for any initial state and α, as well as at all times t. From this, it immediately follows that a necessary condition for observing (i), and thus the boomerang, is that $|\psi(t=0)\rangle \neq \mathcal{P}|\psi(t=0)\rangle$; otherwise $\langle\tilde{p}(t)\rangle = \langle p(t)\rangle = 0$, guaranteeing that (ii) is satisfied but in a trivial way. Since all of the remaining analysis is also concerned with $\langle p(t)\rangle$, we hereafter assume that parity asymmetry is satisfied to derive non-trivial results.

Now we begin to investigate the $t \to \infty$ behavior concerning (ii). Considering the Floquet spectral decomposition of the initial state $|\psi(t=0)\rangle = \sum_m c_m |\varphi_m^\alpha\rangle$ with $U_\alpha |\varphi_m^\alpha\rangle = e^{-i\omega_m^\alpha} |\varphi_m^\alpha\rangle$, the long-time average momentum given by the Floquet diagonal ensemble is

$$\langle p(t \to \infty) \rangle = \sum_m |c_m|^2 \langle \varphi_m^\alpha | \, p \, | \varphi_m^\alpha \rangle \, . \tag{4.8}$$

The Floquet diagonal ensemble is a rather useful proxy predicting the infinite time behavior of this system, and is used as a benchmark for many of the results shown in this chapter.

One can also consider the opposite limit $t \to -\infty$ by decomposing in the basis of $U_\alpha^\dagger$. Since the eigenstates of a unitary operator and its Hermitian-conjugate are identical (both are eigenstates of the same self-adjoint, time-independent Floquet Hamiltonian), the prediction of the Floquet diagonal ensemble is the same. This leads to the conclusion that

$$\langle p(t \to \infty) \rangle = \langle p(t \to -\infty) \rangle. \tag{4.9}$$

This also holds for any initial state and α.

Now finally we consider time-reversal symmetric states $\mathcal{K} \, |\psi(t=0)\rangle = |\psi(t=0)\rangle$. Under parity-time inversion, we then have the relation

$$\mathcal{PK} \, |\psi(t=0)\rangle = \mathcal{P} \, |\psi(t=0)\rangle \equiv |\phi(t=0)\rangle \, . \tag{4.10}$$

Now consider the full solution $|\psi(t)\rangle$ and $\langle p(t) \rangle$. For $\alpha = 1/2$, the parity-time inversion symmetry of the Hamiltonian implies that $\mathcal{PK} \, |\psi(-t)\rangle$ is another solution with a corresponding momentum evolution $\langle p(-t) \rangle$. From (4.10), it is straightforward to see that this solution corresponds to the evolution of the parity-inverted initial state, i.e. $|\phi(t)\rangle = \mathcal{PK} \, |\psi(-t)\rangle$; **note** that while a parity-time inverted state about a different time-axis can be defined for arbitrary α, such a state will not coincide with $|\phi(t)\rangle$ and will

consequently prevent the following conclusions. Defining $\langle\tilde{p}(t)\rangle$ in the same way as before, this result implies $\langle\tilde{p}(t)\rangle = \langle p(-t)\rangle$. Combining this with (4.7), we thus have

$$\langle p(-t)\rangle = -\langle p(t)\rangle. \tag{4.11}$$

One can deduce this relation intuitively by noting that backward propagation under $U_{\alpha=1/2}$ for a time-reversal symmetric initial state simply corresponds to receiving kicks of the opposite sign. Finally, the combination of (4.9) and (4.11) yields the final result

$$\langle p(t \to \infty)\rangle = 0, \tag{4.12}$$

thus proving the existence of the quantum boomerang effect in the QKR.

A numerical simulation of the QBE in the QKR is given in [29]. The simulation starts with a wavepacket of the form

$$\psi_{n,\beta}(t=0) = N\exp[-\frac{\hbar^2(n+\beta)^2}{2\sigma_p^2(0)} - i(n+\beta)x_0]. \tag{4.13}$$

Here N is a normalization constant, $\sigma_p(0)$ is the Gaussian width of the wavepacket in momentum space, and the x_0 is the initial boost, corresponding to an initial nonzero velocity in the position-space boomerang. This wavepacket is evolved forward in time via the Floquet propagator 4.5.

Fig. 4.2 shows the results of numerical simulations for $\alpha = 0, 1/2,$ and 1, represented by the green-dashed, blue dot-dashed, and purple lines respectively. Here the QBE manifests as a localization in *average* momentum, as opposed to position in the typical QBE. Interestingly, the momentum only localizes to its initial value for $\alpha = 1/2$, while for other α $< p(t) >$ saturates to a nonzero value. This is due to the fact that $\alpha = 1/2$ causes $U(\alpha)$ to become time-reversal symmetric, a necessary condition following 4.3.

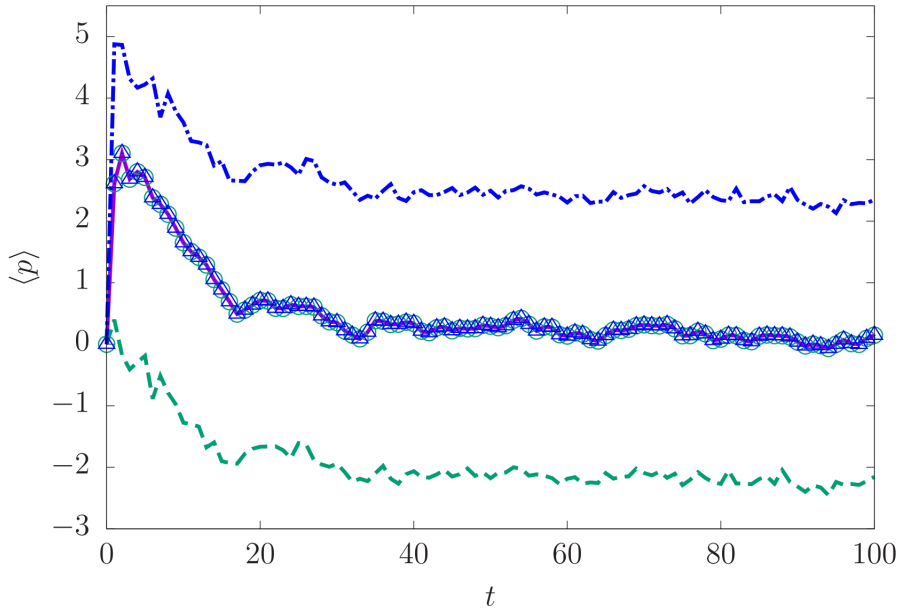

Fig. 4.2: Numerical simulation of average momentum $< p >$ as a function of kick number for values of $\alpha = 0, 1/2, 1$, corresponding to the green, blue, and purple lines respectively. Only $\alpha = 1/2$ displays a signature of the quantum boomerang effect. Results taken from [29].

Intuitively, this can be understood by seeing that for $U(1/2)$, the free evolution terms become equivalent, and thus moving forwards or backwards in time results in a half period of free evolution, a kick, and then another half period of evolution. This does not hold true for any other value of α.

Following the above analysis, I created a simulation adapting this methodology for our own system, assuming a BEC in an optical lattice with typical experimental parameters, to determine whether this protocol would indeed show the QBE in our system. During the making of the simulation there was one key question: how do you give the BEC an initial boost?

The answer happens to be serendipitous for our machine. The QBE in the QKR requires a coherent boost in position for all of the particles in the BEC (since this is a noninteracting atomic cloud, each particle represents a separate instance of the experi-

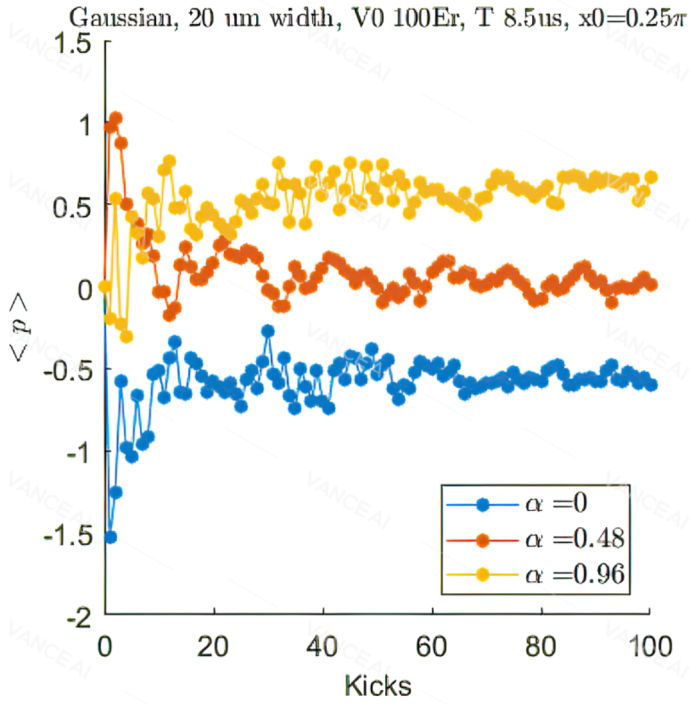

Fig. 4.3: Numerical simulation of average momentum $< p >$ as a function of kick number for three values of α. Only $\alpha \approx 1/2$ displays a signature of the quantum boomerang effect.

ment). The particles can first be localized in position by loading them adiabatically into an optical lattice. Once the lattice is snapped off to start the QBE protocol, a second coaxial *spatially phase-shifted* lattice can be used to administer the kicks, and this relative phase-shift constitutes a position displacement that prepares the correct initial state for the QBE. Fortunately, our setup happens to have this second lattice, and is one of the only experiments in the world to do so (though historically for unrelated experiments involving strongly driven optical lattices [2]). The configuration will be described in the next section.

Early sample simulations for our system are shown in Fig. 4.3. Here the BEC is modeled as a Gaussian wavepacket with a 20 μm width, loaded into a 100 E_R 1064 nm optical lattice and kicked with a secondary lattice shifted spatially by a phase of $\pi/2$. A finite pulse duration of 300ns is included in the simulation to reflect realistic

experimental parameters. Here α is defined as the time between the primary lattice turning off and the kicking lattice turning on divided by the period T, and thus the QBE occurs at an α slightly < 0.5 due to the finite pulse width. Simulations like these in addition to discussions with Tommaso Macri and Patrizia Vignolo inspired the efforts discussed in the following sections, as they realized the possibility of observing the QBE experimentally in our system.

4.2 Dual lattice experimental setup

Due to the close relationship between the QKR and QBE, a large portion of their experimental setups are identical. The added feature for the QBE is the presence of a second coaxial lattice, which will provide the initial position-space offset necessary to observe the QBE in momentum space. The alignment for this second lattice is relatively straightforward, as the power to the lattices is split from the main 1064 nm light into two identical paths for the two lattices. Typically, only the input alignment has to be carefully performed, as the retro should be close to optimal at the same position for both lattices once they are coaxial. The procedure to align the input for the second lattice is the same as the procedure outlined in section 2.3. It is worth noting that the two lattices combine on a PBS before the input lens to the chamber, so they have orthogonal polarizations.

Once both lattices are aligned, the critical feature to adjust is their relative phase. To achieve this, we have two $\lambda/4$ waveplates before the retro mirror. This configuation is shown in Fig. 4.4. The Jones matrix analysis for this configuration is outlined at the end of [2]. Adjusting the waveplate by θ directly before the retro mirror, a relative phase of of 4θ is created between the horizontal and vertical components of the polarization. This allows for precise tuning of the relative phase difference between the two lattices.

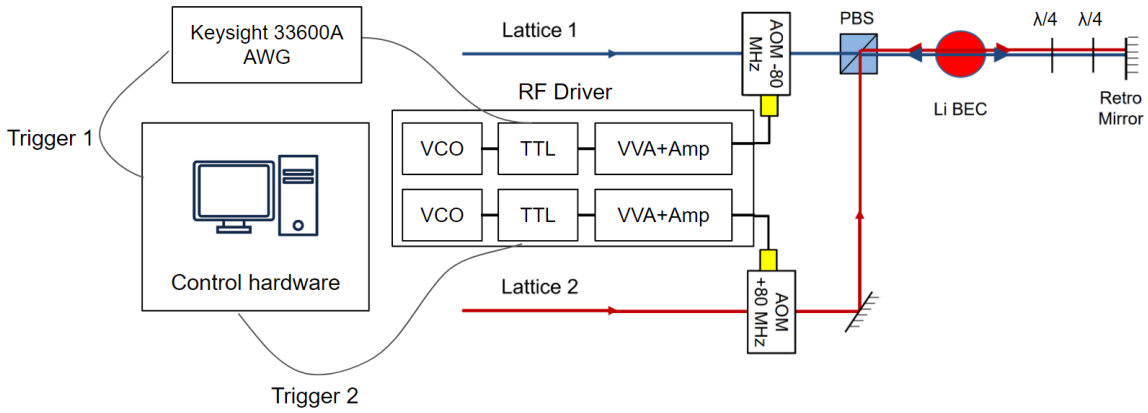

Fig. 4.4: Electronic and optical setup for the optical lattices. A driver box comprising of 2x voltage-controlled oscillators (VCO), TTL switches, and VVA+amplifiers creates an 80 MHz RF source with appropriate amplitude to drive each AOM controlling one of the optical lattice paths. For the lattice used in the QKR experiments (Lattice 1), the TTL is controlled by a Keysight AWG generating a pulse train. The retroreflection of the incoming laser beam by the retro mirror creates a standing wave optical lattice potential experienced by the atoms in the Li BEC.

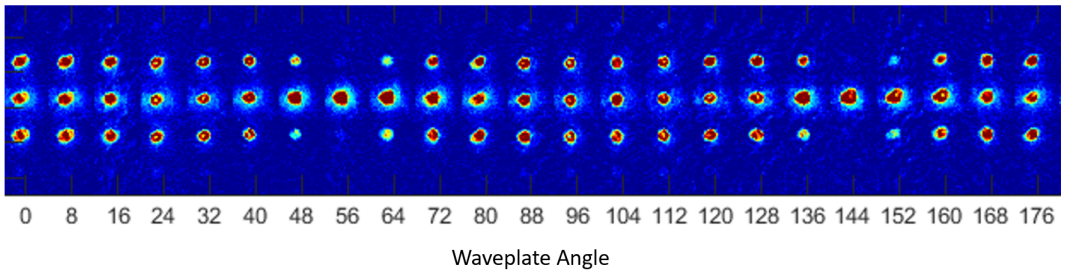

Fig. 4.5: TOF atomic images after KD experiments while varying the second $\lambda/4$ waveplate angle.

The readout of the relative phase can be accomplished by performing Kapitza-Dirac (KD) experiments with both lattices at equal power while varying the phase. When the lattices are π-phase shifted, they will destructively interfere, and a KD experiment will yield no population of higher momentum modes. Conversely, when they are perfectly in phase, a KD experiment will yield maximum population of higher order modes. The 0 and π phase shift waveplate locations can be determined quantitatively this way. For the QBE, the signal is maximized at a phase of $\pi/2$ (discussed in the next section and

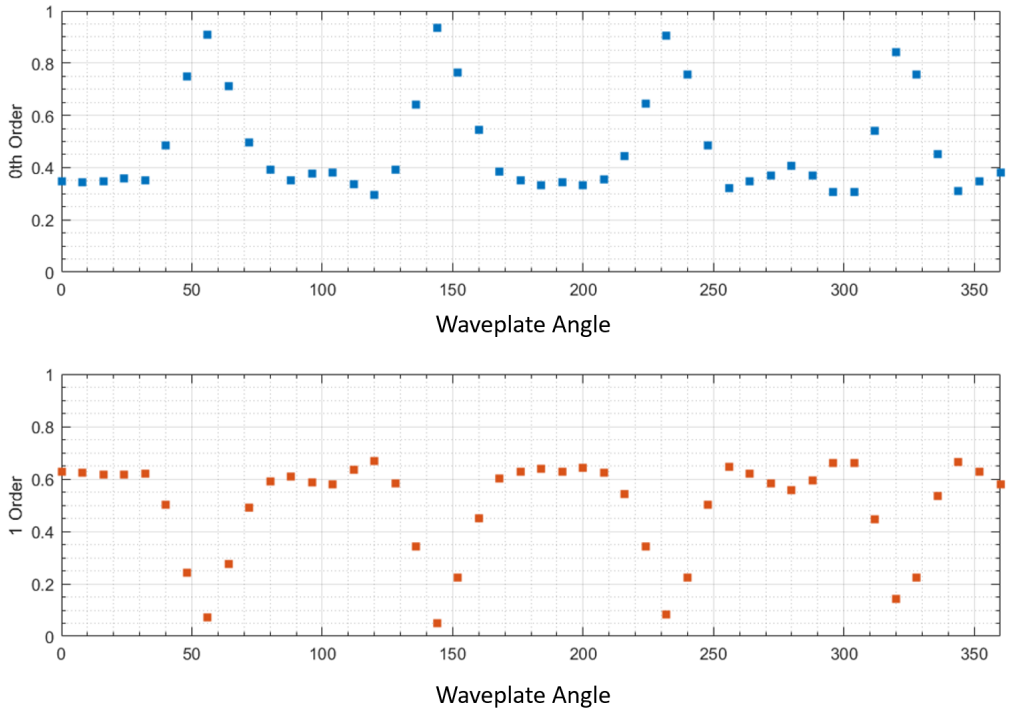

Fig. 4.6: Atom populations in the 0th and 1st momentum order after KD experiment while varying the second $\lambda/4$ waveplate angle. A clear periodicity every 90 degrees is observed due to the 4θ relative phase difference induced by the waveplate rotation.

shown in Fig 4.8f), whose waveplate setting is easily found by going to the midpoint of the 0 and π phase locations. An example run of successive KD experiments for different waveplate positions is shown in Fig. 4.5. The relative atom populations in the 0th and 1st momentum order are shown in Fig. 4.6.

4.3 Observing the Quantum Boomerang Effect

I'll now go through the main results of this experiment, which are published in [48]. We begin each experiment by preparing a Bose-Einstein condensate (BEC) of 10^5 ^{7}Li atoms and then tuning interatomic interactions to zero with the Feshbach resonance. A typical experimental sequence from this point on is depicted in Fig. 4.7a. The atoms are exposed in turn to the two coaxial optical lattices with lattice constant $d = 532\,\mathrm{nm}$, wave

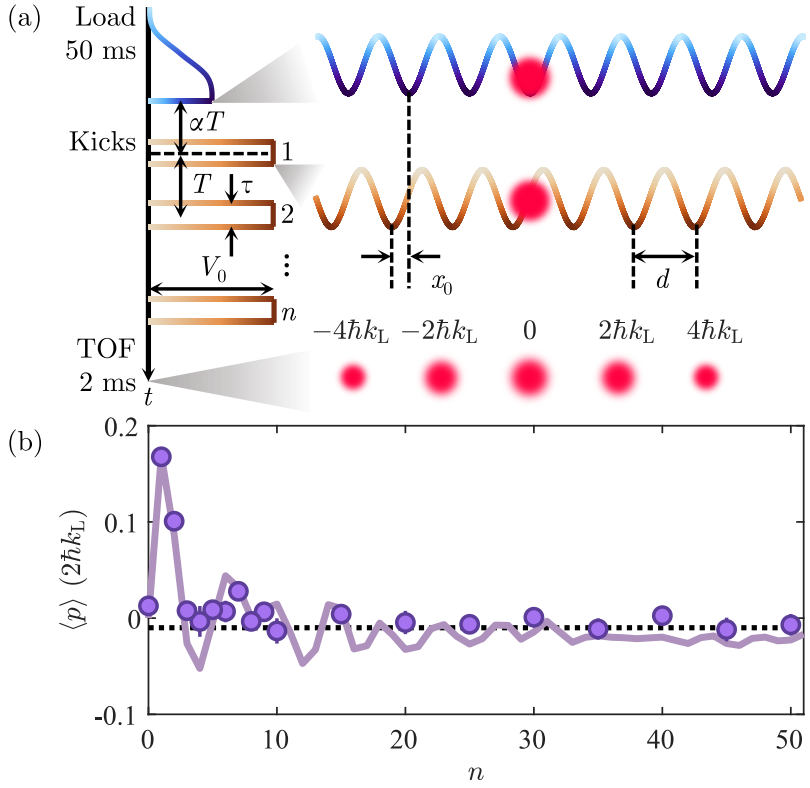

Fig. 4.7: Observation of the quantum boomerang effect. **(a):** Experimental sequence. A BEC is loaded into one optical lattice and then kicked with a second, phase-shifted lattice. The momentum distribution is measured after free expansion. BEC size and timeline are not to scale. **(b):** Measured average momentum versus kick number, for parameters given in the text. The return to the origin demonstrates the quantum boomerang effect. Error bars show standard error of the mean on ten repeated measurements. Solid curve is the numerical prediction. Dotted line represents infinite-time average predicted by the Floquet diagonal ensemble (Eq. 4.8).

vector $k_{\mathrm{L}} = \pi/d$, recoil energy $E_{\mathrm{R}} = \hbar^2 k_{\mathrm{L}}^2/2M$, and tunable relative offset x_0. M is the atomic mass. To prepare an initial wavefunction which is well-localized in position space within each lattice site, we adiabatically load the BEC into the first optical lattice over 50 ms, reaching a final depth of $7\,E_{\mathrm{R}}$. At $t = 0$, we suddenly turn off the first lattice and quench into a Hamiltonian created by repeated kicking with the second, spatially-shifted lattice:

$$H_\alpha = \frac{p^2}{2M} + \frac{V_0}{2}\cos\left(2k_{\mathrm{L}}x\right)\sum_n f_\tau(t - nT - \alpha T). \tag{4.14}$$

As described by Eq. 4.14, the second, phase-shifted lattice is pulsed n times to depth V_0 with pulse shape f_τ, effective pulse width $\tau = 500\,\text{ns}$, and period T; the first pulse peaks a delay time $t = \alpha T$ after the quench. Having measured the finite time of this quench to be approximately 190 ns, we define $t = 0$ halfway through the quench and recognize a systematic ± 0.01 uncertainty in the reported values of α. Figure 4.7b illustrates the main result of this work: we experimentally observe the departure from and return to zero average momentum which is the key signature of the quantum boomerang effect [49]. Here $V_0 = 41E_\text{R}$, $T = 8\mu\text{s}$, $\phi \equiv 2k_\text{L}x_0 = 0.9\pi/2$, and $\alpha = 0.48$. While the first kick imparts momentum asymmetry due to the lattice phase offset, the system returns to zero average momentum at long times. The experimental result agrees well with fit-parameter-free time-dependent Schrödinger equation (TDSE) simulations of the finite-pulse width Hamiltonian (4.14) using a split-step method described in Appendix D of [48].

Figure 4.8 shows the characterization of the QBE with respect to parameters α and ϕ, as well as the difference in average momentum between short times and long times. Fig. 4.8a,b, and c show the difference in late time behavior for different α. In accordance to the time reversal symmetry conditions mentioned in the previous section, we only observe a coherent QBE for α close to 0.5. α's further away demonstrate late time saturation of $< p >$ to nonzero values. The discrepancy between the alpha value in b) and 0.5 can be explained by the finite pulse duration as well as the rise and fall times of our AOMs. The data sets match well with fit-parameter-free TDSE simulations.

Fig 4.8e contrasts the short and long term behavior of the QBE in the kicked rotor system. The short term dynamics are dictated by the Talbot effect (see 3.1.3). The Talbot effect gives rise to periodic reimaging of the wavefunction under free expansion due to diffraction of a matter wave off of a spatial lattice, similar to the repeating pattern observed when a plane wave diffracts off of a periodic grating. A multitude of experiments

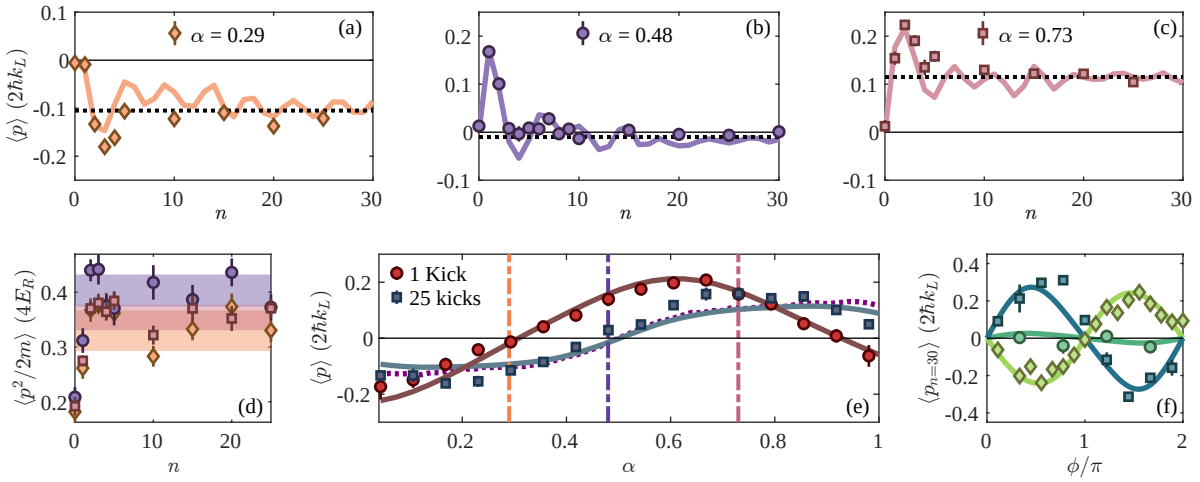

Fig. 4.8: Characterization of the quantum boomerang effect. All error bars show standard error of the mean on repeated measurements. **(a-c):** Average momentum vs. kick number for $V_0 = 41\,E_\mathrm{R}$ and $T = 8\mu$s, at $\alpha = 0.29$, 0.48, and 0.73 respectively. Solid curves show numerical predictions. Dotted lines show infinite-time average momenta predicted by the Floquet diagonal ensemble (Eq. 4.8). $\phi = 0.9\pi/2$ for all experimental runs. **(d):** Measured energy vs. kick number for all three values of α. Shaded areas indicate long-term energy by averaging data points between 10 and 25 kicks. **(e):** Measured average momentum after 1 kick (red circles) and 25 kicks (blue squares) vs. α for the same experimental parameters. Same-color solid lines show numerical predictions. Dashed vertical lines indicate α in (a-c). Dotted purple line shows prediction of the Floquet diagonal ensemble [49]. **(f):** Average momentum after 30 kicks vs. ϕ for $V_0 = 70\,E_\mathrm{R}$, $T = 7\mu$s, and $\alpha = 0.15$ (diamonds), 0.48 (circles), and 1.05 (squares).

have used this Talbot effect to explore quantum resonance phenomena [30, 45, 46, 50].

The long term dynamics are dictated by the symmetries of the initial state and the Hamiltonian. Here I'll fully prove that the infinite time momentum should be an odd function about $\alpha = 0.5$, following Appendix C of [48]. First we consider initial states with time-reversal symmetry such that

$$\mathcal{K}\,|\psi(t=0)\rangle = |\psi(t=0)\rangle \tag{4.15}$$

We note the relation

$$\mathcal{K}^\dagger U_\alpha \mathcal{K} = e^{i(1-\alpha)p^2/2\hbar} e^{iK\cos x/\hbar} e^{i\alpha p^2/2\hbar} = U_{1-\alpha}^\dagger. \tag{4.16}$$

For compactness, we will denote the state after n kicks in the gauge α as $|\psi_n\rangle_\alpha \equiv U_\alpha^n |\psi(t=0)\rangle$ ($|\psi_0\rangle = |\psi(t=0)\rangle$) and use similar notation for expectation values. The momentum evolution in the gauge $1-\alpha$ is then given by

$$\langle p_n\rangle_{1-\alpha} = \langle\psi_0| U_{1-\alpha}^{n\dagger}\, p\, U_{1-\alpha}^n |\psi_0\rangle . \tag{4.17}$$

Using (4.15), (4.16) and $\mathcal{K}^\dagger\, p\, \mathcal{K} = -p$, we find

$$\langle p_n\rangle_{1-\alpha} = \langle\psi_0| \mathcal{K}^\dagger U_{1-\alpha}^{n\dagger} \mathcal{K}\mathcal{K}^\dagger p \mathcal{K}\mathcal{K}^\dagger U_{1-\alpha}^n \mathcal{K} |\psi_0\rangle \tag{4.18}$$

$$= -\langle\psi_0| U_\alpha^n\, p\, U_\alpha^{n\dagger} |\psi_0\rangle = -\langle p_{-n}\rangle_\alpha. \tag{4.19}$$

That is, forward quench dynamics in the gauge $1-\alpha$ possess an opposite momentum evolution to backward evolution under the gauge α. Leaving α arbitrary, taking the limit $n \to \infty$, and applying (4.9), we derive the odd function result for time-reversal symmetric states

$$\langle p_\infty\rangle_{1-\alpha} = -\langle p_\infty\rangle_\alpha. \tag{4.20}$$

Finally, we explore the effect of initial velocity on the late time momentum in 4.8f. Here we vary the relative phase shift between the loading lattice and the kicking lattice, which is analagous to the initial velocity in a position space QBE. For α near 0 and 1, the momentum after 30 kicks has opposite sign and varies sinusoidally, in accordance with TDSE. For α close to 0.5, the late time momentum converges to 0 regardless of

phase, showing the ubiquity of the QBE regardless of the magnitude of position space launch. Thus, the initial velocity does not play a role in the return of the QBE, but rather controls the amplitude of the early time departure.

Initially when attempting this experiment, there were multiple ideas for the preparation of the initial state. Aside from adiabatically loading the BEC into the optical lattice to create a Bloch state, some experiments were performed by kicking with the first lattice instead. This created an exotic initial wavefunction which was more homogeneous in position space, approximately $\psi(x) = e^{-iV\sin(2k_{\mathrm{L}}x)}$ with V the effective kick impulse. This state is not localized or time-reversal symmetric, and thus carries no expectation of showing a QBE. Surprisingly, experiments with the same protocol demonstrating QBE for the Bloch state also demonstrated QBE for this exotic state, but for different values of α (ie. in Fig. 4.9a. we show an example of a QBE at $\alpha = 0.89$, almost maximally far from the typical $\alpha = 0.5$). This exotic behavior is proven below using a Jacobi-Anger analysis similar to Section 3.1.3, and is fully explained in Appendix B of [48].

Using the Jacobi-Anger expansion for the initial wavefunction $\psi(x) = e^{-iV\sin x}$, we can decompose the initial kicked state in a discrete momentum basis indexed by integers l as

$$|\psi(t=0)\rangle = \sum_{l=-\infty}^{\infty} (-1)^l \mathcal{J}_l(V)\,|l\rangle\,, \tag{4.21}$$

where $\mathcal{J}_l$ is the l^{th} Bessel function of the first kind. The quarter-Talbot period free evolution is described by $e^{-ip^2/2\hbar}$ with $\hbar = \pi$ and $p = \hbar l$. Noting that $(-1)^l = (-1)^{l^2}$ we have

$$|\psi(t = T_{\mathrm{Talbot}}/4T)\rangle = \sum_{l=-\infty}^{\infty} i^{l^2} \mathcal{J}_l(V)\,|l\rangle\,. \tag{4.22}$$

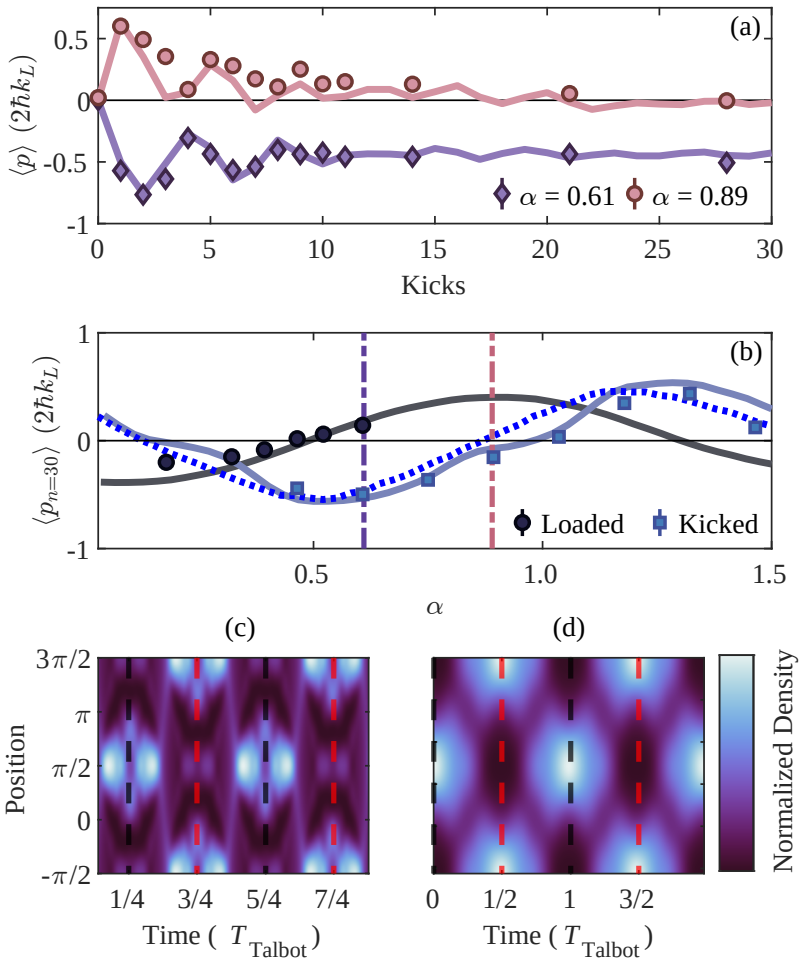

Fig. 4.9: Initial state dependence of the quantum boomerang effect. All error bars show standard error of the mean on repeated measurements. **(a):** Average momentum versus kick number for an initial state consisting of a BEC kicked once by a 60 E_{R} lattice. Pink circles correspond to $\alpha = 0.89$ and purple diamonds to $\alpha = 0.61$ for $T = 7\mu$s. Solid lines are predictions of TDSE numerics. bf(b): Average momentum after 30 kicks versus α, for an initial condition set by adiabatic loading of a BEC into a $7E_{\text{R}}$ lattice (grey circles) and an initial condition set by kicking a BEC once with a $60E_{\text{R}}$ lattice (blue squares). Dotted blue line shows infinite-time average momenta predicted by the Floquet diagonal ensemble (Eq. 4.8). Dashed vertical lines correspond to α values in (a). **(c-d):** Calculated density evolution over two Talbot times of a BEC kicked by a $60E_{\text{R}}$ lattice (left) and a a BEC adiabatically loaded into a $7E_{\text{R}}$ lattice which is then quenched off (right). Dashed vertical lines represent time-reversal symmetry axes.

The condition on the momentum coefficients for a time-reversal symmetric or real position-space wavefunction is $c^*_{-l} = c_l$, where $c_l = \langle l|\psi\rangle$. Using $\mathcal{J}_{-l}(V) = (-1)^l \mathcal{J}_l(V)$,

we straightforwardly confirm this condition

$$c^*_{-l} = (-i)^{(-l)^2}\mathcal{J}_{-l}(V) = i^{l^2}\mathcal{J}_l(V) = c_l. \tag{4.23}$$

This supports the claim that the kicked state should exhibit a boomerang effect for $\alpha = 1/2 + T_{\text{Talbot}}/4T$, which is what we observe in Fig. 4.9a. We note that this argument is only exact for 0 quasi-momentum, and the experimental kicked initial state data relies on a narrow quasi-momentum distribution about 0 for clear observation of the boomerang effect; however in considering corrections to this argument, one should keep in mind that the initial state (4.21) considered in this analysis is already only an approximate description of the experimental reality.

Intuitively, the time-reversal symmetry of the initial state can be evaluated by looking at the wavefunction probability distribution over time. Fig. 4.9c and d show single site TDSE simulations of a BEC kicked once with a 60 E_R lattice and a BEC loaded into a 7 E_R lattice which is quenched off at $T_{\text{Talbot}} = 0$, respectively. Time-reversal symmetric axes have been marked by vertical dashed red and black lines. These axes can be determined visually by finding time values where the entire plot is unchanged under y-axis reflection about those values. For the case of the kicked state (4.9c), we see that no time-reversal symmetric axis exists at $T = 0$, but after $1/4T_{\text{Talbot}}$ the state reaches the time-reversal symmetric axis marked by the first vertical dashed black line.

The final set of results I'll describe probes the question: what happens to quantum boomerang dynamics as localization is destroyed? In the QKR context, dynamical localization can be tunably disrupted by introducing temporal stochasticity into the kicking sequence [51,52]. To implement this, we add a deviation δ_n to the delay time after the n^{th} kick, where δ_n is randomly selected from a uniform distribution in the range $[-W/2, W/2]$. The parameter $\Delta = W/T$ quantifies the degree of randomness and can range from 0 to

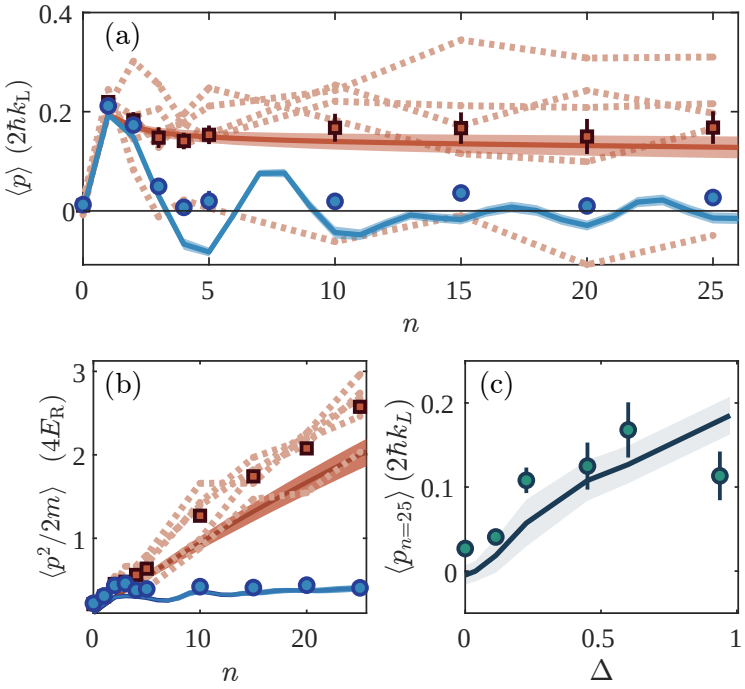

Fig. 4.10: Destruction of the quantum boomerang effect by stochastic kicking. All error bars correspond to the standard error of the mean for all realizations of randomness. **(a):** Average momentum measured after n kicks for temporal disorder strength $\Delta = 0$ (blue circles) and $\Delta = 0.6$ (red squares). For all data in this figure, $T = 8\mu$s, $\alpha = 0.52$, $V_0 = 41\,E_{\mathrm{R}}$, and the initial condition was set by an adiabatic lattice load to $8\,E_{\mathrm{R}}$. Circles (squares) represent the mean of measurements with 5 separate kick disorder realizations for $\Delta = 0$ ($\Delta = 0.6$). Dashed lines show individual realizations. Shaded areas in (a) and (c) show numerically calculated $\langle p \rangle \pm \sigma_{\langle p \rangle}$ with 9000 disorder realizations and 500 initial quasimomenta. The shaded area in (b) includes an additional estimate of the energy accounting for the statistical error in the lattice depth of $V_0 = 41 \pm 2\,E_{\mathrm{R}}$ over 500 lattice depths and 500 realizations. **(b):** Measured mean energy for $\Delta = 0$ (blue circles) and $\Delta = 0.6$ (red squares) over 10 points (blue) and 5 disorder realizations (red), illustrating the destruction of dynamical localization by random kicking. **(c):** Average momentum $\langle p \rangle$ after 25 kicks versus disorder strength Δ. Dots are averages over 10 disorder realizations, except for $\Delta = 0, 0.6$ (5 realizations each). The solid line is numerically calculated $\langle p \rangle$ over 9000 disorder realizations, with shaded area showing a one-standard-deviation range.

1. Fig. 4.10a shows the time evolution of average momentum for $\Delta = 0$ (no randomness) and $\Delta = 0.6$, with the first kick fixed so that $\alpha = 0.52$, and with the same experimental parameters as in Fig. 4.8b. In contrast to the characteristic boomerang-like evolution when $\Delta = 0$, each of the five experimental realizations of randomness for $\Delta = 0.6$ exhibits

a different behavior. The mean momentum over these disorder realizations demonstrates the destruction of the quantum boomerang effect, with a long-time average momentum significantly different from zero, and agrees reasonably well with the result of disorder-averaged simulations. Fig. 4.10b shows the evolution of the average energy for the same experiments: the destruction of dynamical localization by random kicking and the approach to classical linear-time energy growth are clearly visible in both experiment and theory, and are associated with the destruction of the quantum boomerang effect in Fig. 4.10a. To directly probe the dependence of the quantum boomerang on the disorder strength, we plot in Fig. 4.10c the disorder-averaged mean momentum after 25 kicks as a function of Δ. Measured long-time $\langle p \rangle$ increases monotonically up to $\Delta \approx 0.5$ and agrees reasonably well with disorder-averaged numerical predictions. An interesting topic for further study is the relationship between the degree of destruction of the boomerang effect (measured, for example, by long-time average momentum) and the exponent characterizing energy growth [53–55].

4.4 Conclusions

In this work we have presented the first experimental evidence for the quantum boomerang effect in an Anderson-localized system. The measurements confirm theoretical predictions [29, 49] and demonstrate that boomerang dynamics can occur from a variety of initial conditions including even a homogeneous density distribution. These experimental results, along with the analytical theory we present in the appendices, elucidate the crucial role of parity and time-reversal symmetry in determining the presence or absence of the quantum boomerang effect. We have probed the dependence of boomerang dynamics upon Anderson localization itself by measuring the effect of tunably random kicking sequences: results confirm that classical diffusion induced by

stochasticity destroys both dynamical localization and the quantum boomerang effect. These experiments validate a new, powerful probe of the uniquely quantum-mechanical nature of localization applicable to a general class of disordered systems and suggest a variety of intriguing topics for future exploration. These include boomerang phenomena in higher-dimensional systems, different symmetry classes [56], more exotic initial states, and the presence or absence of many-body boomerang effects in interacting systems [57] or even many-body localized states. Applications of our demonstration that adjusting the Floquet gauge can switch on or off the boomerang effect are an intriguing possibility. Beyond the context of the quantum kicked rotor, the investigation of boomerang-like phenomena in condensed matter systems and implications of these results for ultrafast electron dynamics in disordered solids represent unexplored frontiers.

Since the publication of our manuscript [48], more theoretical work has been published exploring the QBE in systems with different symmetries [58], with many-body interactions [59], and in Hermitian vs. non-Hermitian systems [60, 61].

Chapter 5

Quantum Thermodynamic Engines

5.1 Background and Theory

Since the industrial revolution, engines have been powering the activities of humanity. The steam engine, first commercially used to drive water pumps circa the 17th century, began an adoption of engines as a global energy conversion phenomenon that has persisted to this day. This technology is purely powered by 19th century classical thermodynamics, yet accounts for roughly 75% of the world's electricity production. Due to their profound importance, heat engines continue to be an active research area, with recent interest in miniature versions at the micro and nano-scale. In the past decade, the capabilities of quantum thermodynamic engines have been explored theoretically [62, 63, 63–81], and recent years have seen experimental demonstrations of both quantum and nanoscopic classical engines using single ions [82,83], nuclear spins [84], cold atoms [85–88], nitrogen-vacancy centers [89], and quantum gases [90,91]. A natural question is whether quantum phenomena can enhance the performance of a thermodynamic engine [92–94]. Perhaps the simplest experimental approach to this question — the direct comparison of an engine using a classical working fluid to an equivalent one using a quantum degenerate working

fluid — has remained unexplored.

Amid the initial work on quantum thermodynamic engines, some attention focused on creating macroscopic quantum engines with large ensembles of particles. One of these ideas is the Feshbach engine, a novel scheme utilizing the temporal control of interactions between atoms in a quantum gas as part of a thermodynamic cycle [95]. The scheme subjects a BEC to alternating strokes of heat transfer and interaction strength variation. The heat transfer is theoretically performed by the addition and removal of particles or energy to and from the condensate, while the interactions can be controlled via the Feshbach resonance. While not entirely analogous to our system, this pioneering work first showed that BECs can be used as a unique working fluid for thermodynamic engines. In our experimental setup, the coherent addition and removal of particles and/or energy is challenging as our BEC is not coupled to any reservoirs. However, another parameter which is easily controlled is the trap frequency, and in alternating strokes of varying interactions and varying trap frequency we are able to create a new type of quantum thermodynamic engine. For the remainder of this chapter, I'll discuss the experimental setup to create this type of engine, along with experimental results showing the engine's work output and optimization of power and efficiency. At the end, I'll explore how this engine is analagous to an Otto cycle through a reframing of parameters.

5.2 Experimental Setup

The experiments begin by preparing a BEC of between 300,000 and 1 million atoms. It's worth noting that since putting in the Azurlight 130W Fiber amplifier as the dipole trapping laser source, the size of the BECs have increased by almost an order of magnitude, and potentially hold the record for the largest ^{7}Li BECs made to date. After the final stage of evaporative cooling, the BEC resides in a crossed optical dipole trap with a

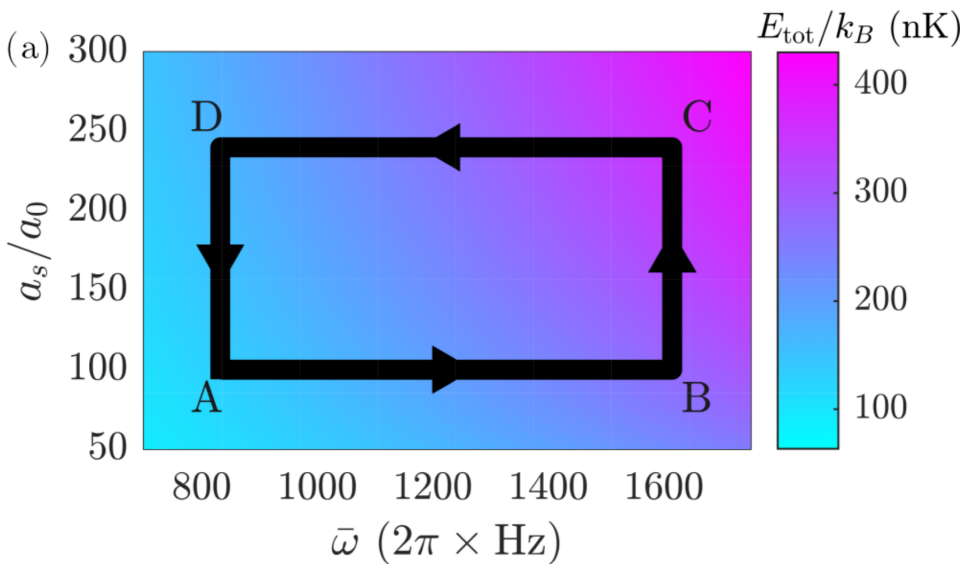

Fig. 5.1: Varying steps in interaction strength (a_s) and trap frequency ($\bar{\omega}$) space to create a thermodynamic engine cycle. The background color shows the total energy per particle in the BEC. The values shown are typical for the cycles that will be discussed in this chapter.

geometric mean trap frequency of $\bar{\omega} = 2\pi \times 130$ Hz, at a temperature of approximately 170 nK, implying a condensate fraction of 95 percent. The scattering length is then tuned to $100a_0$, which is the starting point for all of the following experiments described.

To begin the thermodynamic cycle, an example of which is shown in Fig. 5.1, the ODT is ramped such that $\bar{\omega}$ increases at a constant linear rate while maintaining adiabaticity (which will be proven later in the chapter). This acts as the compression stroke of our engine (steps A to B). In the next stroke, we hold the trap frequency constant and ramp the magnetic field such that the s-wave scattering length increases at a linear rate while maintaining adiabaticity (steps B to C). This stroke is in a sense analagous to the combustion stroke of an Otto cycle, in that both increase "pressure". The definition of "pressure" in this case will be proven at the end of the next section.

Following the second stroke, we linearly ramp down the trap frequency back to its initial value, completing the expansion stroke (steps C to D). This stroke is where the

additional energy pumped into the working fluid is transferred to the optical field, because the work performed on an optical field by a strongly interacting gas is larger than the work needed to compress a more weakly interacting gas. We then ramp the magnetic field back to its initial value, completing the thermodynamic cycle and leaving the working fluid in the same state in which it started (steps D to A).

To characterize the thermodynamic cycle created by the engine, we turn off the trap after each stroke and allow the atoms to undergo a free expansion. As soon as the trap is turned off, the potential energy disappears and the energy remaining in the BEC is comprised of both interaction and kinetic energies. As the atoms fall freely, the interaction energy is converted to kinetic energy via interatomic collisions, and after sufficient time essentially all energy remaining in the system is kinetic. Once all the energy has been converted, we perform absorption imaging to reconstruct the momentum distribution of the atoms. Following [96], we can convert the imaged distribution to a kinetic energy measurement via the formula:

$$E_{rel} = \frac{3\pi m}{2\sigma_0 t_{TOF}^2} \int \rho^3 \log(\frac{I_0}{I}) d\rho \tag{5.1}$$

where m is the mass of a ^{7}Li atom,t_{TOF} is the time of flight duration, I_0 is the intensity of the beam before absorption by the atoms, ρ is the radial coordinate in the image, and $\sigma_0 = 3\lambda^2/2\pi$ with λ the resonant wavelength. The above formula gives a measurement of the release energy:

$$E_{rel} = E_{int} + E_k \tag{5.2}$$

This can be compared to the theoretical prediction of the release energy for a BEC

in the Thomas-Fermi limit [7]:

$$\frac{E_{\text{rel}}}{N_c k_B T_c^0} = \frac{3\zeta(4)}{2\zeta(3)} t^4 + \alpha \frac{1}{7} \left((1 - t^3)^{2/5} (2 + \frac{17}{2} t^3) \right) \tag{5.3}$$

where $t = T/T_c^0$ and $\alpha = \mu/k_B T_c^0$. T_c^0 represents the critical temperature for noninteracting particles.

5.2.1 Ramp Linearization

While the initial versions of this experiment were performed with linear voltage ramps in Cicero for both the dipole trap and magnets, we later switched such that both trap frequencies and interaction strength were ramped linearly. This can be achieved simply by setting both ω and a to constants times time, and then inverting their respective equations to achieve a voltage time series that can be input to Cicero. The constants represent the ramp rate, which we choose empirically such that the ramps are adiabatic.

To create the ramp waveform for the interaction strength, we start with the equation for the scattering length as a function of the magnetic field around the Feshbach resonance:

$$a(B) = a_{bg}(1 - \frac{\Delta}{B - B_0}) \tag{5.4}$$

where $a_{bg} = -24.5$, $\Delta = -192.3$, and the location of the Feshbach resonance $B_0 = 736.8$G for ^{7}Li. The magnetic field B at the location of the atoms is linearly proportional to the current in the coils due to the Helmholtz configuration, and the current in the coils is linearly proportional to the voltage sent to the PTEN current supply from Cicero, which is the main control knob. The desire is to create a voltage waveform in Cicero that will generate a linear s-wave scattering length ramp with respect to time at the

atoms, with a tunable ramp rate for adiabaticity testing. The field ramps at a constant 1.72 G/A with increasing current from the PTEN, determined from ex-situ testing. The PTEN outputs 50A per V input from Cicero, so the magnetic field at the atoms is linear with the Cicero voltage, via the relationship $B(V_{Cicero}) = 1.72\ \mathrm{G/A}\ *\ 50\ \mathrm{A/V} * V_{Cicero} = 86\ \mathrm{G/V} * V_{Cicero} = c_{bv} V_{Cicero}$. Eq. 5.4 can be parametrized as

$$\begin{aligned} a(t) = \dot{a}t + a(0) &= a_{bg}(1 - \frac{\Delta}{B(t) - B_0}) \\ &= a_{bg}(1 - \frac{\Delta}{c_{bv}(V(t) - V_0)}) \end{aligned} \tag{5.5}$$

where $\dot{a}$ is the desired interaction ramp rate and V_0 is the voltage corresponding to the magnetic field at the Feshbach resonance. To obtain the desired waveform, Eq. 5.5 is inverted to

$$V(t) = V_0 + \frac{\Delta}{c_{bv}(1 - \frac{\dot{a}t + a(0)}{a_{bg}})} \tag{5.6}$$

which can be put into Cicero.

Similarly, a waveform can be created for linear ramping of the trap frequency. The expression for the radial trap frequency for a dipole trap beam is

$$f_r = \frac{1}{2\pi}\sqrt{\frac{4U_0}{m w_0^2}} \tag{5.7}$$

where U_0 is the maximum trap depth and w_0 is the beam waist at the focus. U_0 is proportional to the intensity $I(\mathbf{r})$, which is controlled by the RF power sent to the lattice AOM. To a good approximation, $I(t) \propto V_l(t)$, where $V_l(t)$ is the voltage sent from Cicero

to the AM input of the Moglabs RF driver, which controls the RF power amplitude. This is the main control knob for which we desire a waveform that will ramp $\omega(t)$ linearly. From the above relations, $V_l(t) \propto f_r^2$, and thus can be modeled as a general quadratic $V_l(t) = af_r^2(t) + bf_r(t) + c$. The initial and final voltages are set by the initial trap at the end of evaporation as well as the desired compression ratio, providing two constraints. The final constraint is provided by the ramp rate $\dot{V}$, which we decide after adiabatic analysis (discussed in the Results section). Thus, the functional form of $V_l(t)$ can be solved completely.

5.2.2 Trap frequency measurements

A crucial control parameter in this experiment is the trap frequency of the crossed ODT the atoms reside in, and thus accurate measurement of the trap frequency is important. To achieve this, we ramp the trap to a specific laser power and excite a small oscillation. Physically, after ramping the trap, we slowly translate one beam for 10ms before snapping it back to its original position, holding the other beam stationary. This creates a position displacement for the atoms away from the intensity maxima, causing them to slosh about the trap zero position. The frequency of sloshing will occur at the radial trap frequency of the displaced beam. The procedure is then swapped for the two beams to measure the frequency of the other beam. The ODT beams can be dithered by frequency modulating (FM) the Siglent AWG generating the RF for the ODT AOMs, which in turn creates position displacement at the atoms. By setting a low frequency for the FM ($<<$ 100 Hz), the 10 ms displacement can be controlled by sending a voltage signal to the AM input of a second Siglent AWG, whose output is the FM input for the Siglent AWG controlling the AOMs.

Example data from a slosh measurement is shown in Fig. 5.2. For accurate mea-

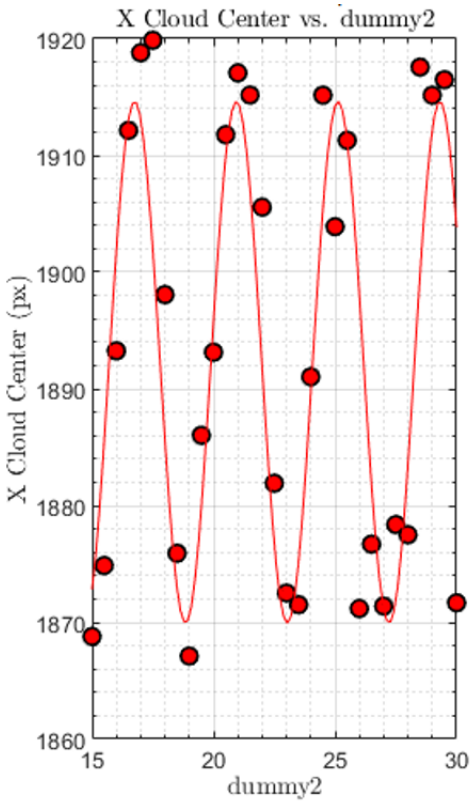

Fig. 5.2: Trap frequency slosh measurement. The dummy2 variable represents time in ms. The X oscillation frequency is 239 Hz, corresponding to an ODT beam ramped to 20% of its maximum power.

surements, we've found it best to sample around 8-10 points per period for at least 3 periods.

5.2.3 Scale factors and TOF analysis

A critical feature of this cold atom experiment is the 3D nature of the BEC. When collecting data for this experiment, one initial oversight was the lack of measuring the vertical positions of our atoms. Since absorption imaging only gives a 2D projection of atomic distribution, we fail to measure high energy atoms with dominant vertical velocities after the free expansion protocol. To address this, the 3D distribution was initially reconstructed from the 2D projection via an inverse Abel transform, an integral

transform method used for reconstruction of spherical or axially symmetric distributions. The Abel transform of a function f(r) is given by

$$F(y) = 2\int_y^\infty \frac{f(r)rdr}{\sqrt{r^2 - y^2}}, \tag{5.8}$$

which projects $f(r)$ onto a plane. The inverse Abel transform is given by

$$f(r) = -\frac{1}{\pi}\int_r^\infty \frac{dF}{dy}\frac{dy}{\sqrt{y^2 - r^2}}, \tag{5.9}$$

and in our case the images we obtain from absorption yield $F(y)$. In practice, we found that using an inverse Abel transform directly on our imaged distributions led to poor agreement with Eq. 5.3 due to inhomogeneous scaling of the cloud as the atoms freely expand. This is due to non-sphericity in the ODT as well as lensing from residual magnetic field curvature during the free expansion. Thus, the imaged distribution doesn't obey the radial symmetry condition necessary for the Abel transform. To bypass this, we imaged the atomic cloud from both the top and the side to obtain length scales for each axis, $\bar{x}, \bar{y}, \bar{z}$. These length scales are radii obtained from Gaussian fits to the imaged distributions, though fits to Thomas-Fermi profiles obtain similar results. The absorption image from the vertical axis (yielding an atomic distribution in the x and y axes) is taken and scaled in the y-axis coordinate by $\bar{y}/\bar{x}$ to create a circular distribution, and an inverse Abel transform via Eq. 5.9 is applied. The result of this transform is a 3D radial distribution in scaled coordinates referenced to the x-axis. Reverting back to Cartesian coordinates simply requires the multiplication of $\bar{y}/\bar{x}$ in the y-coordinate and $\bar{z}/\bar{x}$ in the z-coordinate.

If imaging from multiple axes is not possible, an alternative method to obtain scale

factors is available via free expansion simulation. In [97], a full treatment is given to the dynamics of a BEC released from a trapping potential. Assuming the BEC starts with initial Thomas-Fermi radii $R_j(t=0), (j=1,2,3)$ for the three spatial coordinates, the cloud will experience dilation according to

$$R_j(t) = \lambda_j(t) R_j(0), \tag{5.10}$$

where $\lambda_j(t)$ is a time-dependent scale factor. Applying Newton's law to the evolution of the spatial density and assuming a 3D harmonic trap for the potential, the evolution of the scale factors can be determined from the set of coupled equations

$$\ddot{\lambda}_j = \frac{\omega_j^2(0)}{\lambda_j \lambda_1 \lambda_2 \lambda_3} - \omega_j^2(t)\lambda_j \quad (j=1,2,3). \tag{5.11}$$

When the potential is turned off (ie. for a TOF), the second term on the right hand side disappears. Interestingly, the resulting set of equations implies that the full dynamics of the TOF are governed only by the scale factor evolution. This set is straightforward to solve computationally, and can describe many characteristics of BECs, such as the inversion of their aspects ratios when released from an asymmetric trap [98]. Example MATLAB code to solve these equations is provided below.

```
syms bx(t) by(t) bz(t)
ode1=diff(bx,2) == ((wX^2/(bx^2*by*bz)));
ode2=diff(by,2) == (wY^2/(bx*by^2*bz));
ode3=diff(bz,2) == (wZ^2/(bx*by*bz^2));
```

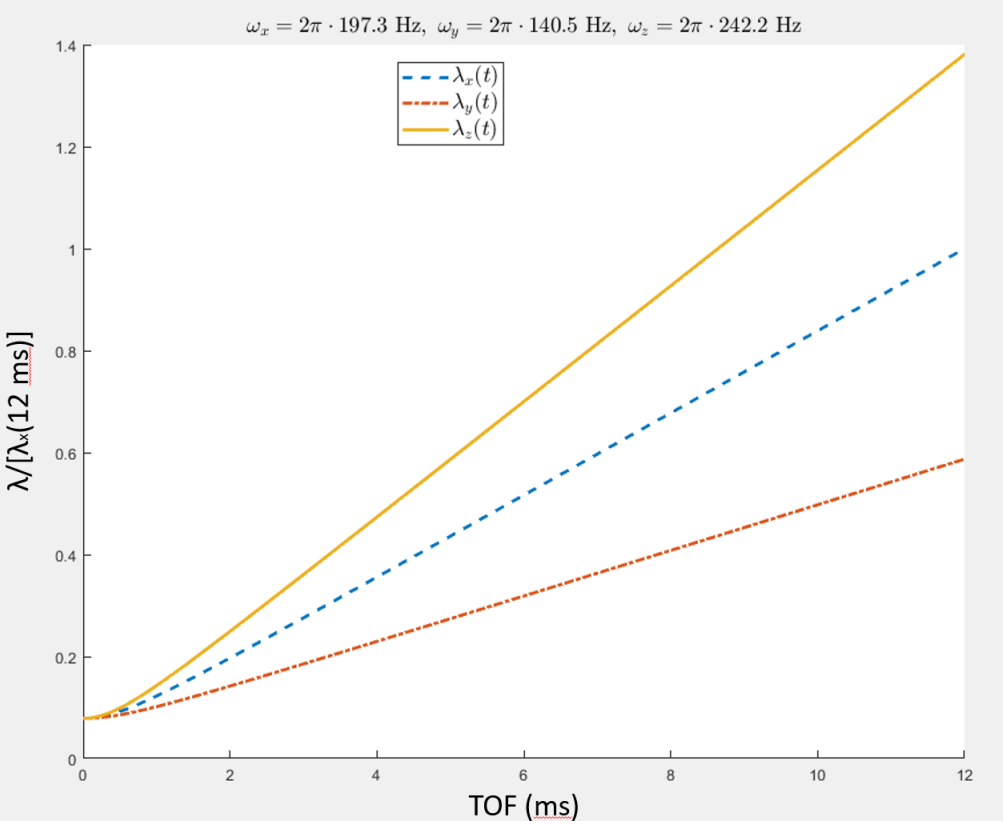

Fig. 5.3: Scale factor evolution for typical trap frequencies used in the experiment, computed by solving the coupled equations 5.11. The y-axis has been scaled by the x-scale factor at the end of the TOF.

```
interval = [t0 tf];  %time interval

vars = [bx(t); by(t); bz(t)];

[V] = odeToVectorField([ode1,ode2,ode3]);

M = matlabFunction(V,'vars', {'t','Y'});


opts = odeset('RelTol',1e-7,'AbsTol',1e-9);

y0 = [1,0,1,0,1,0];

ySol = ode45(M,interval,y0,opts);
```

5.3 Creating a Quantum Thermodynamic Engine

The following section will discuss the results of various experiments performed with the quantum thermodynamic engine. These results have been published in [99].

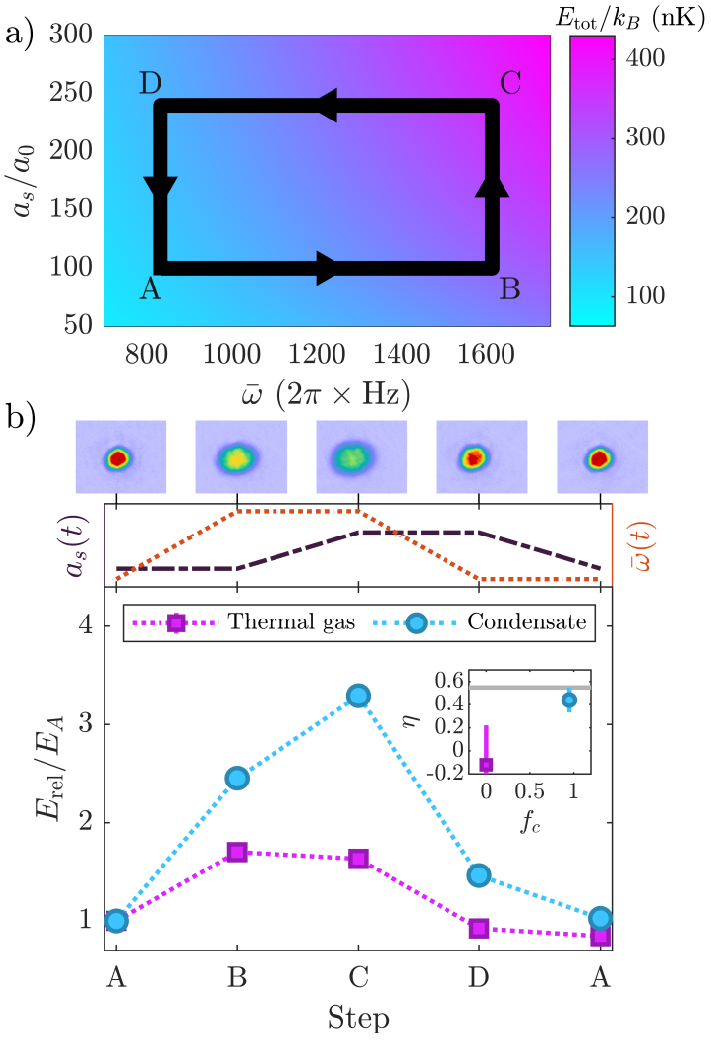

Fig. 5.4: Thermodynamic engine with a quantum degenerate working fluid. (a) Engine cycle in a_s-$\bar{\omega}$ space. Color shows total energy per particle. (b) Top: BEC images after 12 ms of expansion at each step. Middle: Evolution of trap frequency (dotted) and scattering length (dot-dashed). Bottom: measured release energies for quantum degenerate (circles) and thermal (squares) working fluids during one engine cycle, normalized by the step A value. Dotted lines connect data points. Inset shows efficiency for each condensate fraction f_c; line indicates theoretical maximum efficiency in the Thomas-Fermi regime. Error bars show standard error in all figures.

Before we begin, there are two metrics that must be defined which characterize any engine: efficiency and power, designated by η and P respectively. η is defined as

$$\eta = \frac{E_{\mathrm{CD}} - E_{\mathrm{AB}}}{E_{\mathrm{BC}}}. \tag{5.12}$$

Here the numerator is the difference between energy lost and energy gained by the working fluid from the dipole trap ramps, and the denominator is the energy gained during the first magnetic ramp. The numerator equates to the amount of magnetic energy carried away by the optical trap, and thus η represents the converted fraction of the magnetic energy inputted into the system. P is defined as:

$$P = \frac{E_{\mathrm{CD}} - E_{\mathrm{AB}}}{T_{cycle}}, \tag{5.13}$$

which is a measure of how fast magnetic energy can be delivered to the optical trap.

The initial goal of the experiment was to identify any advantage from having a quantum degenerate gas as the working fluid in a thermodynamic engine. The Bose-condensed working fluid is compared to a classical one by performing analagous engine cycles on a BEC and a classical gas. This is achieved by preparing a thermal gas via low-interaction optical evaporation. We ramp our scattering length to 57a0 before ramping down the ODTs, resulting in inefficient evaporation due to choked rethermalization, producing a non-condensed cloud at the end of the evaporation sequence. Due to the partial evaporation, the thermal gas starts at a larger initial trap frequency than the condensate, but both fluids experience the same compression ratio $\nu = \bar{\omega}_B/\bar{\omega}_A \approx 2$ during the optical ramps. This thermal gas has a temperature of 890 nK with a density of $6\text{x}10^{11}$ atoms/cm^3, about 33 times less than the condensate. The density difference can be attributed to bosonic quantum statistics, with the Thomas-Fermi profile having a larger

concentration of atoms when compared to a thermal gas. The difference in engine performance can be seen in Fig. 5.4b. While both fluids increase and decrease energy during optical compression and decompression (steps A to B and C to D, respectively), the condensed working fluid experiences a large change in energy during the interaction ramps (steps B to C and D to A) while the thermal gas energy remains constant within measured error. In terms of engine performance the two fluids produce a stark contrast in η, where the thermal gas has 0 efficiency and thus no ability to transfer energy. The BEC has an efficiency closer to 50% for a wide parameter range (with more specific values given in the discussion of compression ratios), transferring about half of the energy inputted by the magnets into the optical fields. The difference in behavior can be attributed to the Bose-enhanced density of the condensate, which drastically increases the interaction energy in the cloud compared to the low density thermal cloud.

It is useful to measure the reversibility and repeatability of the engine cycle. Reversibility allows for energy transfer in the opposite direction, from the optical field to the magnetic field, and repeatability guarantees the ability to transfer energy for large time scales. Reversibility can be tested by running the engine cycle in reverse (A-D-C-B-A) and comparing the release energy of the working fluid per step to the forward cycle. In Fig. 5.5a, the result of this comparison is shown. The large amount of overlap demonstrates a high degree of reversibility as well as the ability to transfer energy from the lasers to the magnets. Repeatability can be tested simply by running the engine cycle multiple times. Fig. 5.5b shows the release energy per step over 4 cycles. The black line shows theoretical results of isentropic interacting numerical simulations detailed in Appendix A of [99]. The working fluid reliably returns to its original release energy after the completion of each cycle, showing no significant absorption of energy during the course of the cycle. However, there is a reduction of release energy gain per cycle, as shown by the decreasing heights of the step B energy in each cycle. This is attributed to

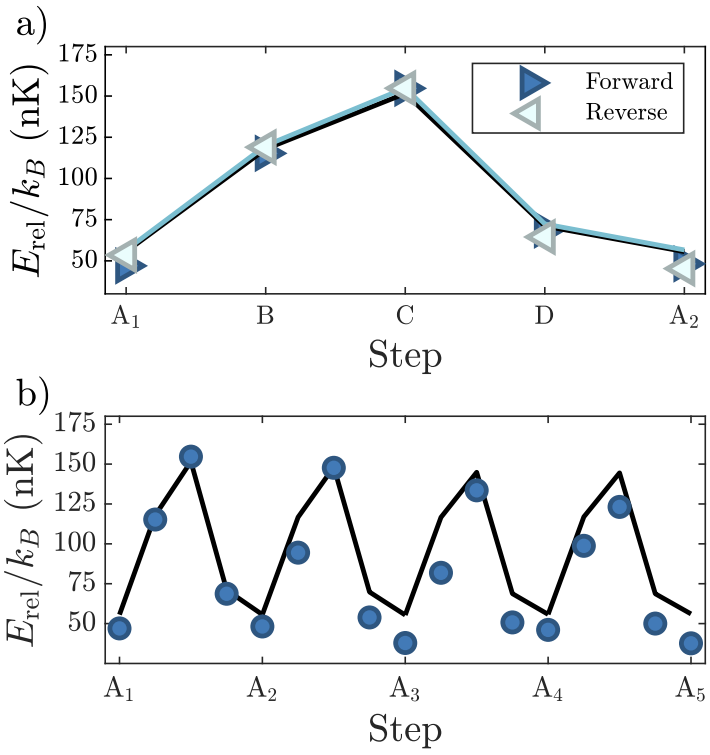

Fig. 5.5: Engine reversibility and repeatability. (a): Comparison of the cycle performed in the "forward" (*A*-*B*-*C*-*D*-*A*) and "reverse" (*A*-*D*-*C*-*B*-*A*) directions, indicated by right- and left-pointing markers respectively. Light blue line shows results of analytic calculations (see Eq. 5.3); black line shows results of isentropic fully-interacting numerical simulations in both panels. (b): Measured release energy evolution during four repeated engine cycles. Simulation particle number is set to the mean particle number across each four-step cycle. Error bars are smaller than symbol size.

three-body loss of atoms during the duration of the experiment, which lasts 530 ms per cycle. Measuring the atom number each cycle, we find $\sim 20\%$ reduction in atom number from the first to the second cycle, 13% reduction from the second to the third cycle, and a 7% decrease from the third to the fourth cycle for this parameter set. The monotonic decrease can be intuited from the fact that three body loss decreases as the cloud density decreases [100], and qualitatively matches our expectations for the scattering lengths used in the cycle. These loss numbers will vary with respect to atom number, trapping frequencies, and interaction strengths, but will always inherently limit the repeatability

of the engine.

Efficiency and power are arguably the two most important metrics for engine performance, and both depend on the adiabaticity of the cycle. The adiabaticity can be tested by varying the cycle time and observing if η and P deviate from theoretical predictions. This is critical, as adiabaticity prevents excessive heating and loss of atoms from the trap, and allows for appropriate characterization of the energy during the cycle. As an estimate, we apply the Landau-Zener formalism to approximate the probability of excitations [101, 102].

Considering only the ground state and the first excitation, the probability of a Landau-Zener transition between them is

$$\begin{aligned} \mathrm{P} &= e^{-\frac{1}{\Theta}}, \\ \Theta &= \frac{\dot{\omega_E}}{2\pi\omega_E^2} \end{aligned} \tag{5.14}$$

where Θ is the adiabaticity parameter and $\bar{h}\omega_E$ is the energy gap to the first excited state. Θ is straightforward to compute, as the energy gap corresponds to the first excitation in the 3D ODT harmonic trap, and $\dot{\omega}_E$ is a tunable parameter set by the trap ramp speed. For the data in Fig 5.4 and 5.5, $\dot{\omega} = 2\pi$ Hz/ms, corresponding to a maximum $\Theta \sim .001$ and obeying the adiabaticity criterion of $\Theta << 1$. In Fig. 5.6b, the inset show how adiabaticity changes as a function of the cycle time. While there is significant increase as the cycle time becomes shorter, Θ remains well under 1 for all tested cycle times.

Fig. 5.6 shows the efficiency and power with respect to the total cycle time. The gray line in Fig. 5.6a corresponds to the theoretical Thomas-Fermi efficiency computed by inputting Eq. 5.3 into Eq. 5.12, which is independent of cycle time. The data in

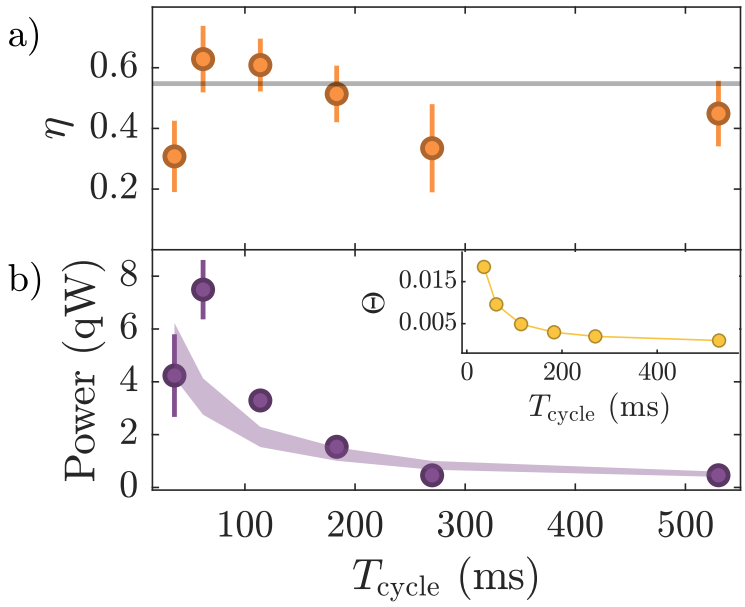

Fig. 5.6: Efficiency and power vs. cycle time. (a): Measured energy transfer efficiency η versus cycle time. Line shows theoretical efficiency from Eq. 5.3. (b): Measured engine power, quoted in quectoWatts (10^{-30} Watts), versus cycle time. Shaded region shows the theoretical prediction of Eq. 5.3 for the measured range of atom numbers. The power shown here is taken from release energy measurements; as discussed in the main text, the total power is a factor of 2.5 higher. Inset shows adiabaticity parameter Θ versus cycle time.

Fig. 5.6a cluster around this theoretical value, though the drop at larger cycle times is attributed to three-body loss and heating of the atoms. At short times, technical limitations, including inductive limits on the magnet ramp rate, degrade the efficiency. Similar behavior can be seen in Fig 5.6b for the power, which decreases according to Eq. 5.3 (purple shaded region in plot, whose width corresponds to the range predicted by the typical variation in atom number), though with significant deviation at lower cycle times. Again there is a drop-off at the shortest cycle time due to the aforementioned technical limitations. The difference between the theoretical prediction and data point around 50 ms can be attributed to the inability of the dipole trap beam powers to follow their PID setpoints, which led to increase excitations in the BEC.

These results conform to expectations from our experience of macroscopic heat engines, in that there is a balance between power and efficiency, but also an optimal range of engine speeds. However, there is a growing body of work on methods to circumvent this tradeoff with shortcuts to adiabaticity (STA) [95, 103, 104]. This concept will be explored in the final section of this chapter 5.5.1.

To maximize the performance of the engine, it's worth looking at the theoretical efficiency to determine which parameters are relevant [1]. The trap compression ratio and interaction ratio are defined as $\nu := \bar{\omega}^B/\bar{\omega}^A$ and $\kappa = a_s^C/a_s^A$, respectively. Assuming that the BEC starts in the ground state of the harmonic trap and has negligible kinetic energy, the Thomas-Fermi formalism can be applied. The BEC energy exhibits the following scaling dependencies [102]:

$$E/N \propto \left(\frac{Na_s}{\bar{a}_{\mathrm{HO}}}\right)^{2/5} \hbar\bar{\omega} \propto a_s^{2/5}\bar{\omega}^{6/5}. \tag{5.15}$$

The above can be applied to the energy at each step of the thermodynamic cycle:

$$E_{\mathrm{AB}} \propto (\nu^{6/5} - 1)\, a_s^{2/5}\bar{\omega}^{6/5}, \tag{5.16}$$

$$E_{\mathrm{BC}} \propto \nu^{6/5}(\kappa^{2/5} - 1)\, a_s^{2/5}\bar{\omega}^{6/5}, \tag{5.17}$$

$$E_{\mathrm{CD}} \propto \kappa^{2/5}(\nu^{6/5} - 1)\, a_s^{2/5}\bar{\omega}^{6/5}. \tag{5.18}$$

The efficiency can then be written as

[1] Credit to Yifei Bai for helping to solve this

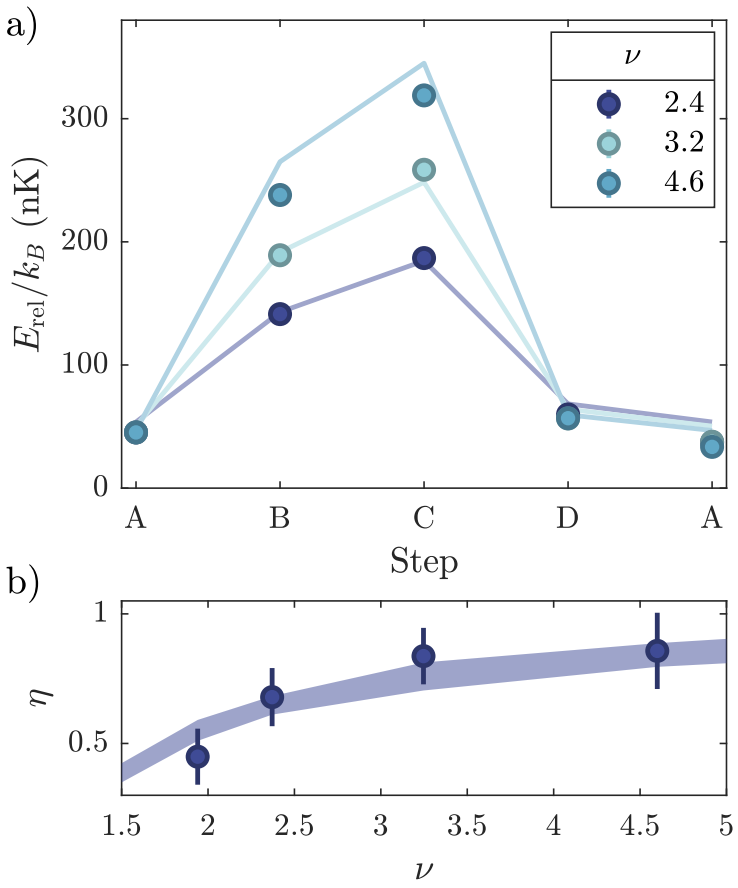

Fig. 5.7: Effects on engine performance from varying compression ratio. (a): Measured release energy evolution over one engine cycle for varying $\nu = \bar{\omega}_B/\bar{\omega}_A$ at a fixed interaction ratio $\kappa = a_s^C/a_s^A = 2.4$. Lines show analytical prediction of Eq. 5.3. (b): Efficiency η as a function of compression ratio. Shaded region shows theoretical prediction of Eq. 5.19 for the measured range of atom numbers.

$$\begin{aligned} \hookrightarrow \eta &= \frac{E_{\mathrm{CD}} - E_{\mathrm{AB}}}{E_{\mathrm{BC}}} = \frac{\kappa^{2/5}(\nu^{6/5}-1) - (\nu^{6/5}-1)}{\nu^{6/5}(\kappa^{2/5}-1)} = \frac{\nu^{6/5}-1}{\nu^{6/5}}\frac{\kappa^{2/5}-1}{\kappa^{2/5}-1} \\ &= \frac{\nu^{6/5}-1}{\nu^{6/5}} = 1-\nu^{-6/5} = 1-\left(\frac{\bar{\omega}^A}{\bar{\omega}^B}\right)^{6/5}. \end{aligned} \tag{5.19}$$

Surprisingly, the efficiency is solely determined by the compression ratio ν. This can be compared in analogy to the Otto cycle efficiency $\eta_{\mathrm{Otto}} = 1-\nu^{1-\gamma}$ with ν the

compression ratio and γ the specific heat ratio. Fig. 5.7a shows three thermodynamic cycles with varying ν, with distinctly larger release energies at steps B and C and no significant change in steps A and D, in agreement with 5.3. In Fig. 5.7b, an asymptotic increase towards unit efficiency is shown with increasing ν. Excellent agreement is observed between the data and Eq. 5.19 (shown by the shaded purple region), validating the predicted relationship between η and ν.

Similarly, we can look at the effects of the interaction strength by looking at power as a function of κ while holding ν constant. Using Eq. 5.19, $P \propto (\kappa^{2/5} - 1)(\nu^{6/5} - 1)$: the power is determined solely by the interaction ratio κ for a fixed compression ratio ν. Fig. 5.8a examines three cycles with varying κ (1.2,1.6,2.0). Accessing larger κ remains an experimental challenge due to significant three-body loss over the duration of the cycle, while smaller interaction strengths are more experimentally accessible but depart from the Thomas-Fermi regime, making comparison to theory challenging. Fig. 5.8b shows that the output power indeed increases with κ, with a departure from theoretical predictions at larger values of κ a possible hint of beyond-mean-field behavior. These results emphasize the importance of interaction effects in the engine: Feshbach tuning is the key parameter controlling energy transfer between magnetic and optical fields. This power enhancement is completely decoupled from the boost to efficiency achieved through stronger compression, and from the power enhancement due to decreased cycle time. Taken together, ν and κ represent flexible experimental control knobs which enable a quantum gas to execute efficient and tunable energy transfer between two otherwise decoupled reservoirs of energy.

We've now fully characterized this novel quantum thermodynamic engine. It's helpful to frame the results within the context of existing engines. Here we draw an analogy between this isentropic thermodynamic cycle and the classical Otto cycle, following Appendix B in [99]. Because the walls of the trap are not rigid and the optical trap interacts

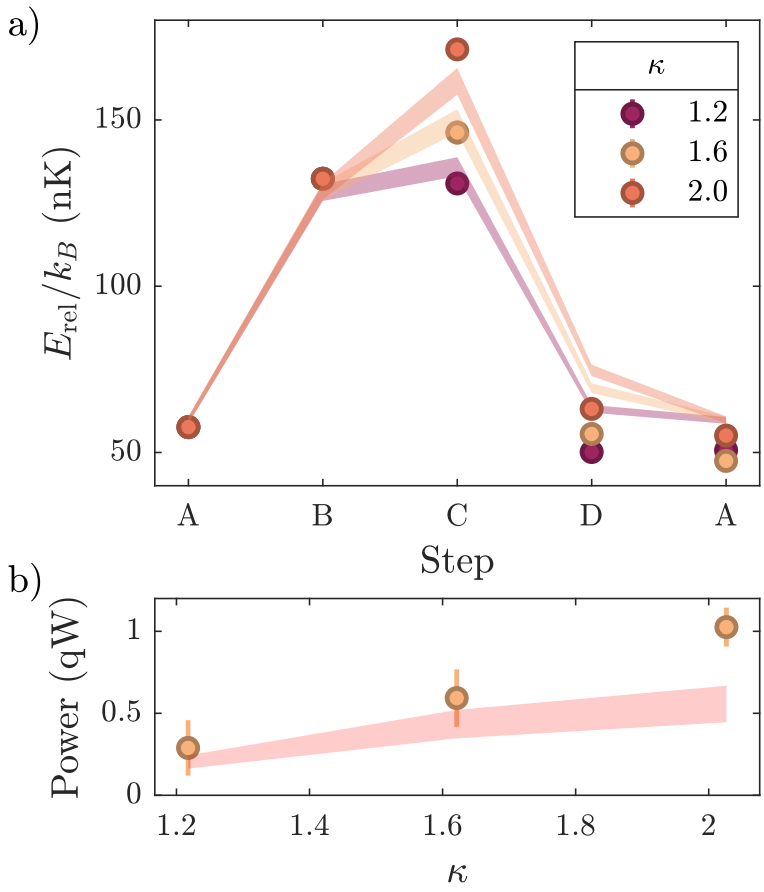

Fig. 5.8: Effects on engine performance from varying interaction strength ratio. (a): Measured release energy evolution over one engine cycle for varying interaction strength ratio $\kappa = a_s^C/a_s^A$ at a fixed compression ratio $\nu = 1.94$. (b): Power output as a function of κ. Shaded regions in both panels are theoretical predictions from Eq. 5.3 for the measured range of atom numbers.

with the BEC at all spatial positions $\mathbf{r}$ through the single-body term $U_{\mathrm{ext}}(\mathbf{r})$, thermodynamic pressure and volume are understood differently than their analogues for fluids in rigid containers. The proper pressure to use in thermodynamic relationships is a generalized extensive mechanical variable related to the spatial extent of the gas $\mathcal{V} = (\hbar\bar{\omega})^{-3}$, referred to as "harmonic volume" [105–107]. We can write the total energy in terms of

this thermodynamic volume as

$$E = \frac{5}{7}\frac{15^{2/5}}{2} m^{1/5} N \left(\frac{N a_s}{\hbar \mathcal{V}}\right)^{2/5}. \tag{5.20}$$

A conjugate intensive mechanical variable denoted $\mathcal{P}$ and referred to as "harmonic pressure" can also be derived [105–107]. This "harmonic pressure" governs mechanical equilibrium of the gas, much like hydrostatic pressure governs mechanical equilibrium of a fluid in a container with rigid walls:

$$\mathcal{P} = -\left.\frac{\partial E}{\partial \mathcal{V}}\right|_N = \frac{15^{2/5}}{7} m^{1/5} N \left(\frac{N a_s}{\hbar}\right)^{2/5} \mathcal{V}^{-7/5}, \tag{5.21}$$

This expression may be equivalently derived by substituting the Thomas-Fermi density into the integral of the harmonic pressure given in [105]. The total energy can then be rewritten as

$$E = \frac{5}{2}\frac{15^{2/5}}{7} m^{1/5} N \left(\frac{N a_s}{\hbar \mathcal{V}}\right)^{2/5} = \frac{5}{2}\mathcal{P}\mathcal{V}, \tag{5.22}$$

and by using the definition of the Thomas-Fermi energy, we can recover an analogy to the ideal gas law:

$$\mathcal{P}\mathcal{V} = \frac{2}{7} N \mu. \tag{5.23}$$

It is important to note that while μ plays the role of an "effective temperature" it is unrelated to a thermal equilibrium. In our cycle, strokes of constant μ are analogous to isothermal strokes in the classical cycle.

We now have all of the pieces to establish a connection with the Otto cycle. The first stage is an adiabatic compression $\bar{\omega}_A \to \bar{\omega}_B = \nu \bar{\omega}_A$ with compression ratio ν. This traces

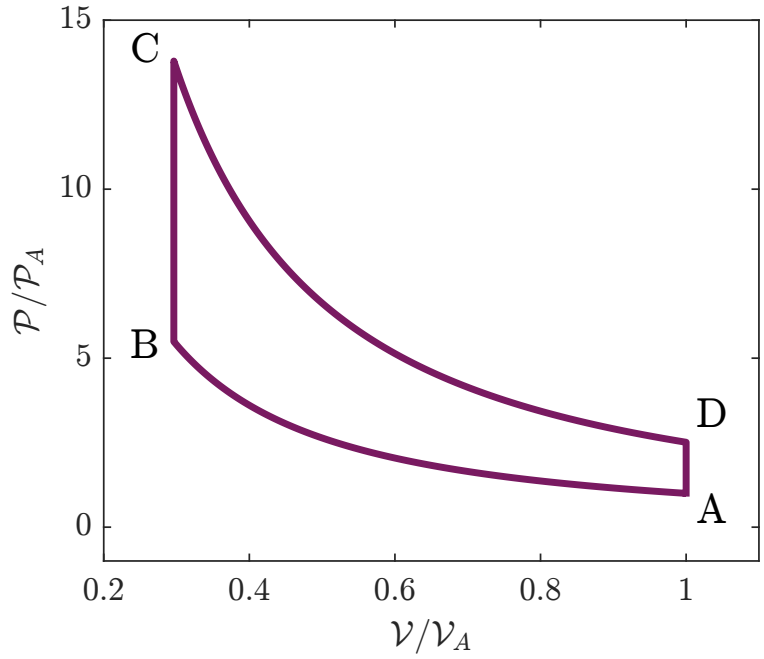

Fig. 5.9: $\mathcal{PV}$ diagram for the thermodynamic engine. $\mathcal{V}_A$ and $\mathcal{P}_A$ are the harmonic volume and pressure evaluated at step A of the engine cycle. Here $\kappa = 10$ and $\nu = 1.5$.

an adiabat in the $\mathcal{PV}$-space.Using Eq. 5.23, the adiabat is defined by

$$\mathcal{V}\mu^{5/2} = \text{constant}, \quad \text{or} \quad \mathcal{V}^{7/5}\mathcal{P} = \text{constant}. \tag{5.24}$$

The heating stroke in the classical Otto cycle is replaced by an interaction strength stroke, which keeps the harmonic volume unchanged but changes the chemical potential and the harmonic pressure, thus mimicking an "isochoric" process. We note that this is not an actual transfer of heat, as the thermodynamic entropy is constant. The final two strokes follow the same arguments presented above. A quantitative $\mathcal{PV}$ diagram of this thermodynamic cycle is shown in Fig. 5.9.

This mathematical analogy enables an alternative derivation of the efficiency of the thermodynamic engine, allowing us to use the Otto cycle efficiency directly with the

adiabatic exponent $\gamma = 7/5$:

$$\eta = 1 - \left(\frac{\mathcal{V}_B}{\mathcal{V}_A}\right)^{\gamma-1} = 1 - \left(\frac{\mathcal{V}_B}{\mathcal{V}_A}\right)^{2/5} = 1 - \left(\frac{\bar{\omega}_A}{\bar{\omega}_B}\right)^{6/5} = 1 - \nu^{-6/5} \tag{5.25}$$

This is the same expression as Eq. 5.19.

5.4 Conclusions

In conclusion, we have realized an isentropic thermodynamic engine with a quantum degenerate working fluid and demonstrated that it outperforms a classical counterpart. Bose-Einstein statistics enable a high ground state occupation throughout the cycle, making manipulation of internal energy straightforward via manipulation of the ground state energy. The quantum-enhanced density of the BEC is essential; interaction-tuning strokes had no observable effect on the dilute thermal gas at the same confinement ratio. It is interesting to note that quantum statistics drive work output in a very different way in the recently-reported Pauli engine [91]: while work done in the Pauli engine is a consequence of excited-state occupation forced by a change to Fermi statistics, the work output in our engine arises chiefly from changes in the ground state energy. Experimental measurements of engine performance for various values of control parameters and degrees of adiabaticity are in good agreement with both low-temperature analytics and approximation-free numerical simulations.

This work opens up a variety of interesting directions for future exploration. These include optimizing performance with shortcuts to adiabaticity [67, 68, 73, 108], realizing a quantum Otto refrigerator [109–113], applying similar techniques to quantum heat engines involving trapped reservoirs of hot and cold atoms, investigating the role of

criticality [69], and experimentally exploring the effects of entanglement on quantum thermodynamic engines [114–116].

5.5 Future work

The prior experiment represents an initial step in realizing macroscopic quantum thermodynamic engines. In this section, I'll discuss two ideas that can extend the work we have done so far. The first will explore how to increase the power output of these engines by speeding up the ramps without sacrificing effective adiabaticity, while the second will explore how to create a true Otto cycle with the BEC system.

5.5.1 Shortcuts to adiabaticity for quantum thermodynamic engines

Optimizing a quantum thermodynamic engine requires increasing speed without sacrificing coherence. Faster strokes lead to larger power outputs, as well as increased repetition before loss from heating. However, when Hamiltonian parameters are varied too quickly, diabatic heating results due to unwanted transitions. To combat this, an extensive body of theoretical and experimental work has focused on creating *shortcuts to adiabaticity* (STAs) [67, 68, 103]. Conceptually, these are protocols that quickly evolve an initial state into a target state, typically on time scales much faster than an equivalent adiabatic process would. These schemes work by optimizing time variation of Hamiltonian control parameters while minimizing unwanted excitations, but they do not guarantee adiabaticity during the process itself. More generally, these protocols are also an active area of research for gate-based quantum computing as well as quantum annealing, where faster speeds allows for increased computation and simulation [117].

Generally, the steps to create an STA are outlined below:

1. Pick the control parameter that must be varied to get from the initial state to the target state.

2. Find a *dynamical* invariant of motion, which is a relation that holds true during the entire protocol.

3. From the invariant, find all boundary conditions for the system. These do not necessarily prevent excitations during the ramp, but rather are relations that must hold for the initial and final states.

4. To satisfy all boundary conditions, a polynomial ansatz of arbitrarily high order can be used. Use this to solve for the dynamical quantity as a function of control parameter

5. That equation can be inverted to obtain the proper protocol for the desired control parameter

For quantum thermodynamic engines, theoretical work has been completed to create STAs for both interaction and dipole trap ramps following procedures similar to the one described above. In [95], a protocol is specifically solved for an interacting BEC in a harmonic trap. Starting with the Gross-Pitaevskii equation 1.10, the interaction strength g is chosen as the control parameter. Going into the Thomas-Fermi regime, an appropriate scaling ansatz can be chosen such that the interaction strength takes the following form:

$$g(t) = g_i \frac{a^2(t)}{\omega^2}[\ddot{a}(t) + \omega^2 a(t)], \tag{5.26}$$

where a is the s-wave scattering length and ω is the harmonic trap frequency for the potential $V(x) = \frac{1}{2}m\omega^2 x^2$. Eq. 5.26 is the dynamical invariant of motion, always holding true during the STA protocol. Now appropriate boundary conditions for $a(t)$ can be chosen:

$$\begin{aligned} a(0) = a_i = 1, \\ a(T_f) = a_f = (g_f/g_i)^{1/3}, \\ \dot{a}(0) = \dot{a}(T_f) = \ddot{a}(0) = \ddot{a}(T_f) = 0. \end{aligned} \tag{5.27}$$

Fulfilling the above equations, we can engineer a ramp from interaction strength g_i to g_f in an arbitarily small time T_f. The boundary conditions can be satisfied by choosing a fifth order polynomial for $a(t)$:

$$a(t) = a_i + (a_f - a_i)(10s^3 - 15s^4 + 6s^5) \tag{5.28}$$

where $s = t/T_f$. Here lies the power of STAs: regardless of the number of boundary conditions, the polynomial dictatiing the parameter evolution can be of arbitrary order, meaning that as long as satisfactory boundary conditions can be found for the evolution, an STA should be achievable. It's worth noting that 5.26 is only true for one dimension, but can be generalized to arbitrary dimension according to the following:

$$g(t) = g_i \frac{a^{d+1}(t)}{\omega^2}[\ddot{a}(t) + \omega^2 a(t)]. \tag{5.29}$$

An example protocol using the form of 5.29 is shown in Fig. 5.10 for multiple time values, taken from [95]. I created an equivalent STA for the second stroke of the quantum thermodynamic engine described in the main results 5.3 using the same method, shown

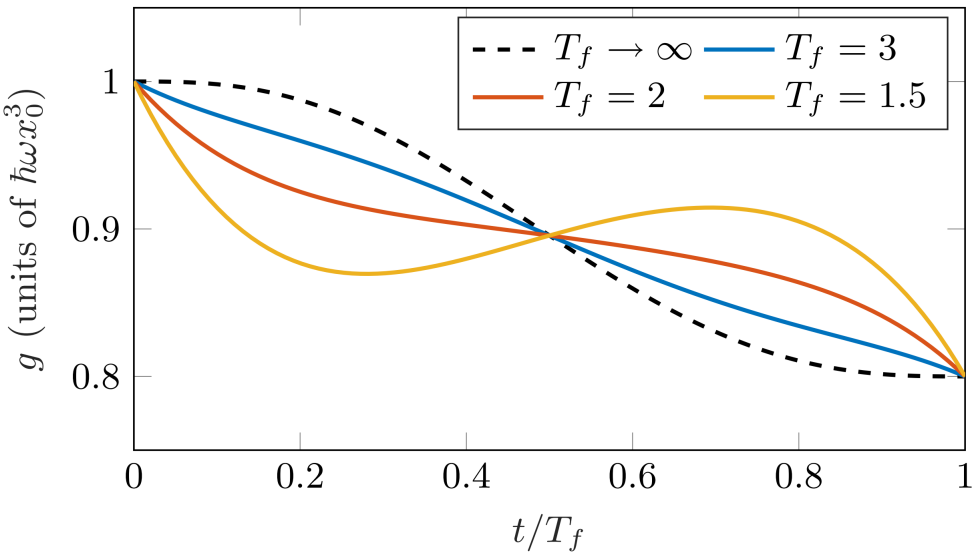

Fig. 5.10: STA for interaction ramp on a BEC in 3D. T_f is in units of $1/\omega$. Taken from [95].

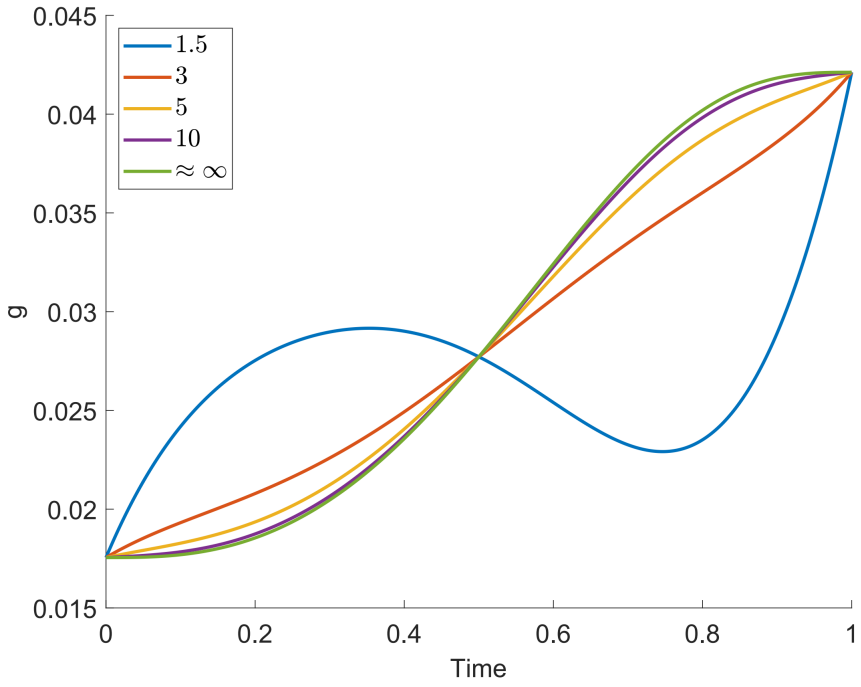

Fig. 5.11: STA for interaction ramp on a BEC in 3D. T_f is in units of $1/\omega$ with $\omega = 2\pi * 100$Hz. Here $a_i = 100a_0$ and $a_f = 240a_0$.

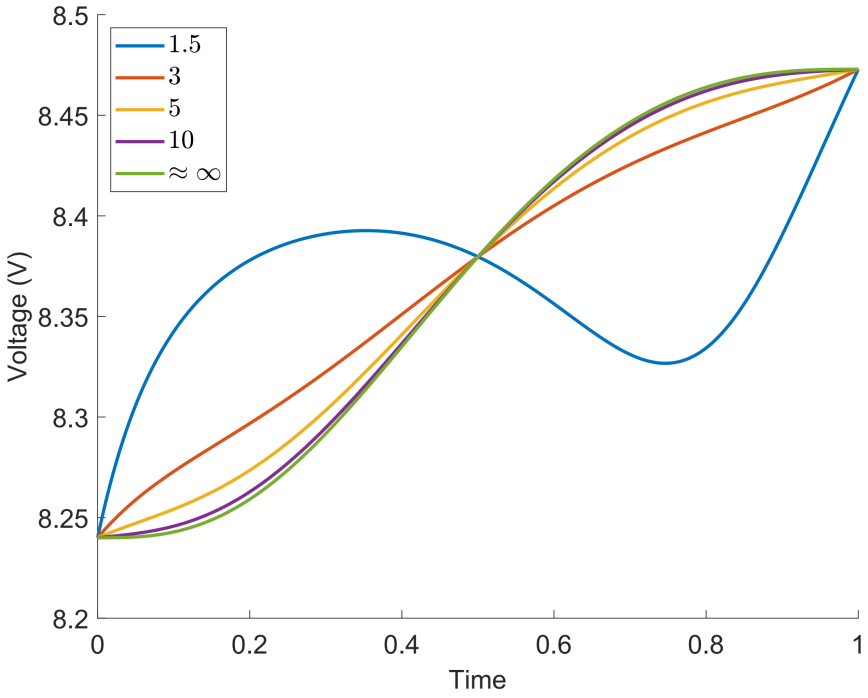

Fig. 5.12: Voltage waveforms for the STA protocol shown in Fig. 5.11.

in Fig 5.11. The interaction strength can be converted into a control voltage signal, which can be directly fed into the Cicero GUI to realize this protocol. Example voltage signals are shown in Fig. 5.12.

The above STA can be used to engineer ramps for strokes 2 and 4 of the quantum thermodynamic engine discussed in this chapter. Similar STAs have been created for ramping harmonic potentials, which can be used for strokes 1 and 3. Extensive analyses of these schemes are shown in [104, 108]. Unfortunately I will be graduating before attempting this experiment, but future students are welcome to engineer these shortcuts in order to realize a higher power quantum engine.

5.5.2 Quantum Otto Cycle

A relevant extension of this quantum thermodynamic engine would be to create a quantum Otto cycle, with a mechanism for adding and removing heat to the working

fluid to perfectly reflect engines used in modern vehicles. While a plethora of theory work has been performed in this realm [109–113], no experiments have achieved this cycle. While heat can be easily applied to the BEC by means of shaking or shining specific frequencies of light, cooling remains an open challenge for this setup. Currently, there are ideas of cooling via partial evaporation within the engine cycle, but this loses efficacy as the density of atoms is reduced, and is unrepeatable after a few cycles.

Another approach would be to create two extra atomic clouds to act as reservoirs. Our group is actively building a new apparatus with the goal of trapping BECs of potassium in optical tweezers. In such an apparatus, three atomic clouds could be created in adjacent sites, with the central cloud acting as a working fluid and the other two acting as hot and cold reservoirs, with the temperature differences achieved by varying the evaporative cooling performed on each cloud.

Appendix A

Code Primer

This appendix provides code for calculating the static band structure of atoms in an optical lattice, following the plane-wave basis treatment outlined in Sec. 1.6.

```
%% Set up band parameters
Nbands = 101;    % Number of bands considered
Nq = 250;        % Number of quasimomentum points
V0 = 3;          % Lattice depth (in Er)

%% Initialize matricies for energy and momentum
q = linspace(-1,1,Nq); % Quasimomentum array, in units of hk
E = zeros(length(q),Nbands); % Matrix to store energy bands
k = -Nbands+1:2:Nbands-1;  % Array of sequential plane wave
   states
Vmat = (V0/4)*gallery('tridiag',Nbands,1,0,1);  %Potential
   matrix for the lattice

% Compute energy band values for every quasimomenta
```

```
for jj = 1:length(q)
    % Kinetic energy Hamiltonian term for this q
    Tmat = sparse(1:Nbands,1:Nbands,(q(jj)+k).^2,Nbands,
       Nbands);

    % Band energies computed by diagonalizing the full
       Hamiltonian
    E(jj,:) = eig(full(Tmat+Vmat));
end

%% Plot band structure
figure(1); clf;
plot(q, E(:,1:4))
```

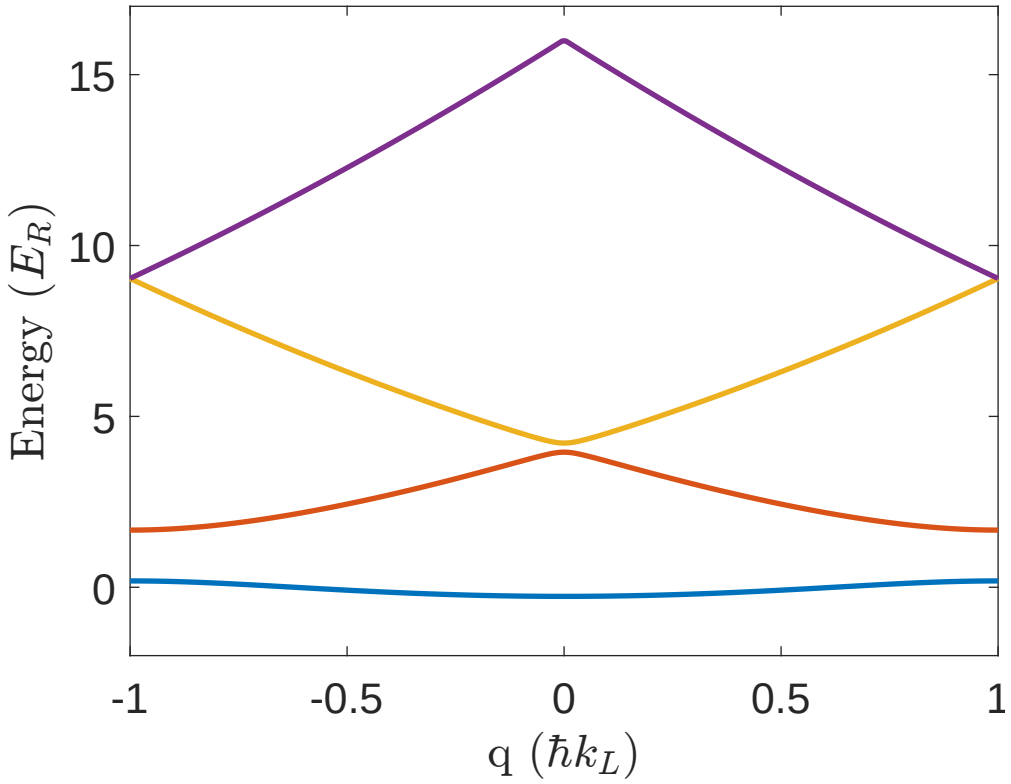

Fig. A.1: First four static bands for $V_0 = 3E_{\mathrm{R}}$

Appendix B

Calculating Atom Interferometer Phase

One active project on the lithium machine is the continuously trapped atom interferometer, created by periodically modulating the optical lattice to induce band transitions on the atoms. This *Floquet engineering* allows for the creation of atomic beamsplitters and mirrors while the BEC is Bloch oscillating in the bands. A simple interferometric loop is couple the bands at a quasimomentum k_1 to induce a 50/50 split of the atoms, and then couple the bands again at quasimomentum k_2 to close the loop. The atoms in the excited trajectory will follow $E_2(t)$ while the atoms still in the ground band will follow $E_1(t)$. The following calculation is to determine the relevant factors in the accumulated phase between the atoms as they go through this interferometric loop.

The phase accumulated in our atom interferometer is defined as:

$$\phi = \frac{1}{\hbar}\int_{t_1}^{t_2}(E_2(t) - E_1(t))dt. \tag{B.1}$$

Since our current code gives us the energy as a function of k, we'd like our integration variable to be k. Doing a simple change of variables:

$$\phi = \frac{1}{\hbar}\int_{k_1*}^{k_2*}(E_2(k) - E_1(k))dk\frac{dt}{dk}. \tag{B.2}$$

We can approximate $\frac{dt}{dk}$ using the following:

$$\frac{dt}{dk} = \frac{T_B}{2\hbar k} = \frac{T_B}{2}. \tag{B.3}$$

The intuition here is that while the atoms travel over one Brillouin zone, one Bloch period (T_B) of time passes and their momenta change by $2\hbar k$. This should be constant over the zone, since the force the atoms experience during one Bloch oscillation is roughly constant. We then factor out E_R for code consistency since our energies are normalized by the recoil energy:

$$\phi = \frac{T_B}{2\hbar}\int_{k_1*}^{k_2*}(\frac{E_2(k)}{E_R} - \frac{E_1(k)}{E_R})E_R dk. \tag{B.4}$$

We then rearrange some terms:

$$\phi = \frac{T_B}{2} * 2\pi * \frac{E_r}{h}\int_{k_1*}^{k_2*}(\frac{E_2(k)}{E_R} - \frac{E_1(k)}{E_R})dk. \tag{B.5}$$

Here, the recoil energy divided by Planck's constant is the recoil frequency:

$$\frac{E_r}{h} = f_{Rec} = 25.2\text{kHz}, T_B = 20\text{ms}, \tag{B.6}$$

where 20 ms is a typical Bloch period we use for our system. We'll define the integral as its own variable. Notice that it is now dimensionless.

$$S = \int_{k_1*}^{k_2*} (\frac{E_2(k)}{E_R} - \frac{E_1(k)}{E_R}) dk \tag{B.7}$$

The final expression for the phase (in full periods) is:

$$\frac{\phi}{2\pi} = \frac{T_B f_{Rec} S}{2} \tag{B.8}$$

The important thing to notice is that $\frac{T_B f_{Rec}}{2} = 252$, meaning that any variation in S will be multiplied by 252 for $T_B = 20$ ms. To reduce this variation, it is crucial to create loops with smaller Bloch periods, ideally ≈ 1 ms. In order to accurately evaluate the interferometer, it is necessary to sample at least 5-10 points per oscillation, which is easier to do the smaller the accumulated phase is. $S \approx 1$ in loops that span non-negligible fractions of the Brillouin zone ($\approx .5$) for relatively small lattice depths ($\approx 5E_R$), meaning that in a typical loop the atoms will accumulate 2π phase hundreds of times. Hence, a drastic reduction in Brillouin zone span in addition to the reduction in Bloch period will most likely be necessary in order to probe the phase accumulation in this type of interferometer.

Bibliography

[1] Z. Geiger, *An Apparatus for Dynamical Quantum Emulation Using Ultracold Lithium*. PhD thesis, UC Santa Barbara, 2018.

[2] K. Singh, *Floquet Engineering with Ultracold Lithium in Optical Lattices*. PhD thesis, UC Santa Barbara, 2019.

[3] C. J. Fujiwara, *Dynamics of Ultracold Lithium in Modulated Optical Lattices*. PhD thesis, UC Santa Barbara, 2019.

[4] C. Foot, *Atomic Physics*. Oxford University Press, 2005.

[5] NobelPrize.org, "The Nobel Prize in Physics 1997." `https://www.nobelprize.org/prizes/physics/1997/summary/`. Accessed: 1/5/2024.

[6] W. Ketterle, D. S. Durfee, and D. M. Stamper-Kurn, *Making, probing and understanding Bose-Einstein condensates*, Apr., 1999. arXiv:cond-mat/9904034.

[7] L. Pitaevskii and S. Stringari, *Bose-Einstein Condensation and Superfluidity*. Oxford University Press, 2016.

[8] C. Chin, R. Grimm, P. Julienne, and E. Tiesinga, *Feshbach resonances in ultracold gases*, *Reviews of Modern Physics* **82** (Apr., 2010) 1225–1286.

[9] S. E. Pollack, D. Dries, M. Junker, Y. P. Chen, T. A. Corcovilos, and R. G. Hulet, *Extreme Tunability of Interactions in a Li 7 Bose-Einstein Condensate*, *Physical Review Letters* **102** (Mar., 2009) 090402.

[10] C. Chin, V. Vuletić, A. J. Kerman, S. Chu, E. Tiesinga, P. J. Leo, and C. J. Williams, *Precision Feshbach spectroscopy of ultracold Cs 2*, *Physical Review A* **70** (Sept., 2004) 032701.

[11] Z. A. Geiger, K. M. Fujiwara, K. Singh, R. Senaratne, S. V. Rajagopal, M. Lipatov, T. Shimasaki, R. Driben, V. V. Konotop, T. Meier, and D. M. Weld, *Observation and Uses of Position-Space Bloch Oscillations in an Ultracold Gas*, *Physical Review Letters* **120** (May, 2018) 213201.

[12] S. Gupta, A. E. Leanhardt, A. D. Cronin, and D. E. Pritchard, *Coherent manipulation of atoms with standing light waves*, *Comptes Rendus de l'Académie des Sciences - Series IV - Physics* **2** (Apr., 2001) 479–495.

[13] P. W. Anderson, *Absence of Diffusion in Certain Random Lattices*, *Phys. Rev.* **109** (Mar, 1958) 1492–1505.

[14] Y. Lahini, A. Avidan, F. Pozzi, M. Sorel, R. Morandotti, D. N. Christodoulides, and Y. Silberberg, *Anderson Localization and Nonlinearity in One-Dimensional Disordered Photonic Lattices*, *Physical Review Letters* **100** (Jan., 2008) 013906.

[15] G. Roati, C. D'Errico, L. Fallani, M. Fattori, C. Fort, M. Zaccanti, G. Modugno, M. Modugno, and M. Inguscio, *Anderson localization of a non-interacting Bose–Einstein condensate*, *Nature* **453** (June, 2008) 895–898.

[16] M. Weidemüller, T. Esslinger, M. A. Ol'shanii, A. Hemmerich, and T. W. Hänsch, *A Novel Scheme for Efficient Cooling below the Photon Recoil Limit*, *Europhysics Letters* **27** (July, 1994) 109.

[17] A. T. Grier, I. Ferrier-Barbut, B. S. Rem, M. Delehaye, L. Khaykovich, F. Chevy, and C. Salomon, *$\ensuremath{\Lambda}$-enhanced sub-Doppler cooling of lithium atoms in ${D}_{1}$ gray molasses*, *Physical Review A* **87** (June, 2013) 063411.

[18] Wikipedia, "Gray molasses." `https://en.wikipedia.org/wiki/Gray_molasses`. Accessed: 1/5/2024.

[19] D. M. Brink and C. V. Sukumar, *Majorana spin-flip transitions in a magnetic trap*, *Physical Review A* **74** (Sept., 2006) 035401.

[20] K. E. Strecker, G. B. Partridge, A. G. Truscott, and R. G. Hulet, *Bright matter wave solitons in Bose–Einstein condensates*, *New Journal of Physics* **5** (June, 2003) 73.

[21] E. Technologies, "pco.edge 5.5 usb scmos camera." `https://www.excelitas.com/product/pcoedge-55-usb-scmos-camera`. Accessed: 1/5/2024.

[22] A. Cao, *Studying Quantum Dynamics in Driven Degenerate Gases*. PhD thesis, UC Santa Barbara, 2021.

[23] A. Keshet and W. Ketterle, *A distributed, graphical user interface based, computer control system for atomic physics experiments*, *Review of Scientific Instruments* **84** (01, 2013) 015105, [https://pubs.aip.org/aip/rsi/article-pdf/doi/10.1063/1.4773536/14701602/015105_1_online.pdf].

[24] B. V. Chirikov, *Research concerning the theory of non-linear resonance and stochasticity*. CERN, Geneva, 1971. Translated at CERN from the Russian (IYAF-267-TRANS-E).

[25] B. V. Chirikov, *A universal instability of many-dimensional oscillator systems*, *Phys. Rep.* **52** (1979), no. 5 263 – 379.

[26] V. I. Arnol'd, *PROOF OF A THEOREM OF A. N. KOLMOGOROV ON THE INVARIANCE OF QUASI-PERIODIC MOTIONS UNDER SMALL PERTURBATIONS OF THE HAMILTONIAN*, *Russian Mathematical Surveys* **18** (Oct., 1963) 9.

[27] S. Fishman, D. R. Grempel, and R. E. Prange, *Chaos, quantum recurrences, and anderson localization*, *Phys. Rev. Lett.* **49** (Aug, 1982) 509–512.

[28] D. R. Grempel, R. E. Prange, and S. Fishman, *Quantum dynamics of a nonintegrable system*, *Phys. Rev. A* **29** (Apr, 1984) 1639–1647.

[29] L. Tessieri, Z. Akdeniz, N. Cherroret, D. Delande, and P. Vignolo, *Quantum boomerang effect: Beyond the standard Anderson model*, *Physical Review A* **103** (June, 2021) 063316.

[30] F. L. Moore, J. C. Robinson, C. F. Bharucha, B. Sundaram, and M. G. Raizen, *Atom optics realization of the quantum δ-kicked rotor*, *Phys. Rev. Lett.* **75** (Dec, 1995) 4598–4601.

[31] I. Manai, J.-F. m. c. Clément, R. Chicireanu, C. Hainaut, J. C. Garreau, P. Szriftgiser, and D. Delande, *Experimental observation of two-dimensional anderson localization with the atomic kicked rotor*, *Phys. Rev. Lett.* **115** (Dec, 2015) 240603.

[32] J. Chabé, G. Lemarié, B. Grémaud, D. Delande, P. Szriftgiser, and J. C. Garreau, *Experimental observation of the anderson metal-insulator transition with atomic matter waves*, *Phys. Rev. Lett.* **101** (Dec, 2008) 255702.

[33] M. Lopez, J.-F. m. c. Clément, P. Szriftgiser, J. C. Garreau, and D. Delande, *Experimental test of universality of the anderson transition*, *Phys. Rev. Lett.* **108** (Feb, 2012) 095701.

[34] D. A. Abanin, E. Altman, I. Bloch, and M. Serbyn, *Colloquium: Many-body localization, thermalization, and entanglement*, *Rev. Mod. Phys.* **91** (May, 2019) 021001.

[35] R. Nandkishore and D. A. Huse, *Many-body localization and thermalization in quantum statistical mechanics*, *Annu. Rev. Condens. Matter Phys.* **6** (2015), no. 1 15–38.

[36] K. Singh, C. J. Fujiwara, Z. A. Geiger, E. Q. Simmons, M. Lipatov, A. Cao, P. Dotti, S. V. Rajagopal, R. Senaratne, T. Shimasaki, M. Heyl, A. Eckardt, and D. M. Weld, *Quantifying and controlling prethermal nonergodicity in interacting floquet matter*, *Phys. Rev. X* **9** (Oct, 2019) 041021.

[37] A. Rubio-Abadal, M. Ippoliti, S. Hollerith, D. Wei, J. Rui, S. L. Sondhi, V. Khemani, C. Gross, and I. Bloch, *Floquet prethermalization in a bose-hubbard system*, *Phys. Rev. X* **10** (May, 2020) 021044.

[38] R. Bouganne, M. B. Aguilera, A. Ghermaoui, J. Beugnon, and F. Gerbier, *Anomalous decay of coherence in a dissipative many-body system*, *Nat. Phys.* **16** (2020), no. 1 21–25.

[39] S. Lellouch, A. Rançon, S. De Bièvre, D. Delande, and J. C. Garreau, *Dynamics of the mean-field-interacting quantum kicked rotor*, *Phys. Rev. A* **101** (Apr, 2020) 043624.

[40] J. Martin, B. Georgeot, and D. L. Shepelyansky, *Cooling by time reversal of atomic matter waves*, *Phys. Rev. Lett.* **100** (Feb, 2008) 044106.

[41] A. Ullah and M. D. Hoogerland, *Experimental observation of loschmidt time reversal of a quantum chaotic system*, *Phys. Rev. E* **83** (Apr, 2011) 046218.

[42] A. Cao, R. Sajjad, H. Mas, E. Q. Simmons, J. L. Tanlimco, E. Nolasco-Martinez, T. Shimasaki, H. E. Kondakci, V. Galitski, and D. M. Weld, *Interaction-driven breakdown of dynamical localization in a kicked quantum gas*, *Nature Physics* **18** (Nov., 2022) 1302–1306.

[43] A. Tenart, C. Carcy, H. Cayla, T. Bourdel, M. Mancini, and D. Clément, *Two-body collisions in the time-of-flight dynamics of lattice Bose superfluids*, *Physical Review Research* **2** (Jan., 2020) 013017.

[44] J. Hecker Denschlag, J. E. Simsarian, H. Haffner, C. McKenzie, A. Browaeys, D. Cho, H. K, S. L. Rolston, and W. D. Phillips, *A bose-einstein condensate in an optical lattice*, *Journal of Physics B: Atomic, Molecular, and Optical Physics* (2002).

[45] A. Ullah, S. Ruddell, J. Currivan, and M. Hoogerland, *Quantum resonant effects in the delta-kicked rotor revisited*, *Eur. Phys. Jour. D.* **66** (2012) 315.

[46] M. Lepers, V. Zehnlé, and J. C. Garreau, *Kicked-rotor quantum resonances in position space*, *Phys. Rev. A* **77** (Apr, 2008) 043628.

[47] R. Sajjad, "Interaction-driven breakdown of dynamical localization in a kicked quantum gas." `https://communities.springernature.com/posts/interaction-driven-breakdown-of-dynamical-localization-in-a-kicked-quantum-gas`. Published: 2022-09-26.

[48] R. Sajjad, J. L. Tanlimco, H. Mas, A. Cao, E. Nolasco-Martinez, E. Q. Simmons, F. L. Santos, P. Vignolo, T. Macrì, and D. M. Weld, *Observation of the Quantum Boomerang Effect*, *Physical Review X* **12** (Feb., 2022) 011035.

[49] T. Prat, D. Delande, and N. Cherroret, *Quantum boomeranglike effect of wave packets in random media*, *Physical Review A* **99** (Feb., 2019) 023629.

[50] C. Ryu, M. F. Andersen, A. Vaziri, M. B. d'Arcy, J. M. Grossman, K. Helmerson, and W. D. Phillips, *High-order quantum resonances observed in a periodically kicked bose-einstein condensate*, *Phys. Rev. Lett.* **96** (Apr, 2006) 160403.

[51] W. H. Oskay, D. A. Steck, and M. G. Raizen, *Timing noise effects on dynamical localization*, *Chaos, Solitons & Fractals* **16** (2003), no. 3 409–416.

[52] A. Cao, R. Sajjad, H. Mas, E. Q. Simmons, J. L. Tanlimco, E. Nolasco-Martinez, T. Shimasaki, H. E. Kondakci, V. Galitski, and D. M. Weld, *Interaction-driven breakdown of dynamical localization in a kicked quantum gas*, 2021.

[53] J. Ringot, P. Szriftgiser, J. C. Garreau, and D. Delande, *Experimental evidence of dynamical localization and delocalization in a quasiperiodic driven system*, *Phys. Rev. Lett.* **85** (Sep, 2000) 2741–2744.

[54] D. H. White, S. K. Ruddell, and M. D. Hoogerland, *Phase noise in the delta kicked rotor: from quantum to classical*, *New Journal of Physics* **16** (nov, 2014) 113039.

[55] B. G. Klappauf, W. H. Oskay, D. A. Steck, and M. G. Raizen, *Observation of Noise and Dissipation Effects on Dynamical Localization*, *Phys. Rev. Lett.* **81** (Aug, 1998) 1203–1206.

[56] R. Blümel and U. Smilansky, *Symmetry breaking and localization in quantum chaotic systems*, *Phys. Rev. Lett.* **69** (Jul, 1992) 217–220.

[57] J. Janarek, D. Delande, N. Cherroret, and J. Zakrzewski, *Quantum boomerang effect for interacting particles*, *Physical Review A* **102** (July, 2020) 013303.

[58] J. Janarek, B. Grémaud, J. Zakrzewski, and D. Delande, *Quantum boomerang effect in systems without time-reversal symmetry*, *Physical Review B* **105** (May, 2022) L180202.

[59] J. Janarek, J. Zakrzewski, and D. Delande, *Many-body quantum boomerang effect*, *Physical Review B* **107** (Mar., 2023) 094204.

[60] F. Noronha and T. Macrì, *Ubiquity of the quantum boomerang effect in Hermitian Anderson-localized systems*, *Physical Review B* **106** (Aug., 2022) L060301.

[61] F. Noronha, J. A. S. Lourenço, and T. Macrì, *Robust quantum boomerang effect in non-Hermitian systems*, *Physical Review B* **106** (Sept., 2022) 104310.

[62] H. T. Quan, Y.-x. Liu, C. P. Sun, and F. Nori, *Quantum thermodynamic cycles and quantum heat engines*, *Phys. Rev. E* **76** (sep, 2007) 031105.

[63] Y. Zheng and D. Poletti, *Work and efficiency of quantum otto cycles in power-law trapping potentials*, *Phys. Rev. E* **90** (July, 2014) 012145.

[64] Y. Zheng and D. Poletti, *Quantum statistics and the performance of engine cycles*, *Phys. Rev. E* **92** (July, 2015) 012110.

[65] R. Kosloff and Y. Rezek, *The quantum harmonic otto cycle*, *Entropy* **19** (2017), no. 4 136.

[66] S. Hamedani Raja, S. Maniscalco, G. S. Paraoanu, J. P. Pekola, and N. Lo Gullo, *Finite-time quantum Stirling heat engine*, *New J. Phys.* **23** (Mar., 2021) 033034.

[67] M. Beau, J. Jaramillo, and A. Del Campo, *Scaling-up quantum heat engines efficiently via shortcuts to adiabaticity*, *Entropy* **18** (2016), no. 5 168.

[68] J. Li, T. Fogarty, S. Campbell, X. Chen, and T. Busch, *An efficient nonlinear Feshbach engine*, *New J. of Phys.* **20** (Jan., 2018) 015005.

[69] Y.-Y. Chen, G. Watanabe, Y.-C. Yu, X.-W. Guan, and A. del Campo, *An interaction-driven many-particle quantum heat engine and its universal behavior*, *npj Quantum Inf.* **5** (oct, 2019) 1–6.

[70] N. Yunger Halpern, C. D. White, S. Gopalakrishnan, and G. Refael, *Quantum engine based on many-body localization*, *Phys. Rev. B* **99** (2019), no. 2 024203.

[71] G. Barontini and M. Paternostro, *Ultra-cold single-atom quantum heat engines*, *New J. Phys.* **21** (2019), no. 6 063019.

[72] F. Carollo, K. Brandner, and I. Lesanovsky, *Nonequilibrium Many-Body Quantum Engine Driven by Time-Translation Symmetry Breaking*, *Phys. Rev. Lett.* **125** (Dec., 2020) 240602.

[73] T. Keller, T. Fogarty, J. Li, and T. Busch, *Feshbach engine in the Thomas-Fermi regime*, *Phys. Rev. Research* **2** (Aug., 2020) 033335.

[74] M. Gluza, J. a. Sabino, N. H. Ng, G. Vitagliano, M. Pezzutto, Y. Omar, I. Mazets, M. Huber, J. Schmiedmayer, and J. Eisert, *Quantum field thermal machines*, *PRX Quantum* **2** (Jul, 2021) 030310.

[75] M. Boubakour, T. Fogarty, and T. Busch, *Interaction-enhanced quantum heat engine*, *Phys. Rev. Research* **5** (2023), no. 1 013088.

[76] J. Eglinton, T. Pyharanta, K. Saito, and K. Brandner, *Thermodynamic geometry of ideal quantum gases: A general framework and a geometric picture of BEC-enhanced heat engines*, *arXiv.2212.12076* (Dec., 2022).

[77] N. M. Myers, F. J. Peña, O. Negrete, P. Vargas, G. De Chiara, and S. Deffner, *Boosting engine performance with Bose-Einstein condensation*, *New J. Phys.* **24** (Feb., 2022) 025001.

[78] J. Roßnagel, O. Abah, F. Schmidt-Kaler, K. Singer, and E. Lutz, *Nanoscale Heat Engine Beyond the Carnot Limit*, *Phys. Rev. Lett.* **112** (Jan., 2014) 030602.

[79] K. Zhang, F. Bariani, and P. Meystre, *Quantum Optomechanical Heat Engine*, *Phys. Rev. Lett.* **112** (Apr., 2014) 150602.

[80] J.-M. Park, S. Lee, H.-M. Chun, and J. D. Noh, *Quantum mechanical bound for efficiency of quantum Otto heat engine*, *Phys. Rev. E* **100** (July, 2019) 012148.

[81] F. Wu, L. Chen, F. Sun, C. Wu, F. Guo, and Q. Li, *Quantum degeneracy effect on performance of irreversible Otto cycle with ideal Bose gas*, *Energy Convers. and Manag.* **47** (Nov., 2006) 3008–3018.

[82] J. Roßnagel, S. T. Dawkins, K. N. Tolazzi, O. Abah, E. Lutz, F. Schmidt-Kaler, and Kilian Singer, *A single-atom heat engine*, *Science* **352** (2016), no. 6283 325–329.

[83] J. Bu, J. Zhang, G. Ding, J. Li, J. Zhang, B. Wang, W. Ding, W. Yuan, L. Chen, S. Özdemir, F. Zhou, H. Jing, and M. Feng, *Enhancement of quantum heat engine by encircling a Liouvillian exceptional point*, *Phys. Rev. Lett.* **130** (Mar, 2023) 110402.

[84] J. P. S. Peterson, T. B. Batalhão, M. Herrera, A. M. Souza, R. S. Sarthour, I. S. Oliveira, and R. M. Serra, *Experimental characterization of a spin quantum heat engine*, *Phys. Rev. Lett.* **123** (Dec, 2019) 240601.

[85] J.-P. Brantut, C. Grenier, J. Meineke, D. Stadler, S. Krinner, C. Kollath, T. Esslinger, and A. Georges, *A thermoelectric heat engine with ultracold atoms*, *Science* **342** (2013), no. 6159 713–715.

[86] Y. Zou, Y. Jiang, Y. Mei, X. Guo, and S. Du, *Quantum heat engine using electromagnetically induced transparency*, *Phys. Rev. Lett.* **119** (2017), no. 5 050602.

[87] J. Nettersheim, S. Burgardt, Q. Bouton, D. Adam, E. Lutz, and A. Widera, *Power of a quasispin quantum otto engine at negative effective spin temperature*, *PRX Quantum* **3** (Dec., 2022) 040334.

[88] I. Reyes-Ayala, M. Miotti, M. Hemmerling, R. Dubessy, H. Perrin, V. Romero-Rochin, and V. S. Bagnato, *Carnot Cycles in a Harmonically Confined Ultracold Gas across Bose–Einstein Condensation*, *Entropy* **25** (Feb., 2023) 311.

[89] J. Klatzow, J. N. Becker, P. M. Ledingham, C. Weinzetl, K. T. Kaczmarek, D. J. Saunders, J. Nunn, I. A. Walmsley, R. Uzdin, and E. Poem, *Experimental demonstration of quantum effects in the operation of microscopic heat engines*, *Phys. Rev. Lett.* **122** (2019), no. 11 110601.

[90] Q. Bouton, J. Nettersheim, S. Burgardt, D. Adam, E. Lutz, and A. Widera, *A quantum heat engine driven by atomic collisions*, *Nat. Commun.* **12** (2021), no. 1 2063.

[91] J. Koch, K. Menon, E. Cuestas, S. Barbosa, E. Lutz, T. Fogarty, T. Busch, and A. Widera, *Making statistics work: A quantum engine in the BEC-BCS crossover*, *arXiv:2209.14202* (Sept., 2022).

[92] J.-M. Park, S. Lee, H.-M. Chun, and J. D. Noh, *Quantum mechanical bound for efficiency of quantum otto heat engine*, *Phys. Rev. E* **100** (2019), no. 1 012148.

[93] G. Watanabe, B. P. Venkatesh, P. Talkner, M.-J. Hwang, and A. del Campo, *Quantum statistical enhancement of the collective performance of multiple bosonic engines*, *Phys. Rev. Lett.* **124** (2020), no. 21 210603.

[94] J. Jaramillo, M. Beau, and A. d. Campo, *Quantum supremacy of many-particle thermal machines*, *New J. Phys.* **18** (2016), no. 7 075019.

[95] T. Keller, T. Fogarty, J. Li, and T. Busch, *Feshbach engine in the Thomas-Fermi regime*, *Phys. Rev. Research* **2** (Aug., 2020) 033335.

[96] A. L. Gaunt, *Degenerate Bose Gases: Tuning Interactions and Geometry*. PhD thesis, University of Cambridge, 2014.

[97] Y. Castin and R. Dum, *Bose-Einstein Condensates in Time Dependent Traps*, *Physical Review Letters* **77** (Dec., 1996) 5315–5319.

[98] D. S. Durfee and W. Ketterle, *Experimental studies of bose-einstein condensation*, *Opt. Express* **2** (Apr, 1998) 299–313.

[99] E. Q. Simmons, R. Sajjad, K. Keithley, H. Mas, J. L. Tanlimco, E. Nolasco-Martinez, Y. Bai, G. H. Fredrickson, and D. M. Weld, *Thermodynamic engine with a quantum degenerate working fluid*, *Physical Review Research* **5** (Oct., 2023) L042009.

[100] P. K. Sorensen, *Three-Body Recombination in Cold Atomic Gases*. PhD thesis, Aarhus University, 2013.

[101] C. Zener, *Non-adiabatic crossing of energy levels*, *Proc. R. Soc. A* **137** (1932), no. 833 696–702.

[102] C. Pethick and H. Smith, *Bose-Einstein Condensation in Dilute Gases*. Cambridge University Press, 2nd ed ed., 2008.

[103] J.-F. Schaff, P. Capuzzi, G. Labeyrie, and P. Vignolo, *Shortcuts to adiabaticity for trapped ultracold gases*, *New Journal of Physics* **13** (Nov., 2011) 113017.

[104] A. Del Campo, *Shortcuts to Adiabaticity by Counterdiabatic Driving*, *Physical Review Letters* **111** (Sept., 2013) 100502.

[105] V. Romero-Rochín, *Equation of state of an interacting bose gas confined by a harmonic trap: The role of the "harmonic" pressure*, *Phys. Rev. Lett.* **94** (2005), no. 13 130601.

[106] V. Romero-Rochín and V. S. Bagnato, *Thermodynamics of an ideal gas of bosons harmonically trapped: equation of state and susceptibilities*, *Brazilian Journal of Physics* **35** (Sept., 2005) 607–613.

[107] N. Sandoval-Figueroa and V. Romero-Rochín, *Thermodynamics of trapped gases: Generalized mechanical variables, equation of state, and heat capacity*, *Physical Review E* **78** (Dec., 2008) 061129.

[108] J.-F. Schaff, X.-L. Song, P. Capuzzi, P. Vignolo, and G. Labeyrie, *Shortcut to adiabaticity for an interacting Bose-Einstein condensate*, *EPL* **93** (2011), no. 2 23001.

[109] A. Hartmann, V. Mukherjee, G. B. Mbeng, W. Niedenzu, and W. Lechner, *Multi-spin counter-diabatic driving in many-body quantum Otto refrigerators*, *Quantum* **4** (Dec., 2020) 377.

[110] W. Niedenzu, I. Mazets, G. Kurizki, and F. Jendrzejewski, *Quantized refrigerator for an atomic cloud*, *Quantum* **3** (June, 2019) 155.

[111] O. Abah, M. Paternostro, and E. Lutz, *Shortcut-to-adiabaticity quantum Otto refrigerator*, *Phys. Rev. Res.* **2** (May, 2020) 023120.

[112] G. Jiao, Y. Xiao, J. He, Y. Ma, and J. Wang, *Quantum otto refrigerators in finite-time cycle period*, *New J. Phys.* **23** (jun, 2021) 063075.

[113] B. Karimi and J. P. Pekola, *Otto refrigerator based on a superconducting qubit: Classical and quantum performance*, *Phys. Rev. B* **94** (Nov, 2016) 184503.

[114] H. Ji-Zhou, H. Xian, and Z. Jie, *Entangled quantum heat engine based on two-qubit Heisenberg XY model*, *Chin. Phys. B* **21** (may, 2012) 050303.

[115] T. Zhang, W.-T. Liu, P.-X. Chen, and C.-Z. Li, *Four-level entangled quantum heat engines*, *Phys. Rev. A* **75** (Jun, 2007) 062102.

[116] L.-M. Zhao and G.-F. Zhang, *Entangled quantum otto heat engines based on two-spin systems with the dzyaloshinski–moriya interaction*, *Quantum Inf. Process.* **16** (Jul, 2017) 216.

[117] D. Guéry-Odelin, A. Ruschhaupt, A. Kiely, E. Torrontegui, S. Martínez-Garaot, and J. Muga, *Shortcuts to adiabaticity: Concepts, methods, and applications*, *Reviews of Modern Physics* **91** (Oct., 2019) 045001.